École polytechnique de Louvain (EPL)

New composites for aeronautical applications

Static and fatigue failure of aerospace grade epoxy resins

Dissertation presented by
Robin DORMAL

for obtaining the Master's degree in
Chemical and Materials Engineering

Supervisor(s)
Thomas PARDOEN

Assistant(s)
Jérémy CHEVALIER

Reader(s)
Issam DOGHRI, Frédéric LANI

Academic year 2016-2017

Abstract

Polymer composites are becoming increasingly prevalent in structural engineering and especially aircrafts manufacture. Highly-crosslinked epoxy resins are used as matrix because of their good properties for reduced weight. However the use of such materials leads to complicated fracture mechanisms which are not fully understood. In this work the fracture behavior of the HexFlow RTM6 epoxy resin is studied. A mechanical testing campaign is performed on dog-bone cylindrical samples and on CT specimens under both static and cycling loadings. This campaign is associated with finite elements analyses to confirm the results and predict the stress state at the crack tip. A fracture toughness of 0.9 MPa $\sqrt{m}$ is found and a stiffness degradation is observed when the material undergoes cycling loading at a sufficient level. An endurance limit of 38 MPa is also found for unnotched specimens and the crack propagation rate curve is obtained. This curve has a threshold of amplitude of stress intensity factor of 0.28 MPa $\sqrt{m}$, where the crack start to slowly propagate and a critical amplitude of stress intensity factor of 0.4MPa $\sqrt{m}$ where final failure occurs. A stable growth is observed between those two behaviors, where a Paris coefficient of 12.3 is found.

Acknowledgements

I would like to thank all the people that helped me writing this thesis. First my promoter, Thomas Pardoen for trusting me to realize this work and for his relevant advices at every meeting. I also want to thank Jérémy Chevalier for his help during the mechanical tests, his numerous advices about the numerical simulations and his regular feedback during the whole year. I also want to thank Alban Maton for the machining of the samples and Marc Sinneave for his help during the mechanical tests, as well as all the people working in IMAP for helping me using the several devices from UCL and particularly Laurence Ryelandt for teaching me the use of the SEM. Finally I want to thank the other students who were working on their own thesis for the mutual help and support.

Computational resources have been provided by the supercomputing facilities of the Université catholique de Louvain (CISM/UCL) and the Consortium des Équipements de Calcul Intensif en Fédération Wallonie Bruxelles (CÉCI) funded by the Fond de la Recherche Scientifique de Belgique (F.R.S.-FNRS) under convention 2.5020.11

Contents

Abbreviations and symbols

RTM	Resin transfer molding
CT	Compact tension
CSR	Constant strain rate
UTS	Ultimate tensile strength.
FF	Fiber fracture
IFF	Inter fiber fracture
SEM	Scanning electron microscope
FCP	Fatigue crack propagation
MPS	Maximum principal stress
LEFM	Linear elastic fracture mechanics
EPFM	Elastic-plastic fracture mechanics
FEA	Finite element analyses

Chapter 1

Introduction

Over the last decades, the search for lighter materials as been a primary concern in the aerospace field, as the main energetic cost of aircrafts is their fuel consumption rather than the materials used for their manufacturing. Reducing the mass of an aircraft would significantly reduce its required energy as well as have a great impact on the environment. Composite materials, with their light weight and good mechanical properties, stand out to be a perfect fit for the structure of aircrafts and their use keeps increasing over the years as figure 1.1 points out. Their use is generally accepted for secondary parts (leading edges, flaps, etc.) but also extends to primary structural parts such as the fuselage. Nowadays manufacturers even use organic matrix composites for motors[1]. Moreover composites have good corrosion resistance and can be made to resist high impact. Their drawback lies is the resistance to crack propagation. They seem to fail in a brittle manner and cracks grow very quickly. A good understanding of the initiations of the cracks and of their propagation is therefore essential. Aircraft are made to last a long time and therefore fatigue properties are very

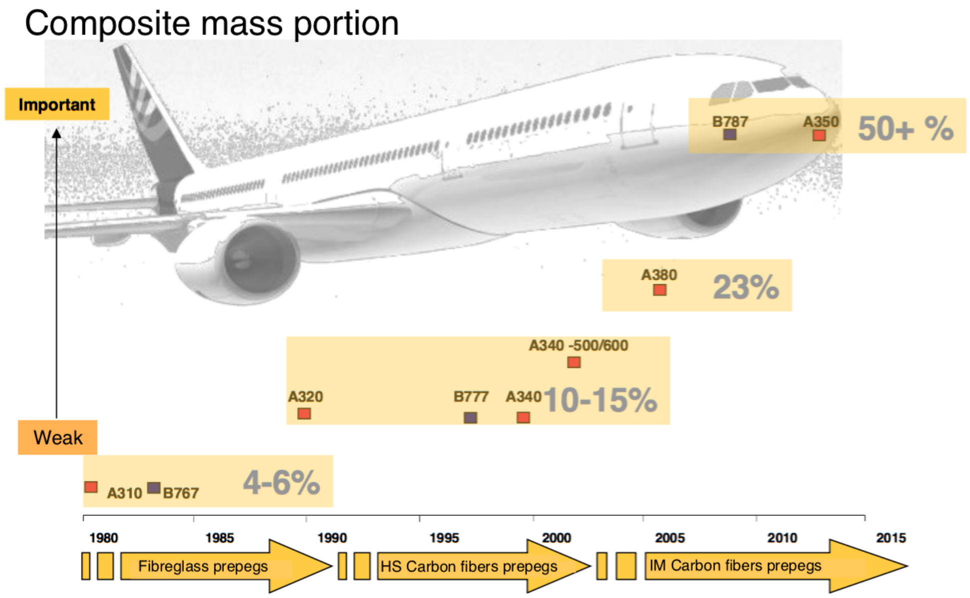

Figure 1.1: Evolution in time of the mass portion of composites in aircraft manufacturing [2].

important in the aerospace field. A good knowledge of the behavior of the materials after a significant number of cycles is therefore also crucial. Such qualification procedure can be long and costly and a good modeling of the failure mechanisms could greatly reduce the number of experiments as well as help improving the performance of the materials. Virtual testing with finite elements would therefore allow to predict the composite response under several loading conditions. To this end, a deep understanding of the mechanical response of the composite is essential, and the weakness of the composite often starts with its constituents. Polymer matrices, such as epoxy resin are often used and more specifically the RTM6 epoxy resin, which is certified for aeronautics.

This thesis focuses on the characterization and the modeling of the failure of this RTM6 resin. Experimental tests are performed to understand how cracks initiate and propagate and to quantify the material degradation through the decrease of its mechanical properties, such as stiffness and residual strength, under cyclic loading. Another goal is to link an existing failure criterion of the resin to the fracture behavior at the crack tip and to analyze if the same failure mechanism occurs. The various tests are performed on dog-bone cylindrical samples and compact tension specimens.

This report is divided into five parts. The first one describes the existing models of failure under static and cyclic loading of composites and also focuses on the elasto - viscoplastic behavior of the epoxy resins and more particularly the RTM6. The second part explains the material as well as the methods that have been used for the experimental tests. It also explains the methods used to analyze the fracture surface of the samples and the modeling of the numerical analyses with finite elements. The third part presents the obtained results from the mechanical tests and from the finite elements simulations. It also shows the micrographs of the fracture surfaces. All those results are discussed in the following chapter which presents the stress life curve of the material as well as the crack propagation rate curve in function of the amplitude of the stress intensity factor. The chapter also explains, thanks to micrographs, how the cracks grow in the material until fracture, and thanks to FEA, gives the stress state at the crack tip right before failure occurs. Finally the last chapter concludes this work by giving the main results and propositions of prospects for the future.

Chapter 2

State of the art

This chapter describes the existing knowledge of the failure mechanisms and models of composite materials under static and cycling loadings. It first gives a brief reminder of the elasto-plastic behavior. Then it describes the several mechanisms of failure in composite materials. It also explains the mechanical behavior of the thermoset polymers and focuses on the highly cross-linked epoxy resins, such as the RTM6. Finally this chapter describes the fatigue failure model of composites and the degradations that occur before fracture under cycling loading. It also focuses on the failure models of polymers used as matrix in composites.

2.1 The elasto-plastic behavior

A material subjected to a load deforms itself. At low loads, the deformations are elastic, which means they are completely reversible. Once the loads are no longer applied, the material returns to its original shape. This deformation is governed by Hooke's law, which states:

$$\sigma = E\epsilon \tag{2.1}$$

With σ the applied stress, E the Young's modulus or elastic modulus, and ϵ the resulting strain. The elastic range ends when the material reaches its yield strength. At this point plastic deformation begins. Plastic deformations are irreversible. However, a material in the plastic deformation region will first have undergone reversible elastic deformation, and thus will partly return to its original shape. Figure 2.1 shows a typical curve showing the elastic region from 0 to A, and the plastic region from A to B, where the deformation 0C remains after unloading. The slope 0A is the same as CD and is equal to the Young's modulus E.

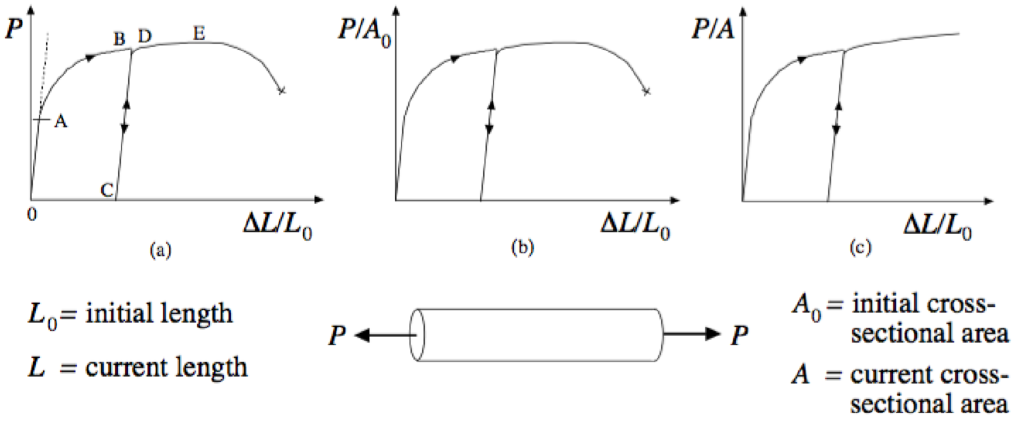

Figure 2.1: Typical load-displacement curve of a material subjected to simple tension [3].

2.2 Static failure

2.2.1 Failure model of composites

Overview of composites

There are many definitions for composite materials, but the most global one is probably: *'the combination of two or more distinctly different materials to make an improved or superior material'.* [4]. In general, a composite is composed of two phases: a reinforcing one, which has high mechanical properties such as stiffness, and a matrix one, which surrounds and supports the reinforcement material. The matrix part can also protects the reinforcement from wear and the environment. An other important factor of the composite is the interface between the reinforcement and the matrix. A laminate composite is composed of a stack of plies, several layers of fibers (the reinforcing phase) oriented in different directions as seen on figure 2.2. Thermoset resins, as RTM6, are frequently used as matrices of fiber-reinforced polymer composites. Composite materials usually have three different failure modes: fiber fracture, matrix fracture or fiber-matrix interface delamination. Fiber failure is different in compression and in tension. In compression, it is affected by the resin shear behavior

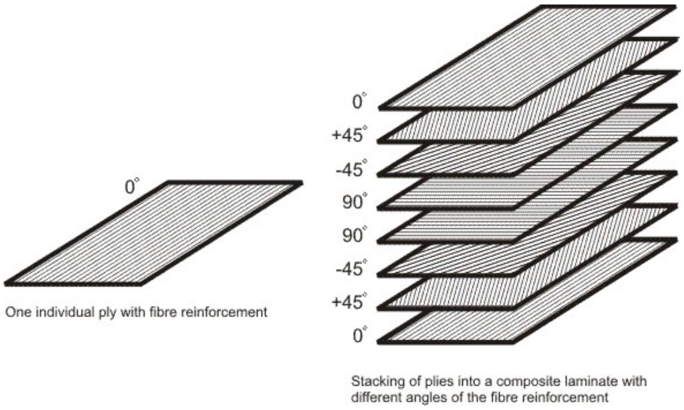

Figure 2.2: Drawing of the stacking of a laminate composite [5].

and imperfections such as the initial fiber misalignment angle and voids. In tension it is an explosive mode of failure that releases large amount of energy and causes catastrophic failure [6]. The matrix failure is also different in compression and in tension. The failure in compression is a shear matrix failure, where the failure occurs at an angle with the loading direction, whereas the failure in tension has a fracture surface normal to the loading direction [6]. Delamination between the matrix and the fracture can also occur, and significantly reduce the bending stiffness of the panels. This mode of failure has already been well studied and implemented in a commercial Finite Element code [6]. The existing models of failure, that are presented further, have a common weakness which is the intrinsic mechanism of failure of the components like matrix cracking itself.

Puck-criteria: Inter fiber fracture

The IFF, inter fiber fracture, or matrix cracking, characterizes cracks propagating very rapidly through the entire layer thickness. The crack is stopped by the fibers of the neighboring layers. These cracks can either be caused by cohesive failure of the matrix, or by adhesive failure at the fiber/matrix interface. IFF is a brittle fracture, which means a sudden separation of material without pronounced deformations in the fracturing area. Fracture is produced by a combination of normal and shear stresses, respectively, σ and τ. There exist three different modes: A and B where the cracks are "straight", and C where the cracks are "oblique"[7]. The difference between those modes lies in the inclination θ_{fp} of the fiber-parallel fracture plane. Figure 2.3 describes the increase of the risk of delamination and local buckling with the increase of this angle. When the ratio $\frac{\sigma_2^c}{\tau_{21}}$ reaches a certain value, fracture occurs under an angle $\theta_{fp} \neq 0^o$. This angle increases with the ratio $\frac{\sigma_2^c}{\tau_{21}}$ until $\pm 54^o$ for pure transverse compressive stress. An other interesting observation is that in mode A, fracture occurs before $\sigma_2^t = R_\perp^t$ or $\tau_{21} = R_{\perp\parallel}$ if σ_2^t and τ_{21} act at once. Whereas in mode B, higher shear stress τ_{21} can be sustained without fracture when σ_2^c and τ_{21} act simultaneously.

The harmless IFF (mode A) can be distinguish from the dangerous IFF (mode C)[7]. Such

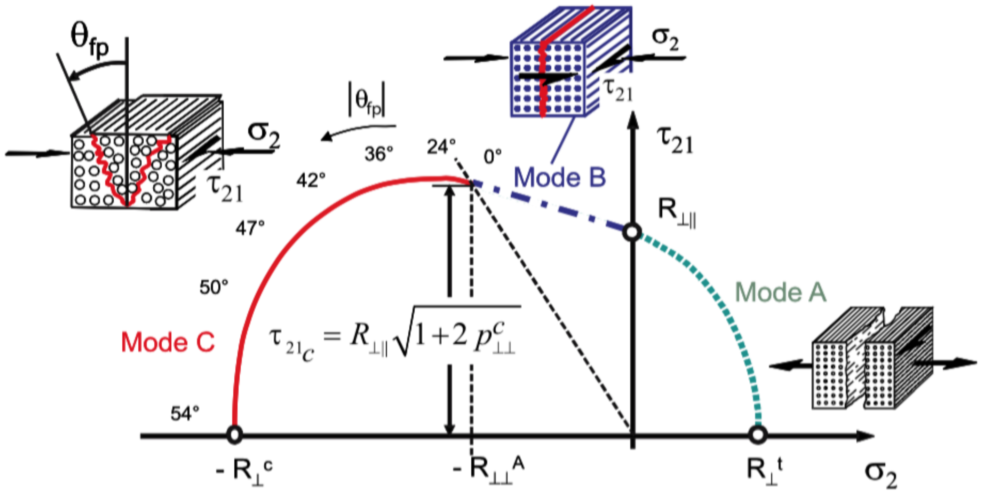

Figure 2.3: Fracture envelope for combined (σ_2,τ_{21}) stresses, fracture modes A, B, C and fracture angle θ_{fp} [8].

oblique IFF do not totally destroy the layer affected, but can seriously harm the laminate as a whole. A wedge is formed at the fracture surfaces and induces a force in the thickness direction leading to major delamination and the dismantling of the laminate, as seen in figure 2.4. Therefore, unlike most IFF, this kind of IFF must often be observed as final failure of the laminate. Long before an IFF, 45° micro-cracks caused by micro-damage can appear, but those micro cracks are stopped by the fibers to prevent the fracture of the composites, as shown on figure 2.5.

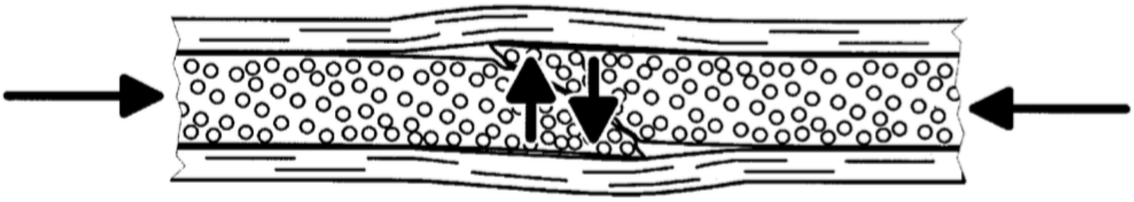

Figure 2.4: Schematic illustration of a wedge shaped transverse compressive fracture causing delamination and local buckling [7].

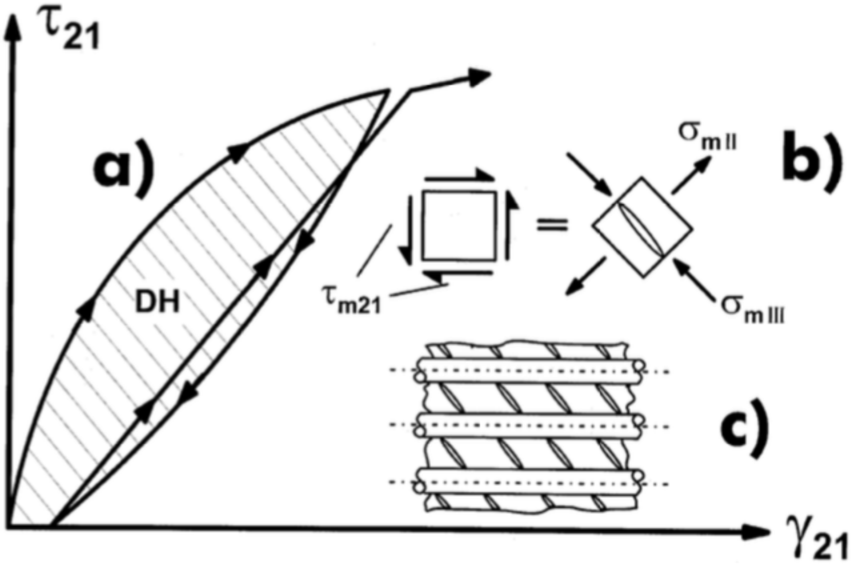

Figure 2.5: (a) Brittle micro-damage in a UD-layer caused by a shear stress τ_{21} leads to a marked damage hysteresis (DH) in a loading/ unloading cycle. (b) A shear stress τ_{m21} is acting in the matrix which can be transformed into the principal stresses $\sigma_{mII} = \tau_{m21}$ and $\sigma_{mIII} = -\tau_{m21}$. (c) The tensile principle stress σ_{mII} causes numerous 45° micro-cracks long before the fiber/matrix composite fails. The micro-cracks are stopped by fibers which in this case prevent an early fracture of the composite [7].

LaRC04

Pinho et al. [6] proposed a set of three-dimensional failure criteria for laminated fiber-reinforced composites, known as LaRC04. The criteria are based on physical models for each failure mode and can accurately predict failure envelope [9]. The main advantage of these criteria is that they take into consideration the non-linear matrix shear behavior, which is an important factor affecting strength in a general loading situation. However it does not consider the dependence of the shear stress on eventual superposed transverse stress and uses the shear stress at some strain level as the shear strength. Just as Puck et al. [7], the model for matrix compressive failure is based on the Mohr-Coulomb criterion and predicts the fracture angle [9].

Extensions of the criteria

Catalanotti et al. [10] claimed that Puck's failure criterion for transverse compression provides accurate predictions of the first ply failure load but that the prediction of failure of plies embedded in multidirectional laminates requires the use of the in situ strengths. They proposed a failure criteria that can be used to predict failure envelopes for all conceivable stress states, but has limitations regarding the out-of-plane components of the stress tensor.

Camanho et al. proposed[11] a three-dimensional invariant-based failure criteria for fiber-reinforced composites. It can predict failure in a single UD ply, but requires the analysis of strains and stresses ply-by-ply when analyzing multidirectional laminates [11]. The failure envelopes of LaRC04, Catalanotti and Camanho for AS4/55A carbon-epoxy are shown on figure 2.6. As it is the main weakness of the existing models of failure, this work focuses on the matrix phase alone, which is often a thermoset polymer. According to Koratkar and Srivastava [12] the failure mode of the polymer matrix can be either ductile or brittle, depending upon the chemistry and the curing agent used. The ductile mode is often identified by shear yielding, whereas an increase in brittle nature of the polymer shows micro-voiding

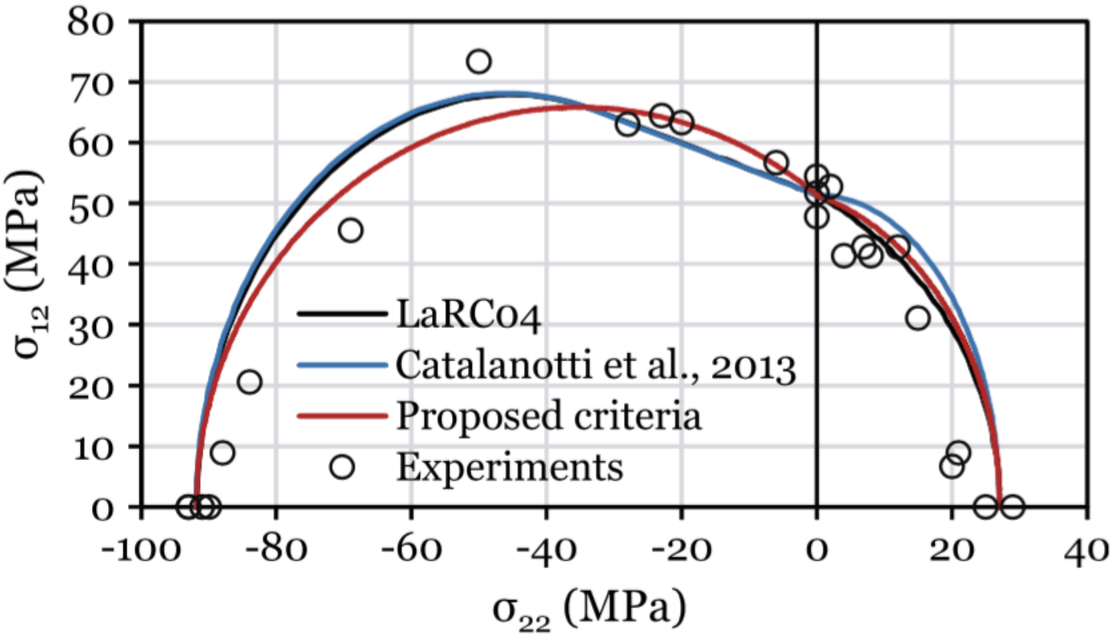

Figure 2.6: Comparison of the different $\sigma_{22} - \sigma_{12}$ failure envelopes with the experiments for AS4/55A carbon-epoxy [11].

followed by crazing. Networked polymers like epoxy usually has highly brittle failure without crazing.

2.2.2 Mechanical behavior of thermoset polymers

Elasto - viscoplastic response

The figure 2.7 shows the several stages of deformation in the intrinsic stress-strain behavior of a glassy polymer, such as RTM6 [13] :

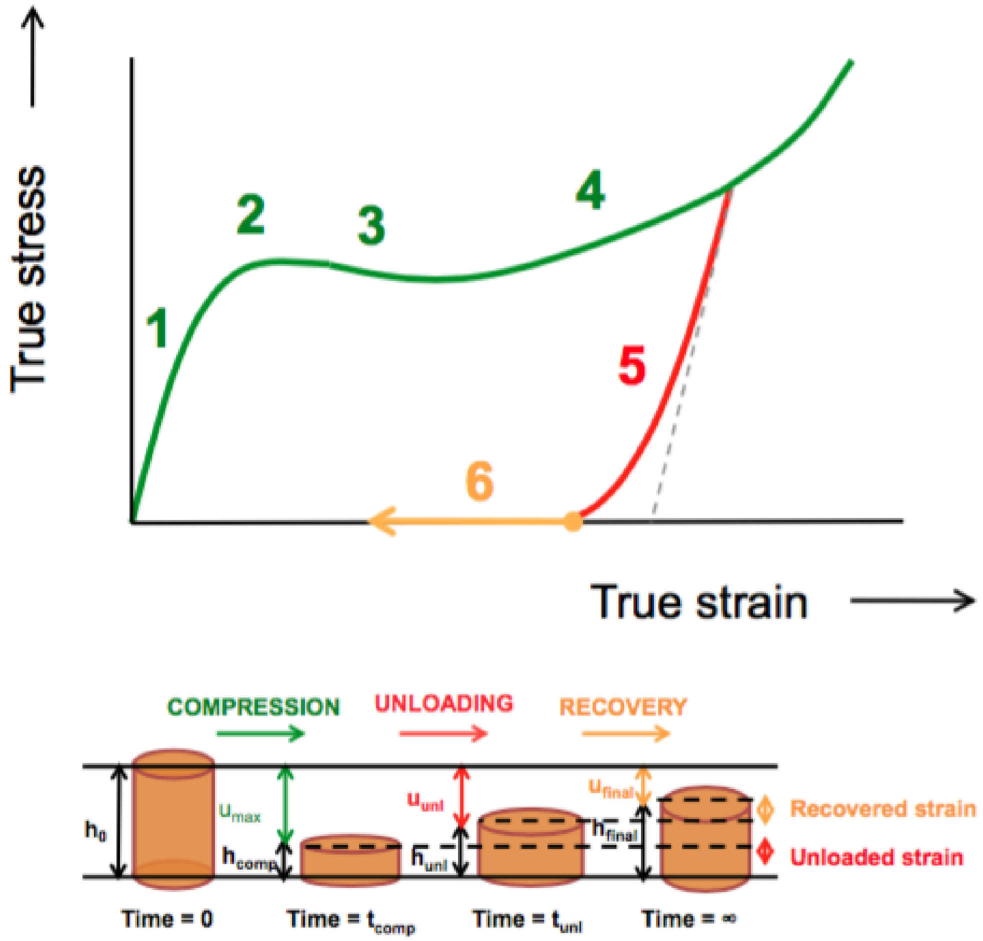

Figure 2.7: Schematic representation of the intrinsic stress-strain behavior of glassy polymers, in parallel with the corresponding compression test : 1) elastic-viscoelastic region, 2) yield transient, 3) strain softening, 4) strain hardening, 5) unloading back-stress, 6) strain recovery [13]

- 1. Elastic-viscoelastic region

  The stress-strain curve of glassy polymers starts with an elastic region, where the strain is reversible. The strain-stress relation is linear, with a slope characterized by a Young's modulus E around 1 to 4 GPa. This slope progressively decrease showing non-linear elastic response.

- 2. Yield transient

  There is a transition from elastic regime to plastic regime at the yield point, which is defined as the local maximum of the curve. The plastic yielding process occurs at that point. It physically corresponds to overcoming the activation barrier and allowing the chains to start moving along each other. This process is irreversible, and the plastic yielding can be different between compressive and tensile loadings for some polymers.

- 3. Strain softening

  A stress drop occurs just after the yielding point, the strain softening. The origin of this intrinsic phenomenon is not fully understood and still subjected to debate but it is often related to extrinsic plastic localization where the deformation keeps increasing in local shear bands.

- 4. Strain hardening

  The stress rises again at larger strains in a phenomenon called strain hardening.

  It is associated to the response of the cross-linked network which starts to prevail through chain orientation. The cross-link density is thus a significant factor that affect this phenomenon.

- 5. Back-stress during unloading

  This phenomenon is similar to the Bauschinger effect observed in metals. The unloading behavior shows a strong non-linearity. This effect is rarely mentioned in the literature and still not fully understood.

- 6. Strain recovery after unloading

  A consequence of the unloading behavior of glassy polymers is the important strain recovery after deformation.

Strain softening followed by strain hardening is a key issue in the understanding of the failure process.

2.2.3 Failure of highly cross-linked epoxy resins

In the literature, two kinds of epoxies are studied [13] :

- The resins involving low crosslink densities. These epoxies can usually be cured at room temperature and exhibit a large plastic or visco-plastic deformation before failure.

- The resins involving moderately to highly crosslink density. As the RTM6, these epoxies are ideal candidates for high performance structural applications since they exhibit high stiffness, thermal and chemical stability. The drawback is their relatively brittle behavior under positive stress triaxiality.

Failure models

There are a lot of fracture mechanisms for brittle epoxy: matrix crazing, shear banding, tearing, plastic deformation, particle caused caviation, de-bonding, plastic zone formation at crack tip, crack bridging, crack pinning, crack path deflection and others. Maiti et al. [14] proposed a cohesive model for failure of polymers:

$$T_n = \frac{\psi}{1-\psi}\frac{\Delta_n}{\Delta_{nc}}\frac{\sigma_{max}}{\psi_{init}} \tag{2.2}$$

where the subscript n refers to the normal component of the vectors T, the cohesive traction and Δ the crack opening displacement.Δ_{nc} is the critical opening displacement jump and σ_{max} is the tensile cohesive failure strength. The parameter ψ is defined as:

$$\psi = min(\psi_p, \langle 1 - \frac{\Delta_n}{\Delta_{nc}}\rangle) \tag{2.3}$$

it quantifies the evolution of the damage process. ψ_p is the previously achieved value of ψ and $\langle a\rangle = a$ if a > 0 and $\langle a\rangle = 0$ otherwise. ψ_{init} is chosen close to unity and ψ gradually decreases from this initial value to zero as the material starts failing. Figure 2.8 shows the cohesive traction-separation law for tensile failure. To preserve the damage level previously achieved, the reloading follows the unloading path rather than the initial loading path. The failure of RTM6 was studied by Chevalier et al. [15] in order to find a fracture criterion. It was shown that the RTM6 resin exhibits a much larger ductility in compression than under tensile loadings, but a brittle fracture is observed in both loading. The fracture of RTM6 was initiated when a critical principal stress was attained locally near characteristic internal defects. An aspect ratio, A_r of these microdefects was introduced and found to be between 0.26 and 0.27 to be the best predictive capability of leading to the same local MPS when fracture occurs both in uniaxial compression and uniaxial tension. FE simulations were performed with an $A_r = 0.27$ on different specimens to find an MPS around 300 MPa. When this stress of 300 MPa is reached in the vicinity of the defect, the polymer chain breaks and a crack is initiated.

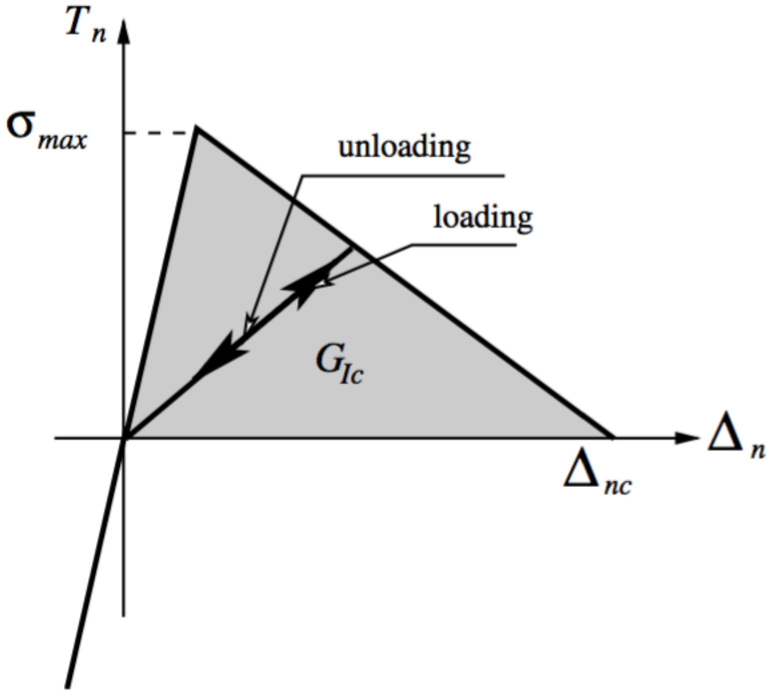

Figure 2.8: Schematic representation of the cohesive model in under monotonic loading [14].

2.3 Fatigue failure

There are only a few studies about the failure in cyclic loading of polymer matrix-based composites. The choice of studying this phenomenon and extending the failure model for monotonic loading was therefore straightforward.

2.3.1 Fatigue failure models of composites

In general, the fatigue degradation behavior of a composite laminate is characterized by a combination of matrix cracking, delamination, fiber/matrix debonding, and fiber breakage. Reifsnider [16] illustrated the development of damage during the fatigue life of a composite on figure 2.9. The matrix cracks initiate in plies under tensile stress perpendicular to the fibers. At the characteristic damage state, CDS, the number of cracks saturates and creates a pattern of regularly spaced cracks remaining undisturbed throughout the end of the life of the material. These cracks cause the delamination to form and contribute greatly to the local stress state at the delamination front, which leads to final fracture. Abdelal et al. [17] proposed a model based on a combination of an orthotropic damage model, that predicts the evolution within a single cycle and an isotropic fatigue evolution model, that predicts the magnitude of fatigue damage accumulated as a function of the number of cycles. It uses 11 parameters, of which 9 are adjusted with quasi-static lamina strength data and 2 are adjusted with fatigue data from a laminate. Therefore only limited amount of fatigue data is required.

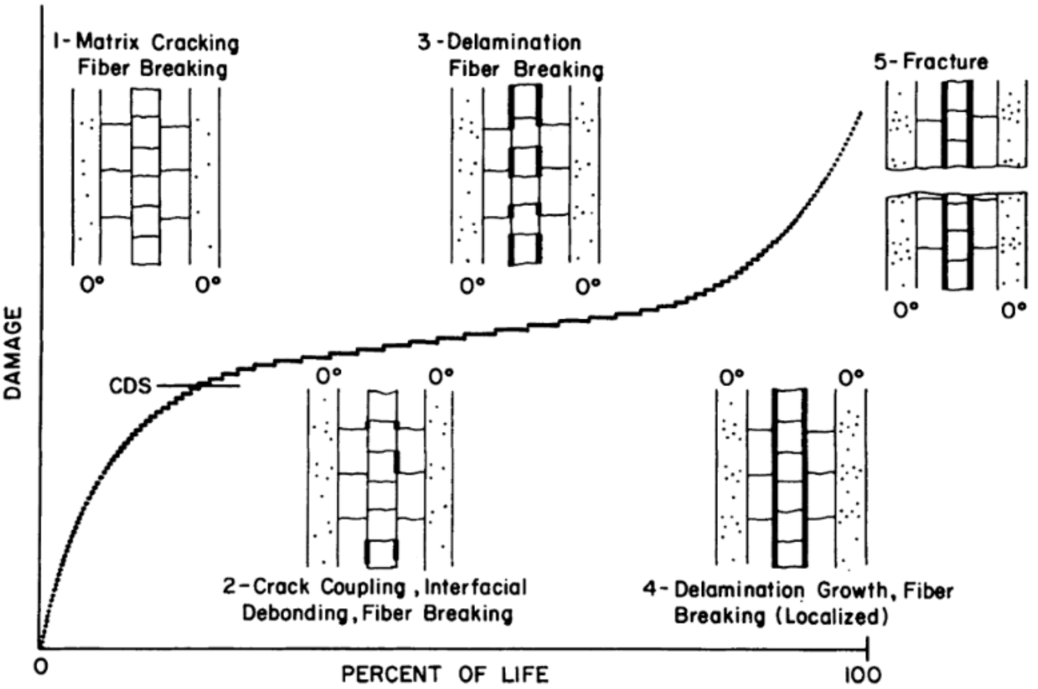

Figure 2.9: Schematic representation of the development of damage during the fatigue life of a composite laminate [16].

According to Wu et al. [18] a fatigue damage model based on the stiffness degradation is capable of describing the nonlinear damage evolution in the whole fatigue life period of the materials. In their model, the parameters are proportional to the fatigue life and are inversely proportional to the fatigue loading level.

Varvani et al. proposed a parameter based on the physics and the mechanism of fatigue cracking within three damage regions of matrix (I), fiber–matrix interface (II), and fiber (III) as the number of cycles progresses [19]. The figure 2.10 shows those three regions.

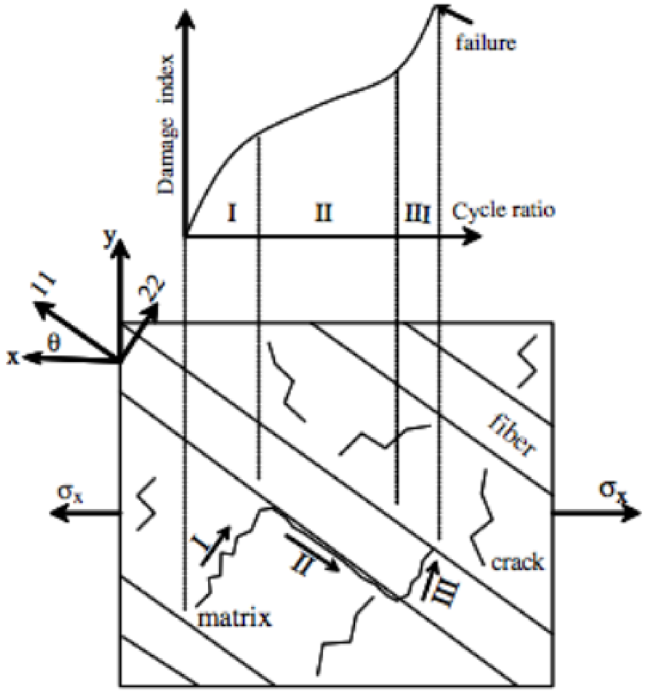

Figure 2.10: Representation of the fatigue cracking within three damage regions of matrix (I), fiber–matrix interface (II), and fiber (III) [19].

Region I

In early stage of fatigue damage, microcracks are formed from flaws within the polymeric matrix. There initiation was triggered by shear deformation within matrix. At this stage, matrix cracking is dominantly due to shear components of stress and strain. The energy based damage is defined as:

$$\Delta W_I = [\frac{\Delta\tau_{max}\Delta\frac{\gamma_{max}}{2}}{(\tau_{ult}\frac{\tau_{ult}}{G})_m}] \tag{2.4}$$

with τ_{ult} the ultimate shear strength and G the shear modulus and where:

$$\Delta\tau_{max} = (\frac{\sigma_1 - \sigma_3}{2})_{r1} - (\frac{\sigma_1 - \sigma_3}{2})_{r2} \tag{2.5}$$

$$\Delta\gamma_{max} = (\frac{\epsilon_1 - \epsilon_3}{2})_{r1} - (\frac{\epsilon_1 - \epsilon_3}{2})_{r2} \tag{2.6}$$

with $\sigma_1 > \sigma_2 > \sigma_3$ are the principal stress values and $\epsilon_1 > \epsilon_2 > \epsilon_3$ are the principal strain values. The subscripts r1 and r2 correspond to the first and the second reversals of a fatigue cycle and the subscript m denotes the matrix phase. In this region, the crack length becomes long enough to develop a shear stress at its tips leading to a fiber–matrix interface debonding.

Region III

Region III correspond to the breakage of the fibers. In this region, normal stress and strain components in fiber direction are responsible for brittle fiber failure:

$$\Delta W_{III} = [\frac{\Delta\sigma_n \Delta\epsilon_n}{(\sigma_{ult}\frac{\sigma_{ult}}{E})_f}] \tag{2.7}$$

with the subscript f referring to the fiber phase, and σ_{ult} being the ultimate tensile strength and where the normal stress range and the normal strain range are:

$$\Delta\sigma_n = (\frac{\sigma_1 + \sigma_3}{2})_{r1} - (\frac{\sigma_1 + \sigma_3}{2})_{r2} \tag{2.8}$$

$$\Delta\epsilon_n = (\frac{\epsilon_1 + \epsilon_3}{2})_{r1} - (\frac{\epsilon_1 + \epsilon_3}{2})_{r2} \tag{2.9}$$

Region II

The region II involves shear-mode cracking along the matrix-fiber interface.

$$\Delta W_{II} = [\frac{\Delta\tau_{12}\Delta\frac{\gamma_{12}}{2}}{(\tau_{ult}\frac{\tau_{ult}}{G})_m} + \frac{\Delta\sigma_{22}\Delta\epsilon_{22}}{(\sigma_{ult}\frac{\sigma_{ult}}{E})_f}] \tag{2.10}$$

where $\Delta\sigma_{22}$, $\Delta\epsilon_{22}$ the ranges of transverse stress and strain are responsible for opening the crack and $\Delta\tau_{12}$, $\Delta\gamma_{12}$ the ranges of in-plane shear stress and strain cause debonding and crack growth along the interface. The total energy-based fatigue damage parameter for GRP and CFRP composites as damage continuously accumulates over life cycles is then :

$$\Delta W = \Delta W_I + \Delta W_{II} + \Delta W_{III} \tag{2.11}$$

The Region I is the main focus in this paper since the polymer matrix alone is studied. The mechanical properties of composites have a time dependent nature, and Guedes et al. [20] studied the viscoelastic effect of the polymer matrix composites to predict their fatigue life based on an energy failure criteria. They showed that lifetime theories predict similar features between creep failure and constant stress rate failure strength curves.

Degradation due to fatigue loading

Fatigue loading gradually degrades several intrinsic properties of the materials. Wim Van Paepegem et al. [21] showed that the secant shear modulus of a glass/epoxy composite is decreasing considerably before failure and also that the amount of permanent shear strain is very large. Jain et al. [22] developed a method to statistically compare the loss of stiffness of composites under cycling loadings. The stiffness degradation was the same regardless of the fibers orientation. Wim Van Paepegem et al. [23] also demonstrated that there is a degradation of the Poisson's ratio which is much larger than that of the stiffness under cyclic loading when damage is present in a composite laminate. Daelemans et al. [24] showed that a toughening of composite laminates is possible by the addition nanofibrous interleaves. According to them, there is a mechanism of development of nanofiber bridging zones at interlaminar crossings and this mechanism occurs under static and cycling loading.

2.3.2 Fatigue failure of glassy polymers

Polymers fail in fatigue because of cycle by cycle accumulation of damage resulting from repeated non-elastic strain. A crack forms, propagates and the specimen fractures [25]. According to Janssen et al. [26], failure originates from the polymer's intrinsic deformation behavior, more particularly the true strain softening after yield, which leads to the initiation of localized deformation zones.

Nagasawa et al. [27] showed that rotary-bending fatigue for epoxy resins proceeds by way of crack nucleation, propagation of the crack and final failure of the specimen. The propagation rate of a crack and final failure of a specimen follows the general theory of fracture mechanics of elastic materials. They also showed that fatigue or strain is accumulated until a crack nucleus is created on the surface, but this strain might be reversible. Indeed, the distorted segment arrangement can return to the original state due to the contractile force of the network structure. However, if the reversible strain turns into an irreversible defect, it initiates a crack instead of returning into its original state.

2.3.3 Fatigue damaging models

Most of polymers fail in a macroscopically brittle way under cyclic loading. The primary mechanism for crack growth in polymers is the crazing of the material in a thin strip ahead of the crack tip, but this is usually not the case for thermosetting resins.

Maiti et al. [14] also formulated a cohesive model for fatigue failure. It is stated that in the case of cyclic loading, in addition to continuous per cycle crack growth as in metals, an additional crack propagation mechanism is at work for polymers. The craze zone may grow over a number of cycles before the failure of the fibrils and the crack jumps through two thirds of the craze length, giving rise to discontinuous crack growth [14]. The model involves the progressive degradation of the cohesive zone strength during reloading:

$$k_c = \frac{dT_n}{d\Delta_n} = f(N_f, T_n) \tag{2.12}$$

where k_c is the cohesive stiffness and N_f is the number of loading cycles since the onset of failure.

Figure 2.11 shows the degradation of the cohesive stiffness during cyclic loading.

A study of the damaging process of bulk adhesive, which are epoxies, was performed by AbdelWahab et al. [28]. They found two damage constants fitting the fatigue tests data for low cycles (<10000 cycles).

Walander et al. [29] proposed two approaches too study the fatigue damage of an adhesive layer. A first one using the Paris'law and the second using a damaging law with three parameters where a zone of damage, which size extension depends on the stiffness of the adherents, evolves at the crack tip. This means that not only the state at the crack tip governs the rate of crack growth.

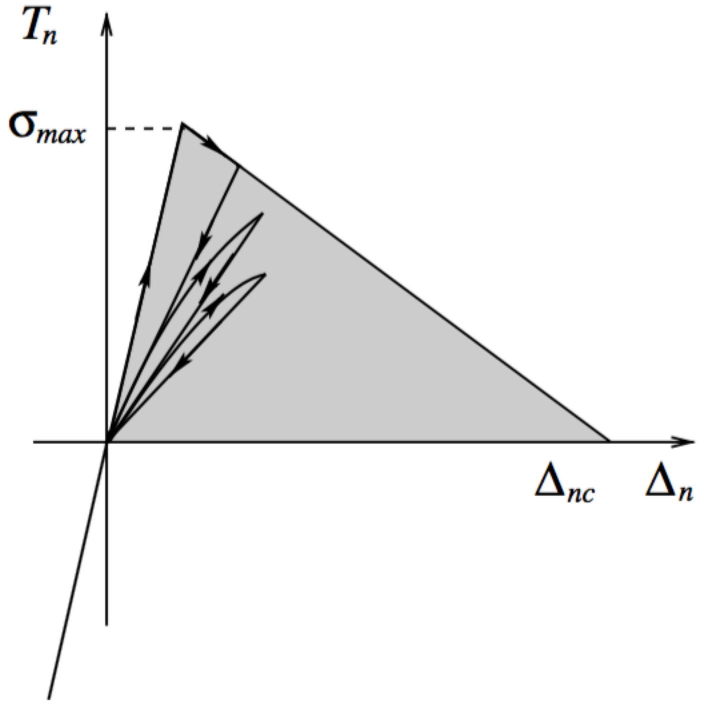

Figure 2.11: Schematic representation of the fatigue failure cohesive model showing the decay of the cohesive stiffness during reloading events [14]

2.4 Present work

This works focuses on the comparison of the criterion explained in section 2.2.3 on the failure of highly crosslinked epoxy resins under monotonic tensile and compressive loadings and the results obtained from FE simulations and experiments in cyclic loading. The mode of failure in cyclic loading under tensile-tensile load of cylindrical specimens and of pre-crack specimens is studied in order to find an extension of the criterion.

Chapter 3

Materials and methods

This chapter first describes the tested material. It explains the curing process and the machining of the different samples tested in the frame of this work. It also shows pictures of the samples as well as their dimensions. Then it explains the methods of the mechanical testing under static and cycling loading. The preparation for the analysis with a microscope of the fracture surface is also explained in this chapter and finally the model and the material law used for the finite element analysis is presented.

3.1 Materials : RTM6

The material used in this research is the HexFlow ©RTM6. It is a mono-component epoxy resin provided by Hexcel. It is used as matrix of RTM composites and fulfill the requirements of aerospace and space industry. It is an amine-cured thermoset composed of a stochiometric premixed system of a tetra-functional epoxide precursor (TGMDA) and a blend of two di-amine hardeners (MDEA and MMIPA) [13]. It is a highly crosslinked material which has a good stiffness of 3 GPa (at room temperature), and also good thermal stability properties. The resin is first poured in the molds then degassed to take out as much air trapped as bubble as possible. Different molds were used:

- Thin glass test-tube molds for the tensile specimens
- Thick rectangular molds for the CT specimens

The resin is then cured following a cycle illustrated in figure 3.1. In this cycle there are three different steps:

- Degassing:
  The filled molds are placed in an oven at 90°C. The vacuum is then reached progressively to remove all the air bubbles trapped in the resin. This step should last 75 minutes.
- Curing:
  The molds are transfered to a programmable air ventilated oven where the temperature increases from 90°C to 130°C with a heating ramp of 2°C/min. Once the temperature of 130°C is reached, the oven is kept at that temperature for three hours. During this step the resin becomes solid-like.

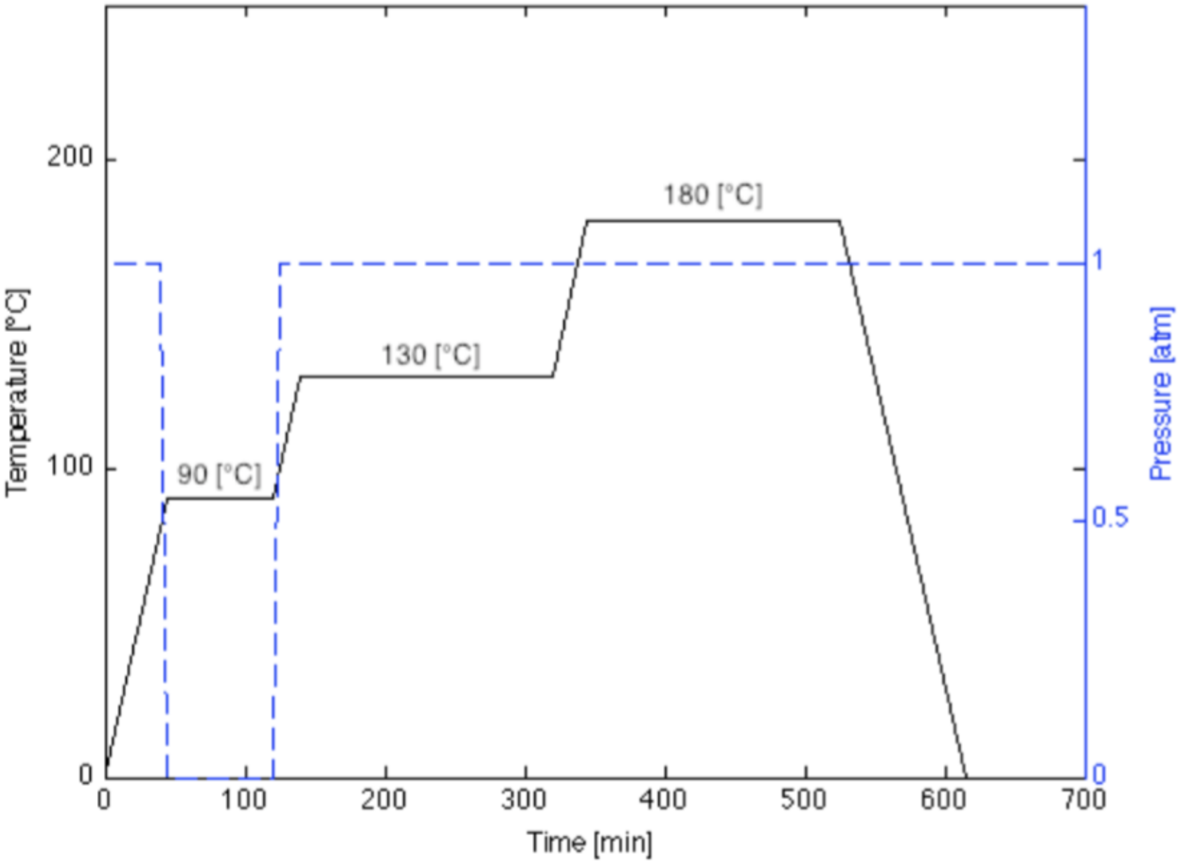

Figure 3.1: Scheme of the optimal curing cycle for the production of thick rectangular samples of RTM6. This curing process is composed of: a) Degassing step under vacuum - 75min at 90°C b) Curing step - 180min at 130 °C and c) Post-curing step - 180min at 180 °C. Heating ramps are of 2 °C/min. Heating ramp for cooling is of 10°C/min [13].

- Post-curing:
  A post-curing is necessary to ensure a good homogeneity of polymerization through the thickness of the sample, to achieve the requested high degree of conversion and to give an identical thermo-mechanical history to every samples [13]. This step consists in increasing the temperature to 180°C with a heating ramp of 2°C/min. Once the temperature is reached, the oven is kept at that temperature for three hours, then cooled down to room temperature with a cooling ramp of 10°C.

3.2 Mechanical testing

The cured resin in the thin glass test-tube mold, see figure 3.2a, was machined to form cylindrical dog-bone tensile specimen as seen in figure 3.2b, while the rectangular slab of resin was machined to form CT specimens. Two different CT specimens were machined: thick ones, as seen in figure 3.3a, for the measurement of the fracture toughness and thin ones for measurement of the crack propagation, as seen in figure 3.3b.


(a) (b)

Figure 3.2: Pictures of a) cured resin from a thin glass test-tube mold and b) an unpolished dogbone sample.

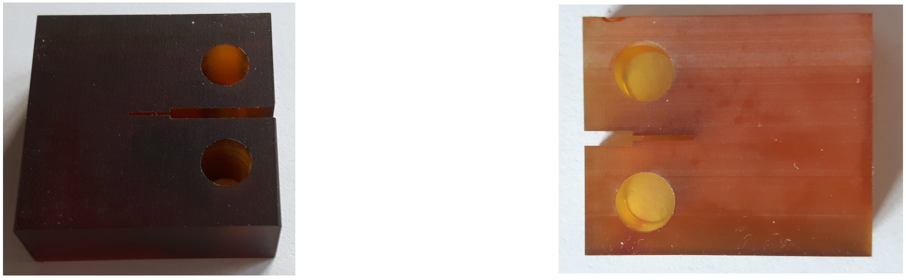
(a) (b)

Figure 3.3: Pictures of a) a thick CT sample and b) a thin CT sample.

3.2.1 Samples

Dog-bone specimens

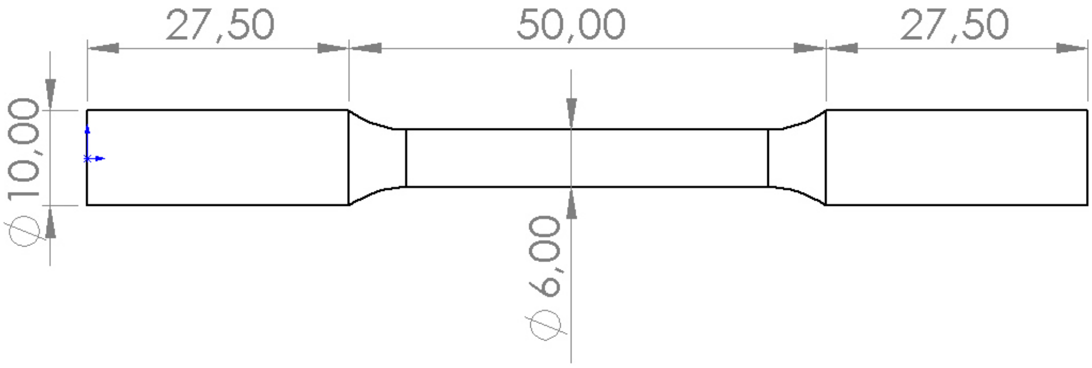

Figure 3.4: Dimensions of the dog-bones specimens in [mm].

The cylindrical specimens were machined for tensile testing, but another polishing was needed to assure that the failure would occur inside the specimen rather than on the outside surface. This polishing step was very important in order to study the failure of the material. It was carried out on a turning machine, first with 1200 grit SiC abrasive paper, then with some diamond paste. Several sizes of diamond paste were consecutively used: 15 μm, 9 μm, 3 μm and 1 μm. The result is shown on figure 3.5.

Figure 3.5: Picture of a polished dogbone sample.

CT Specimens

Two slabs of resins of different thickness were produced to respectively manufacture two sets of CT specimens. The thick ones, with a deep notch, for static testing, and the thin ones, with a smaller notch, for fatigue testing and crack propagation analysis. Standard norms ASTM D 5045-99 and ASTM E 647-11 were used to decide on the dimensions of the samples. The dimensions for the thick specimens followed the standard as seen on figure 3.6. Where:

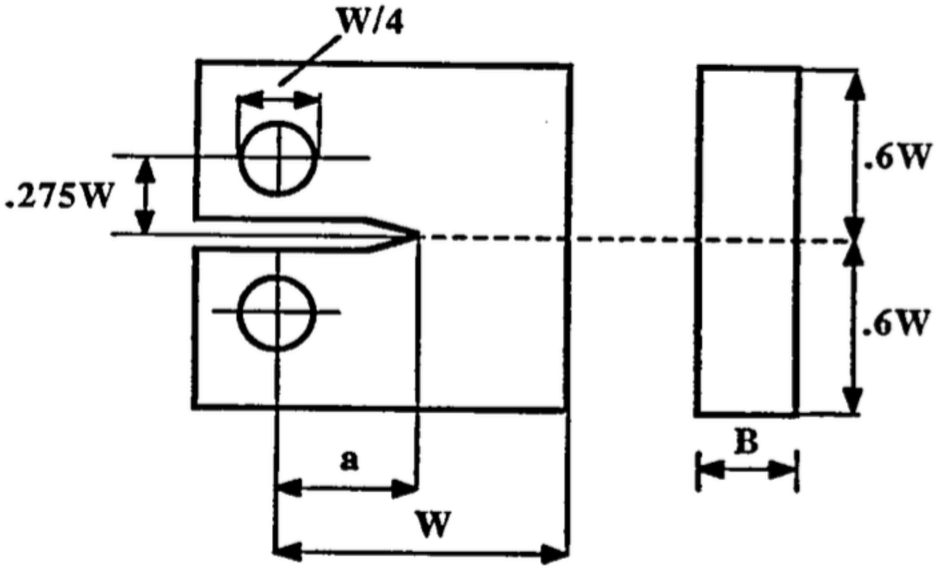

Figure 3.6: Standard dimensions of CT specimens [30]

.

- W = 24.4 mm
- B = 12.2 mm
- a = 12.2 mm

The dimensions for the thin specimens were also supposed to follow the standard, but ended up machined a bit smaller than expected. The true dimensions are represented on figure 3.7. The main differences between the thick specimens and the thin ones are that the thin ones have a width twice smaller and a length crack almost three times smaller. The dimensions of the thin CT specimens regarding the figure 3.6 are as follow:

- W = 22.8 mm

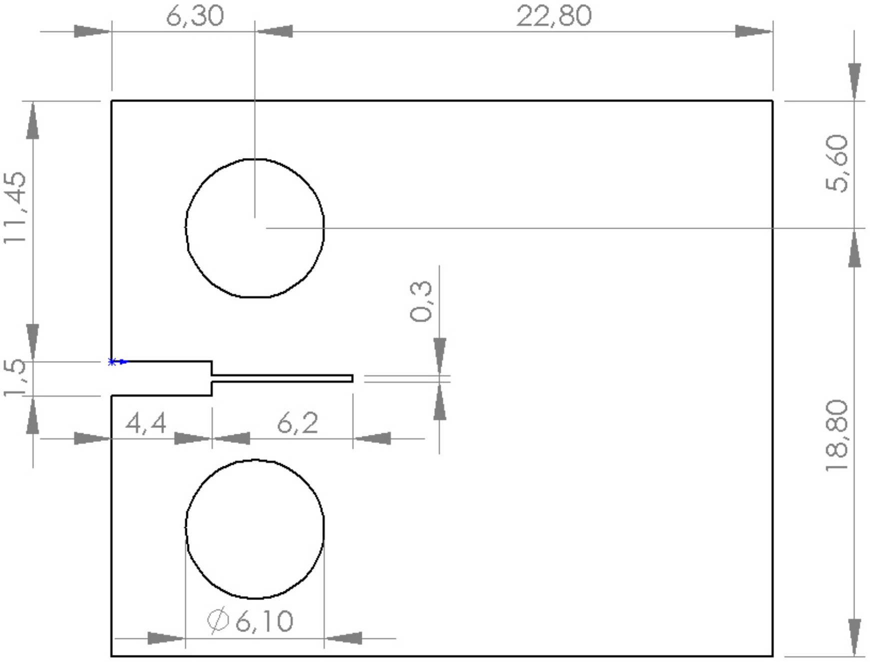

Figure 3.7: Dimensions of the thin CT specimens in [mm].

- B = 6.1 mm
- a = 4.3 mm

Pre-cracking

Both of the specimens were also manually pre-cracked with a razor blade introduced in the notch. The length of those pre-cracks were about 300 to 400 μm. This pre-cracking is shown on figure 3.8 and is more deeply explained in section 5.1.

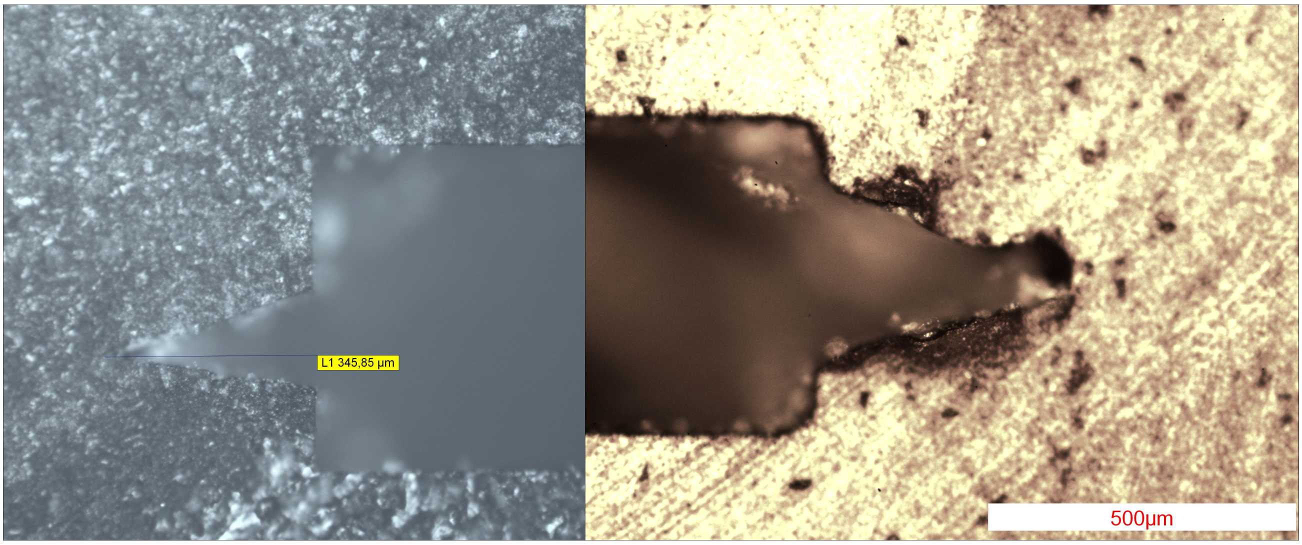

(a) Precrack of a thin specimen. (b) Precrack of a thick specimen.

Figure 3.8: Optical microscope pictures of the precracking of the CT samples.

3.2.2 Static

Tensil testing

The behavior in tension has been characterized at CSR of 0.001 /sec, performed on a screw-driven Zwick Z250 universal testing machine with a 250 kN external load cell. An extensometer measured the strain of the samples. Three specimens were used.

Compact tension specimens

The testing was performed on a screw-driven Zwick Z250 universal testing machine. Three thick CT specimens were used and three thinner specimens were also used to ensure the same fracture toughness would be determined for both samples. A clip-on was used to measure the crack mouth opening displacement. As the results were not satisfactory, new tests were performed on three other thick CT specimens and on three other thin CT specimens. The reason of the first unsatisfactory results more than likely lies in the pre-cracking step, where the length of the pre-crack was too small.

3.2.3 Fatigue

Tensile testing

The behavior in tension has been characterized at a frequency of 5 Hz, performed on an Instron 50kN testing machine. Several maximum loads were tested : 40%, 50% and 60% of the stress at failure. A stress ratio of R=0.1 was used. Three specimens were used for the 50% and 60% testing, and two specimens were used for the 40% testing. The tests were performed until fracture, but for the tests at 40% of the stress at failure, the samples didn't break. Residual strength tests were then performed on the Zwick Z250 machine.

Compact tension specimens

The behavior in tension has been characterized at a frequency of 0.5 Hz, performed on an Instron 50kN testing machine. To avoid excessive test durations, as the crack started propagating at a rate of $10^{-8}\frac{mm}{cycle}$, the samples were tested under different loads, progressively increasing. Most of the time, they were tested two hours, therefore 3600 cycles, at each load. The maximum loads were starting at 30N to finish at 50N with an increase of 2.5 N each time. When approaching the critical load, around 47.5 N, the samples were tested for a longer time, until failure occurred. A stress ratio of R=0.1 was used every time.

3.3 Electronic microscopy

An analysis of the fracture surface of the different samples tested was performed using micrographs obtained on a scanning electron microscope (SEM). In order to see the fracture surface of the broken samples, several steps were necessary to make the resin conductive. Indeed, the epoxy resins are not conductive materials, and it is mandatory to have a path for electrons from the analysed surface to the sample holder in order to have images from the microscope. The broken samples were first placed on stands with silver lac applied with a brush. The observed surface was linked to the nil-potential mass by the silver lac, applied all over the height of the observed specimen. A coating of gold was then applied on the fractured surface of each sample by cathodic sputtering in a coating machine. This was done during one minute at a voltage of 45mV.

3.4 Finite elements analysis

3.4.1 Model

A 2D model, with plane strain elements, is represented on figures 3.9a and 3.9b. It has been created with Abaqus for both the thick and the thin specimens. The dimensions of the true samples are respected and the pre-crack is introduced in the model as a seam with a contour integral. A dynamic implicit step was used and the loads obtained with the experimental tests were used, with an amplitude of loading over the whole time of the test. The mesh of the samples is represented on figure 3.10. Circular lines centered on the crack tip were used to obtain a finer mesh near the crack tip. To allow the mesh to be regular and focused, the “swept meshing” technique was used near the crack tip while the rest of the model is free meshed using the “medial axis” meshing algorithm. The meshes were mainly composed of quadrilaterals and at the crack tip of collapsed quadrilaterals. The singularity at the crack tip was characterized by a mid-side node parameter of 0.25. A new refined mesh, shown on figure 3.11 was also used for the last simulations to increase the reliability of the model. This meshing was inspired from Simulia [31].

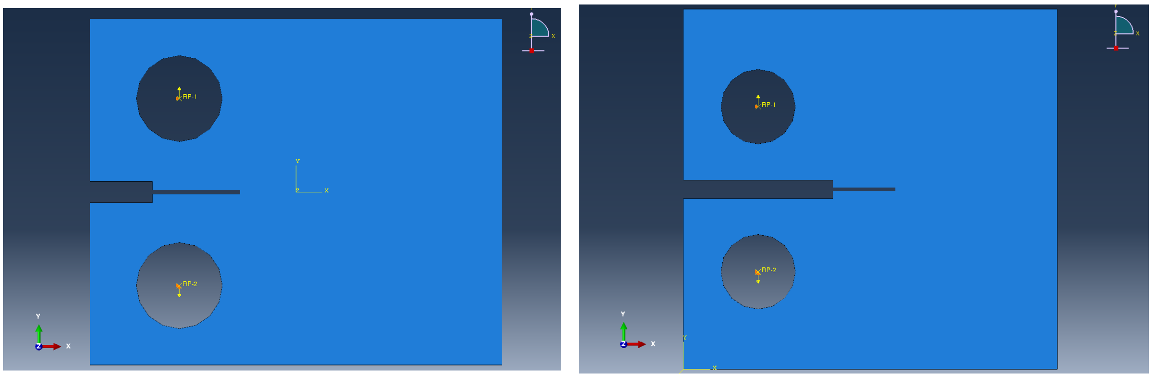

(a) (b)

Figure 3.9: Models for the numerical simulations of a) a thin specimen and b) a thick specimen.

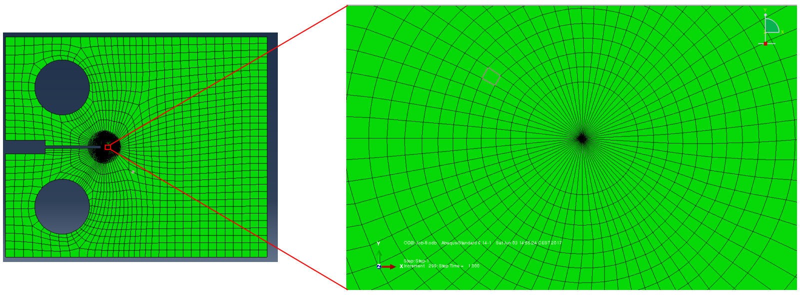

Figure 3.10: Mesh of the thin specimens.

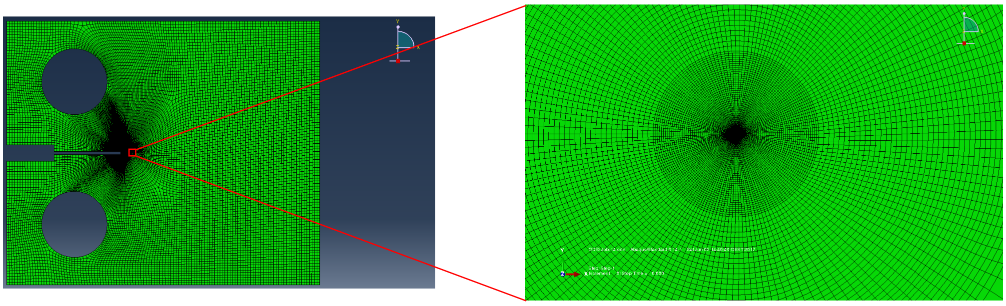

Figure 3.11: Refined mesh of the thin specimens.

3.4.2 Material law

The elastic properties of RTM6 were given to the model: the Young's modulus E=3GPa and the Poisson's ratio $\nu = 0.34$. Plastic properties were also given for some simulations to study the plasticity at the crack tip. The Drucker-Prager yield criterion was used with an angle of friction of 7.86, a flow stress ratio of 1 and a dilation angle of 0. The stress-strain curves developed by Chevalier et al. [32] for several strain rates (from 10^{-12} to 10^{2} /sec) were used.

Drucker-Prager Yield criterion

A yield criterion, or yield surface, is a hypothesis giving the limit of elasticity of a material under any combination of stresses. The Drucker–Prager yield criterion is a three-dimensional pressure-dependent model that can estimate the stress state at which the material undergo plastic yielding. It was established as a generalization of the Mohr-Coulomb criterion. This criterion can be expressed as:

$$\sqrt{J_2} = \lambda I_1 + \kappa \tag{3.1}$$

where J_2 is the second invariant of the stress deviator tensor and I_1 is the first invariant of the stress tensor. λ and κ are materials constants. The invariants are respectively defined as:

$$I_1 = \sigma_1 + \sigma_2 + \sigma_3 \tag{3.2}$$

$$J_2 = \frac{1}{6}[(\sigma_1 - \sigma_2)^2 + (\sigma_1 - \sigma_3)^2 + (\sigma_3 - \sigma_1)^2] \tag{3.3}$$

where σ_1, σ_2 and σ_3 are the principal effective stress.

In the stress space, the Von Mises criterion describes a right circular cylinder. It is also the case for the Drucker-Prager criterion when $\lambda = 0$, but when $\lambda > 0$ it describes a right-circular cone, as seen in figure 3.12. The parameters λ and κ can be obtained from standard compression triaxial tests an be expressed in terms of internal friction angle and cohesion intercept [34]:

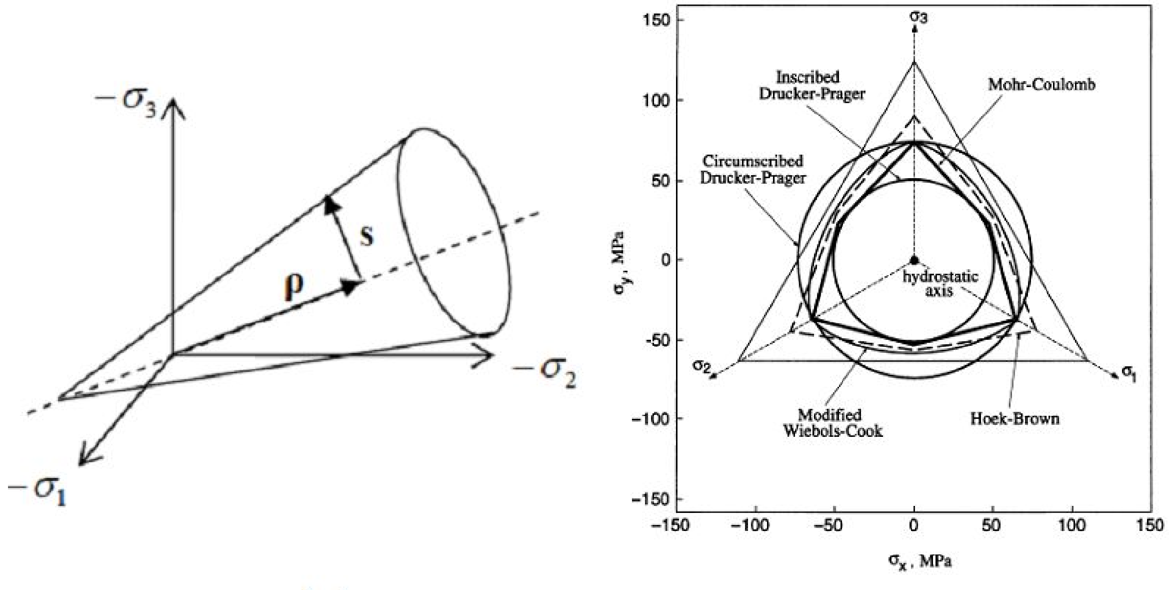

(a)

(b)

Figure 3.12: (a) The Drucker-Prager criterion, (b) Yield envelopes for Circumscribed Drucker-Prager and Inscribed Drucker-Prager criterion [33]

$$\lambda = \frac{2\ sin\ \psi}{\sqrt{3}\ (3 - sin\ \psi)} \tag{3.4}$$

$$\kappa = \frac{6\ c\ cos\ \psi}{\sqrt{3}(3 - sin\ \psi)} \tag{3.5}$$

where c is the cohesion intercept and ψ the internal friction angle. Or it can be expressed in terms of σ_t and σ_c, respectively the true stress in uniaxial tension and uniaxial compression:

$$\lambda = \frac{1}{\sqrt{3}} \frac{\sigma_t - \sigma_c}{\sigma_t + \sigma_c} \tag{3.6}$$

$$\kappa = \frac{2}{\sqrt{3}} \frac{\sigma_t \sigma_c}{\sigma_t + \sigma_c} \tag{3.7}$$

The Drucker-Prager criterion is useful because of its simplicity and its smooth. However it tends to overestimates the volumetric part of plastic strain, and therefore the strength of the material. This criterion also does not provide accurate predictions when one or more principal stresses are tensile [34].

Chapter 4

Results

This chapter first introduces the experimental imprecisions that may have occurred during the testing and the difficulties encountered with the testing machines and the equipment used. It then describes all the results obtained during the mechanical testing as well as during the finite element simulations. Finally the last part of this chapter shows the fractography, the micrographs obtained with the SEM of the fracture surfaces of the broken specimens, and the measurement of the different zones and specific elements that have been observed.

4.1 Experimental imprecisions and difficulties

Before giving all the results of the experiments, it is needed to explain the imprecisions that may have been made, along with the difficulties encountered during the several testing. First of all, the thin CT specimens were not exactly machined to meet the Standard norms ASTM D 5045-99. As seen in section 3.2.1 the height and the width were a bit smaller than wanted.

The method of pre-cracking was another factor that could have had a big impact on the results. The introduction of the razor blade was done manually, and therefore all the samples were different from each other. The length of the pre-crack, but also the opening at the tip of the crack, as well as the homogeneity of the pre-crack along the width of the specimen varied for each specimen.

Finally, the Instron 50kN testing machine had some issues regarding the requested load. Indeed, the applied load was, most of the time, smaller than the requested one. Moreover, the applied load would progressively decrease with time and drift back to a value of 45 N, and the testing had to be relaunched every once in a while to ensure a load rather constant.

4.2 Static

4.2.1 Tensile testing

The load at which the three tested samples failed are shown in table 4.1. The average value of 2465 N was used as a threshold for the fatigue testing. Figure 4.1a shows the stress-strain curves of the samples. The Young's modulus, which is equal to the slope of the linear behavior, as seen in figure 4.1b was found to be around 3 GPa, as expected[35].

	Load at failure [N]	Stress at failure [MPa]
Sample 1	2666.68	99.82
Sample 2	2206.29	81.88
Sample 3	2526.13	94.89
Average	2466.37	92.2

Table 4.1: Results of the tensile testing under quasi static loading

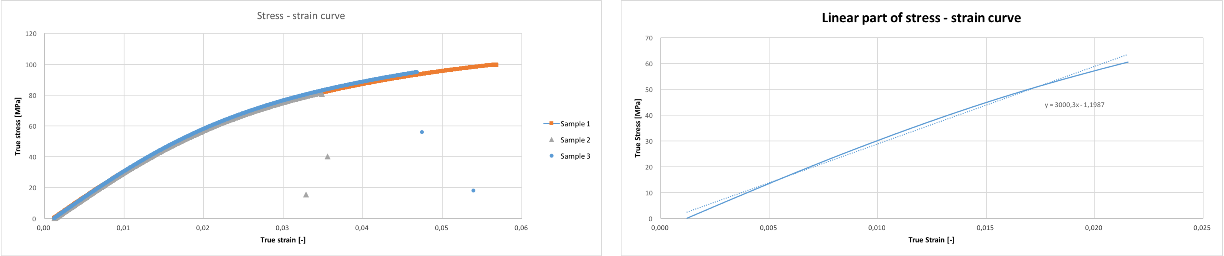

(a) (b)

Figure 4.1: a) Stress-Strain curve of the dog-bone samples. b) Linear part of the stress-Strain curve of the dog-bone sample 1. The dashed line is a linear interpolation showing the value of E, the Young's modulus.

4.2.2 Fracture toughness determination

Mechanical testing

The fracture toughness can be calculated from the load at failure and the dimensions of the specimen. The formula and method are as follow [30]:

$$K_Q = \frac{P_q}{BW^{1/2}} f(x) \tag{4.1}$$

where (0.2 < x < 0.8) and with:

$$f(x) = \frac{(2+x)(0.886 + 4.64x - 13.32x^2 + 14.72x^3 - 5.6x^4)}{(1-x)^{\frac{3}{2}}} \tag{4.2}$$

Where :
P_Q = load in kN
B = specimen thickness in cm
W = specimen width in cm
a = crack length in cm
$x = \frac{a}{W}$

To be sure that a valid K_{Ic} has been determined, a conditional K_Q needs to be calculated first. This K_Q has to be consistent with the size of the specimen. On figure 4.2a, the line AB

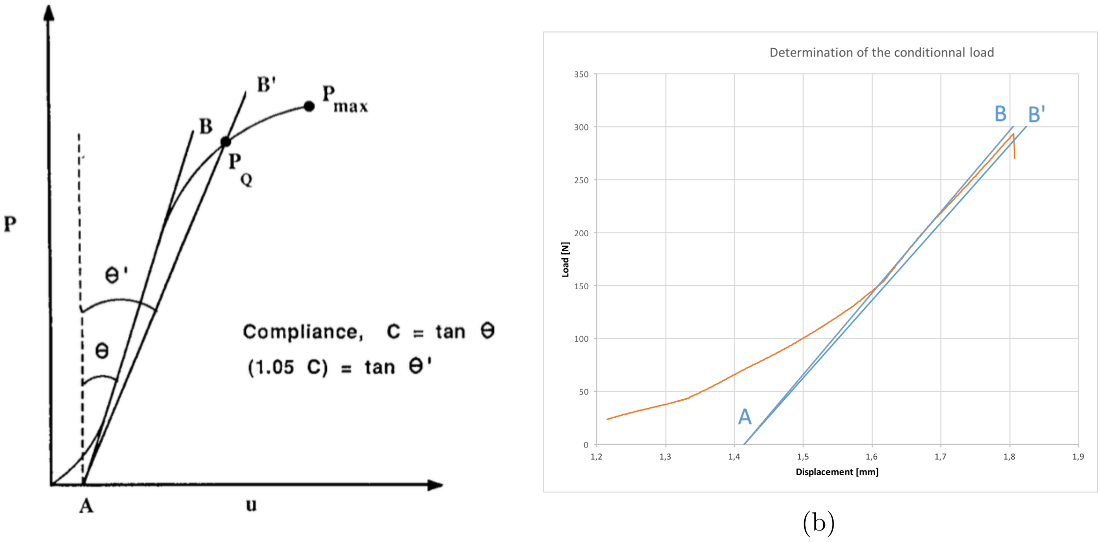

(a)

(b)

Figure 4.2: a) Theoretical model of determination of P_Q and of its validity [30] and b)Determination of the P_Q from the mechanical tests and of its validity.

gives the initial compliance and AB' gives a compliance 5 % greater than AB. In figure 4.2b, P_{max} falls inside the lines AB and AB' and therefore according to [30], has to be used as P_Q in the calculation of K_Q. Once the K_Q is calculated, it is needed to assure its validity. This is done with these conditions [30]:

$$Criteria = 2.5(\frac{K_Q}{\sigma_y})^2 \tag{4.3}$$

where σ_y is the yield stress. If Criteria is smaller than B, a and (W-a), than $K_Q = K_{Ic}$. For each test, the conditional fracture toughness has been validated. The fracture toughness can also be expressed in terms of fracture energy[1]:

$$G_c = \frac{(1-\nu^2)K_{Ic}^2}{E} \tag{4.4}$$

According to Castellani et al. [36] there is a relation between the opening displacement at the crack mouth and the crack length:

$$\frac{a}{W} = C_0 + C_1U_x + C_2U_x^2 + C_3U_x^3 + C_4U_x^4 + C_5U_x^5 \tag{4.5}$$

With:

$$U_x = \frac{1}{(\frac{BEV_x}{P})^{1/2} + 1} \tag{4.6}$$

Where V_x is the crack mouth opening displacement measured by the clip-on. And the

---

[1] The specimens are always in plane strain conditions.

coefficients for the measurement locations used being:

$$\begin{aligned} C_0 &= 1.0010 \\ C_1 &= -4.6695 \\ C_2 &= 18.460 \\ C_3 &= -236.82 \\ C_4 &= 1214.9 \\ C_5 &= -2143.6 \end{aligned} \tag{4.7}$$

Thick CT

Figure 4.3 shows the load - clip-on opening curve of the three tested samples. They all show similar curves. The summary of the results from the testing as well as the calculated values of the fracture toughness and the crack length are listed on table 4.2. As the values of the fracture toughness seemed too high compared to literature [13], [35], three other samples were tested with deeper pre-cracks. Figure 4.4 shows the load - clip-on opening curve of the three new tested samples. Once more, they all show similar curves, but the load at failure is smaller than the three first samples tested. The summary of the results from the new testing as well as the calculated values of the fracture toughness and the crack length are listed on table 4.3. The crack length is very close to the value of 12.2 mm, measured on the specimen before testing, which confirms the accuracy of the used formula.

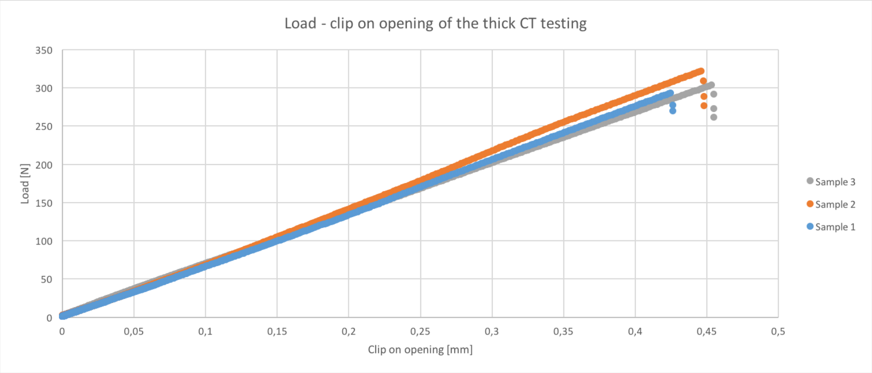

Figure 4.3: Plot of the load over the clip-on opening for the three thick CT samples.

	Load at failure [N]	K_{Ic} [MPa$\sqrt{m}$]	G_c [$\frac{J}{m^2}$]	Clip-on [mm]	Crack length a [mm]
Sample 1	293.41	1.3629	555.7	0.425	12.01
Sample 2	322.31	1.4978	671.2	0.446	11.76
Sample 3	303.64	1.4094	594.3	0.4534	12.19
Average	306.45	1.42	607	0.44	11.99

Table 4.2: Results of the testing under quasi static loading of the thick CT specimens

Thin CT

Figure 4.5 shows the load - clip-on opening curve of the three tested samples. The summary of the results from the testing as well as the calculated values of the fracture toughness and the crack length are listed on table 4.4. The 3 samples gave results all very different from

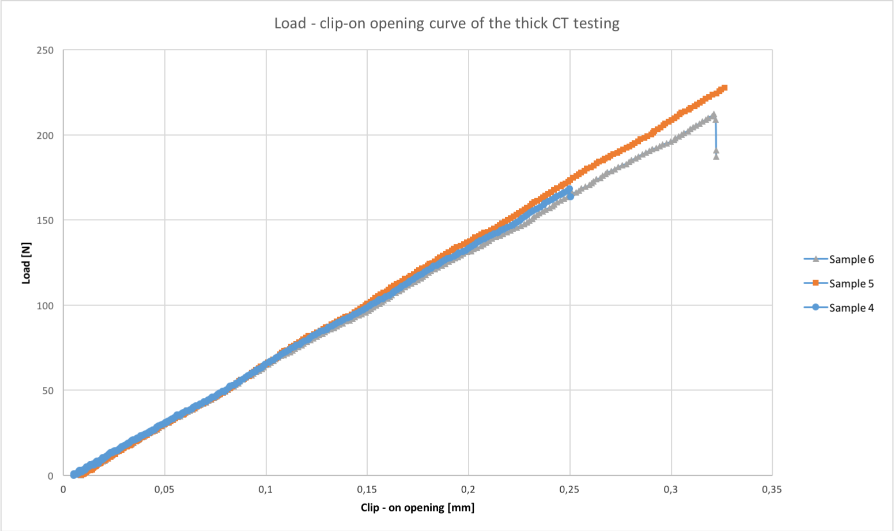

Figure 4.4: Plot of the load over the clip-on opening for the three new thick CT samples.

	Load at failure [N]	K_{Ic} [MPa$\sqrt{m}$]	G_c [$\frac{J}{m^2}$]	Clip-on [mm]	Crack length a [mm]
Sample 4	168.24	0.7871	182.7	0.249	12.15
Sample 5	227.42	1.0631	338	0.326	11.97
Sample 6	212.17	0.9885	290.9	0.321	12.26
Average	202.6	0.946	267.76	0.299	12.13

Table 4.3: Results of the testing under quasi static loading of the thick CT specimens

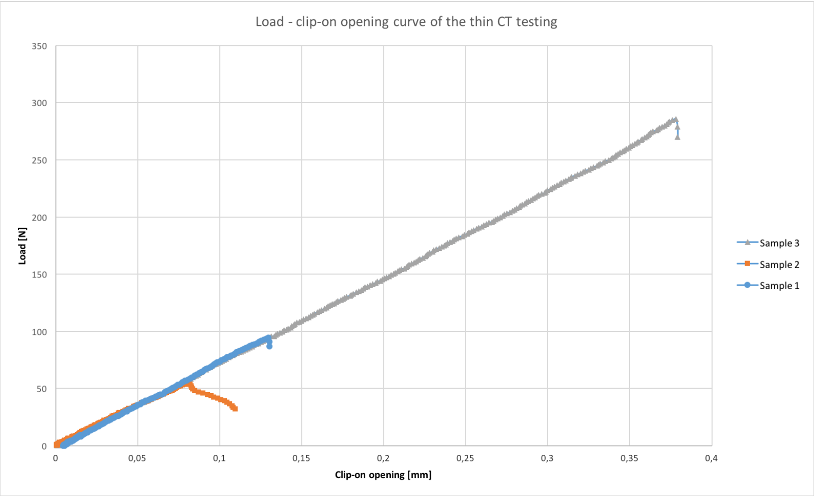

Figure 4.5: Plot of the load over the clip-on opening for the three thin CT samples.

each other and therefore were not satisfactory. The calculated crack length was also too high compared to the 4.5 mm measured on the samples. Therefore new tests were performed on three new samples with deeper pre-cracks. Figure 4.6 shows the load - clip-on opening curve of the three tested samples. The clip on probably slipped for sample 2 testing and therefore the values of the clip-on and the crack length are wrong. However the load at failure is correct. The sample 2 has therefore not been taken into account for the calculation of the

	Load at failure [N]	K_{Ic} [MPa$\sqrt{m}$]	G_c [$\frac{J}{m^2}$]	Clip-on [mm]	Crack length a [mm]
Sample 1	94.58	0.43	56.1	0.1298	6.92
Sample 2	54.45	0.25	18.2	0.0814	7.46
Sample 3	285.5	1.30	508.5	0.3780	6.69

Table 4.4: Results of the testing under quasi static loading of the thin CT specimens

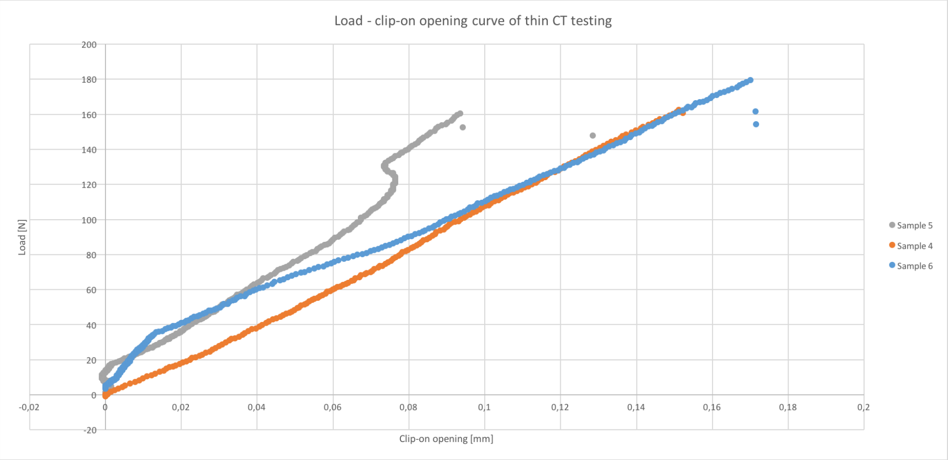

Figure 4.6: Plot of the load over the clip-on opening for the three new thin CT samples.

average of the clip-on displacement and the crack length. The summary of the results from the testing as well as the calculated values of the fracture toughness and the crack length are listed on table 4.5. Again, the crack length is very close to the value of 4.5 mm, measured on

	Load at failure [N]	K_{Ic} [MPa$\sqrt{m}$]	G_c [$\frac{J}{m^2}$]	Clip-on [mm]	Crack length a [mm]
Sample 4	160.6	0.76	170.9	0.1511	4.34
Sample 5	160.5	0.76	170.9	0.094	0.97
Sample 6	179.5	0.84	213.9	0.17	4.48
Average	166.87	0.78	184	0.16	4.41

Table 4.5: Results of the testing under quasi static loading of the thin CT specimens

the specimen before testing, which confirms the accuracy of the used formula. The fracture toughness of the thin CT is close to the fracture toughness of the thick CT, but it is a bit smaller.

4.2.3 Finite element analysis

A dynamic implicit simulation was performed under LEFM to find the stress intensity factor at the load of failure of the samples. The values are listed on table 4.6. 3D simulations were also performed giving similar values, and thus confirming the reliability of the results. A dynamic implicit simulation was performed under EPFM, with the Drucker-Pracker hardening and softening behavior. As the Drucker-Pracker curves were time dependent, an amplitude of the load was given in function of the time, obtained from the experimental tests. The simulations never converged with the Drucker-prager curves with a crack defined as a seam. A new model was then built with a triangle crack, as seen on figure 4.7. This model gave the

	Load [N]	Fracture toughness [MPa$\sqrt{m}$]	Fracture energy [$\frac{J}{m^2}$]	Clip-on [mm]
Thin CT	166.87	0.91	247.77	0.11
Thick CT	202.6	0.94	264.37	0.22

Table 4.6: Results of the FE simulations of the CT specimens, based on the load at failure from the experiments.

same exact values of fracture toughness as the model with a seam crack, which validates the reliability of the model. For this model, a dynamic explicit simulation was possible, and the maximum principal stress at the crack tip before propagation of the crack was found to be 243 MPa. This result is shown on figure 4.8.

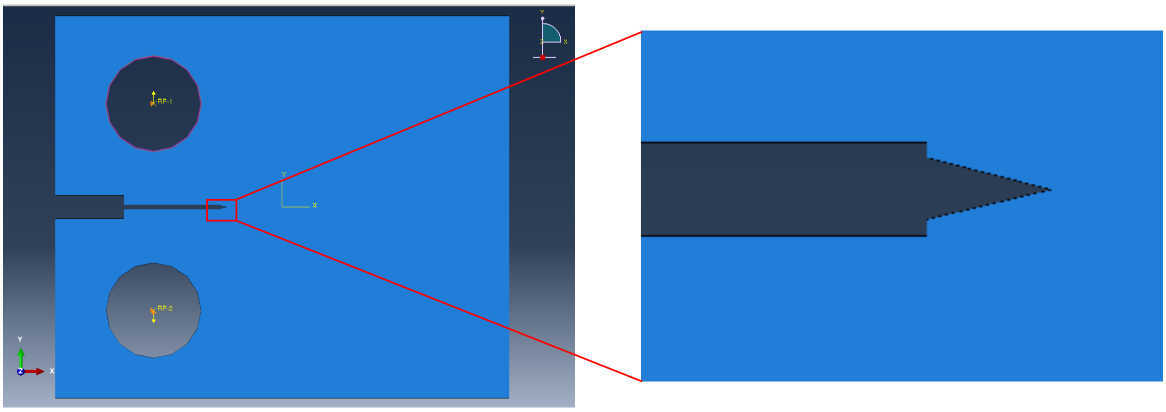

Figure 4.7: Numerical model of a thin CT sample with a triangle pre-crack.

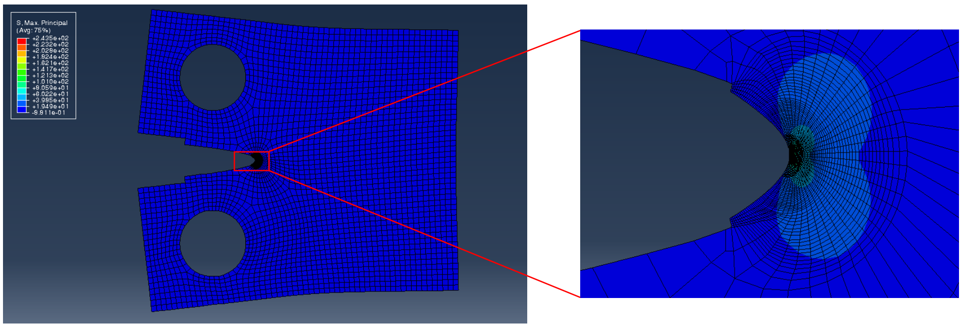

Figure 4.8: FEA of a triangle crack showing the maximum principal stress at the crack tip.

4.3 Fatigue

4.3.1 Tensile testing

From the value found in section 4.2.1 of 2465 N, the values of maximum loads were calculated as 60%, 50% and 40% of this value. The specimens tested at 40% of the load at failure did not fail, and residual strength tests were performed for each sample. Table 4.7 shows the number of cycles without failure at some specific applied loads, as well as the residual strength of the specimens when they didn't break under cyclic loading. The samples 7 and 8 were tested under static loading to compare their residual strength with the strength of the samples that did not undergo cyclic loading. The figure 4.9 shows the stress-strain curves of the three samples already presented in section 4.2.1 as well as the curves of the samples tested under 986N in cyclic loading. The sample 7 has a similar curve as the samples broken under static loading, whereas sample 8 has a small stiffness drop. Its Young's modulus was calculated to be 2.5 GPa, compared to 3GPa for the other samples. The stresses at failure of samples 7 and 8 were however consistent with the samples from section 4.2.1.

R = 0.1	Maximum Load applied [N]	Number of cycles	Residual strength [N]
Sample 1	1600	448	/
Sample 2	1479	500	/
Sample 3	1479	1254	/
Sample 4	1232.5	3588	/
Sample 5	1232.5	11953	/
Sample 6	1232.5	3929	/
Sample 7	986	>1201525	2630
Sample 8	986	>1723553	2603

Table 4.7: Results of the tensile testing under cyclic loading of respectively 60%, 50% and 40% of the average tensile load of failure presenting the applied the load, the number of cycles without failure and the residual strength of the specimen when no failure occurred under cyclic loading.

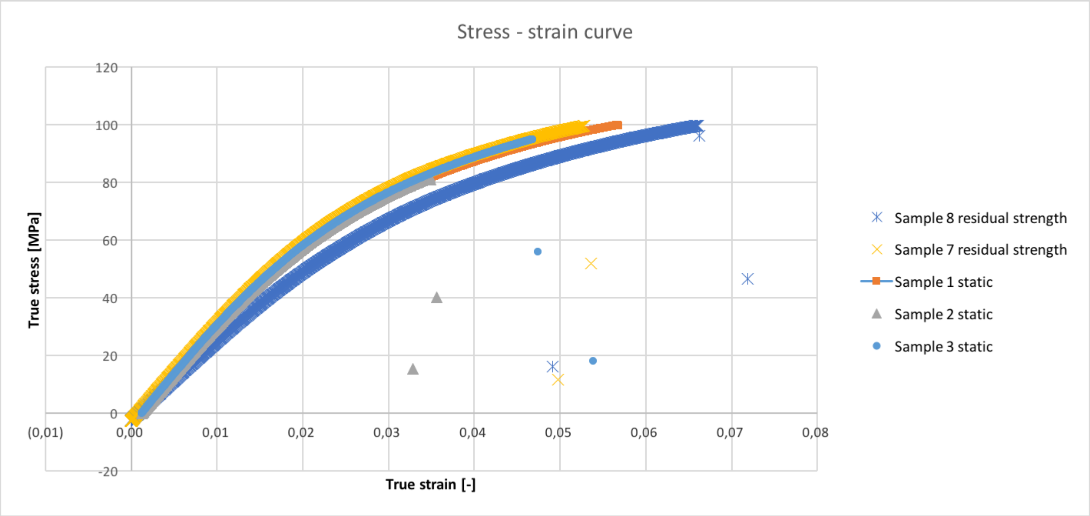

Figure 4.9: Stress-Strain curve of the dog-bone samples broken under static loading and the samples 7 and 8 broken under static loading after cyclic loading of 986N.

4.3.2 Fatigue crack propagation

Mechanical testing

A lot of samples were tested, but only three samples are presented in this work, since they showed the most relevant results. Samples 17 and 18 were broken during fatigue testing, after undergoing respectively 81334 and 33274 cycles. Sample 22 was broken under quasi-static loading, after 46394 cycles in cyclic loading. The number of cycles is to be taken carefully, since the testings of the samples were performed at different loads, as explained in section 3.2.3. To study the rate of propagation of the crack, the opening displacement at the crack mouth was measured. Since the data were not perfectly smooth, a curve fitting the data was plotted. Both the data and the fit are represented in figure 4.10a and 4.10b. Figures 4.11a and 4.11b show the evolution of the crack length along with the number of cycle. On both samples the crack first grows rapidly to reach a rather stable plateau and then another growth is observed until fracture. The fast growth may be due to the different loads applied consecutively which are greater every time. It is also explained by the fact that the

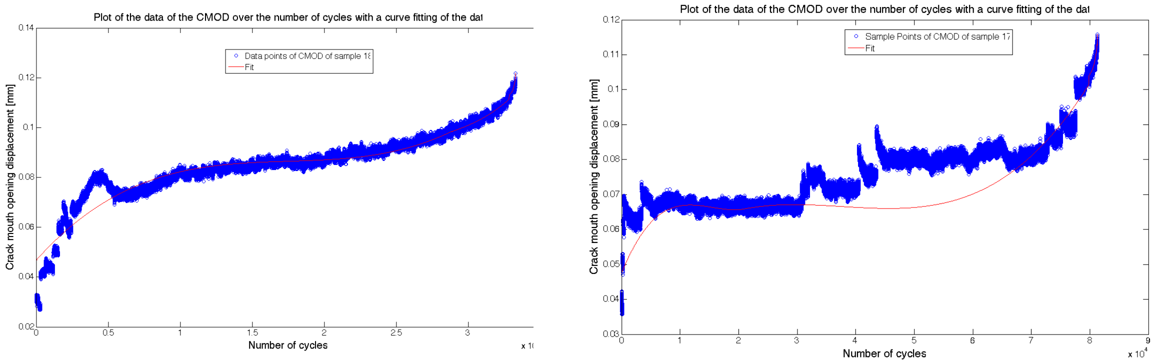

(a) (b)

Figure 4.10: Plot of the data of the displacement measured by the clip on over the number of cycles with a curve fitting the data for a) sample 18 and b) sample 17.

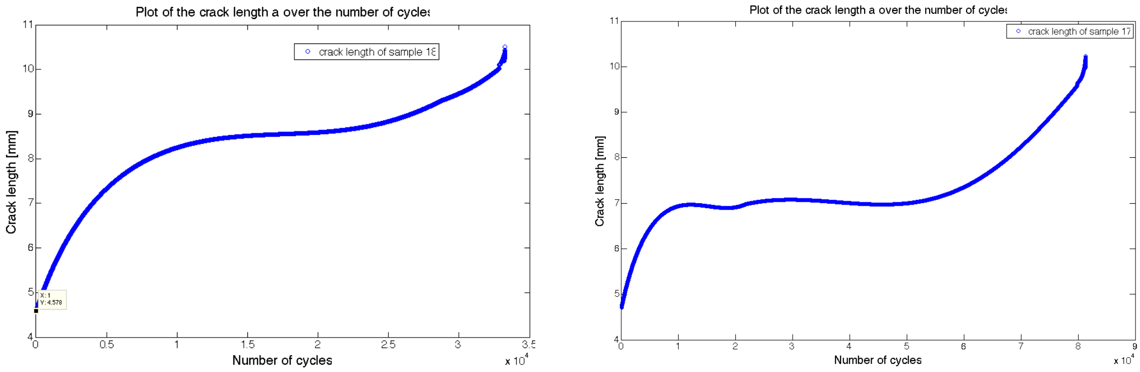

(a) (b)

Figure 4.11: Plot of the crack length over the number of cycles for a) the sample 18 and b) the sample 17.

razor-blade pre-crack is not completely uniform along the width of the sample, and must first grow to have the same length uniformly. This may also come from micro-cracks that are not propagating as explain further in section 5.3.2. The final growth lies in the propagation of the main crack as the stress intensity factor increases.

The formula 4.1 is used again to find the stress intensity factor related to the maximum load applied. The amplitude of the stress intensity factor is then calculated by:

$$\varDelta K = K_{max} - K_{min}$$

And since:

$$R = \frac{K_{min}}{K_{max}} = 0.1$$

Thus:

$$\varDelta K = 0.9 K_{max}$$

The amplitudes of the stress intensity factor as a function of the number of cycles of the samples 18 and 17 are represented on figures 4.12a and 4.12b.

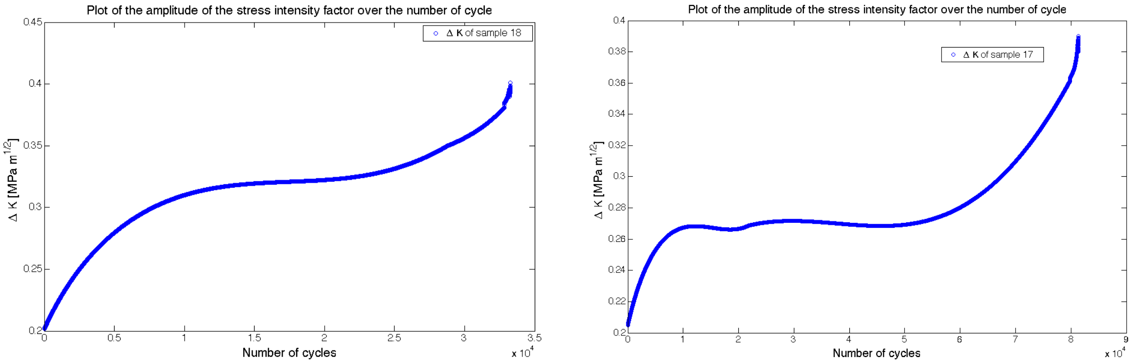

(a) (b)

Figure 4.12: Plot of the amplitude of the stress intensity factor over the number of cycles for a) the sample 18 and b) the sample 17.

According to Koratkar and Srivastava [12] and also by Alstadt et Al. [37], the fatigue crack growth behavior of polymers, is traditionally divided in three discrete regimes: First, the initiation of the crack growth described by the threshold value, $\varDelta K_{th}$. Second, the regime of stable crack propagation and finally, the regime of fast and instable crack growth described by $\varDelta K_{Ic}$. The initiation of fatigue cracks are usually due to surface flaws and inclusions. The regime of stable crack growth is governed by the Paris law:

$$\frac{da}{dN} = C \varDelta K^m$$

where a is the crack length and C and m are two constants which depend on the testing parameters including moisture, temperature, loading frequency, and the stress ratio. This law shows that the propagation rate per cycle $\frac{da}{dN}$ is directly proportional to the stress intensity factor range $\varDelta K$. The fatigue resistance of a material is lower when the rate of

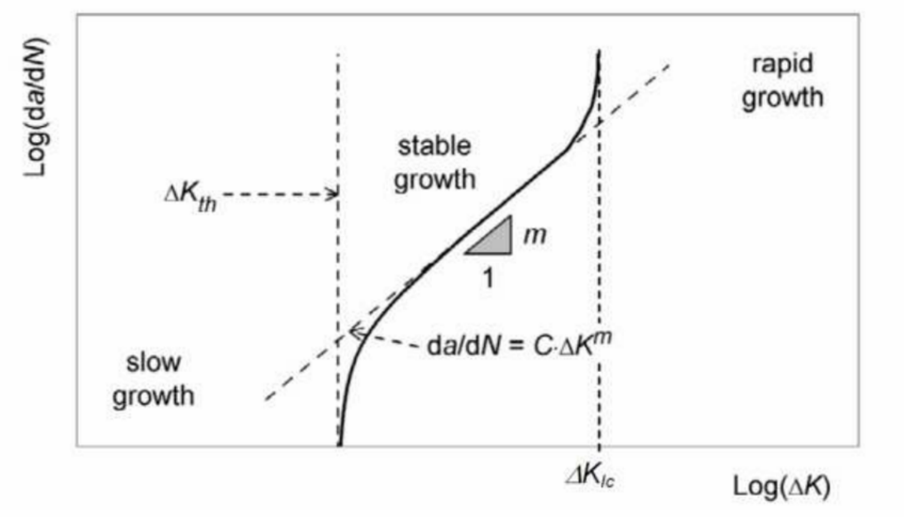

Figure 4.13: Identification of the three regimes: Initiation, stable crack propagation and instable crack growth [38].

propagation is fast and small values of the Paris exponent m mean high resistance to fatigue crack propagation. As seen in figure 4.13, the fatigue crack propagation (FCP) behavior is typically illustrated by a log-log plot of the fatigue crack propagation rate, $\frac{da}{dN}$, as function of the stress intensity factor ratio, ΔK, acting at the crack tip.

Similar curves were drawn on figures 4.14b and 4.14b for the tested samples and the important values are listed in table 4.8. The Paris slope on figure 4.14b was not well represented due to the problems of the machine explained in section 4.1, and therefore the fit of the curve was a bit inaccurate, but the value of the Paris slope was well calculated with the true data.

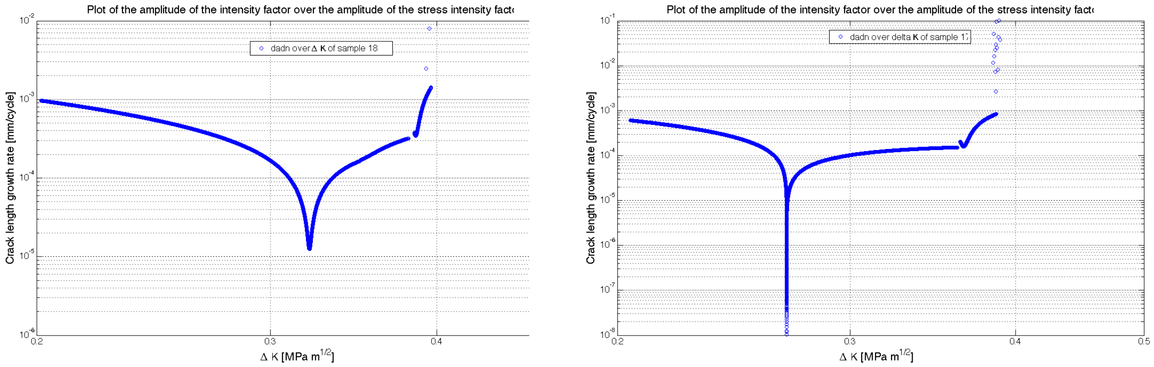

(a) (b)

Figure 4.14: Plot of the crack propagation rate over the amplitude of the stress intensity factor for a) the sample 18 and b) the sample 17.

The sample 22 was also tested under cycling loading but not until failure. It was then broken under static loading. The same curves as for samples 17 and 18 were drawn and the rate of of the crack length growth is presented on figure 4.15. The crack length at the end of the test is 8mm and the amplitude of the stress intensity factor is 0.34 MPa$\sqrt{m}$. This

R = 0.1	ΔK_{th} [MPa $\sqrt{m}$]	$\Delta K_{critical}$ [MPa $\sqrt{m}$]	Paris slope
Sample 18	0.32	0.4	11.43
Sample 17	0.27	0.39	13.25

Table 4.8: Summary of characteristic ΔK values obtained by FCP testing.

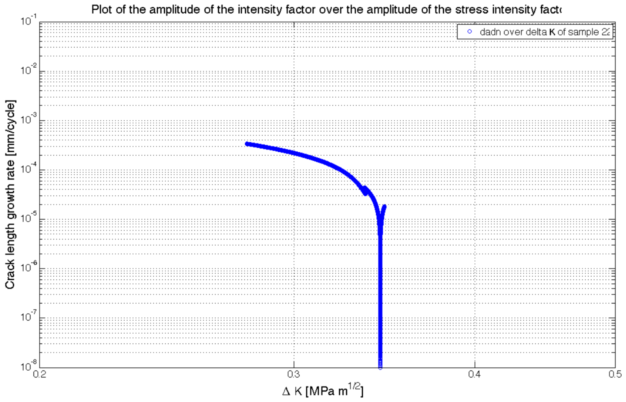

Figure 4.15: Plots for the sample 22 of the crack propagation rate over the amplitude of the stress intensity factor.

sample was then broken under static loading and figure 4.16 shows its stress - strain curve as a comparison of the curves of the samples broken under static loading without a fatigue pre-cracking. The values obtained are shown on table 4.9. A stiffness drop is observed

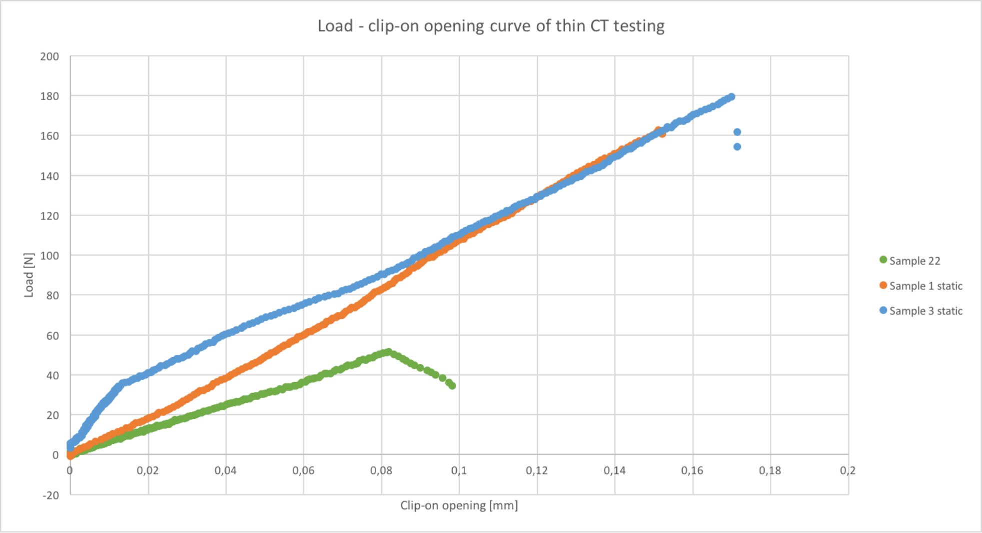

Figure 4.16: Plot of the stress - clip-on opening curve under static loading of the sample 22 with a fatigue pre-crack, compared to stress - clip-on opening curves of the samples broken under static loading without fatigue pre-cracking.

and the fracture toughness has been determined as 0.42 MPa$\sqrt{m}$. A decrease in the load is observed at the end of the curve, where the crack goes from 7.8 mm to 11.2 mm.

	Load at failure [N]	K_{Ic} [MPa$\sqrt{m}$]	G_c [$\frac{J}{m^2}$]	Clip-on [mm]	Crack length a [mm]
Sample 22	51.4	0.42	53	0.0813	7.87

Table 4.9: Results of the testing under quasi static loading of the sample 22 with a fatigue pre-crack.

4.3.3 Fractography

Dog-bone specimen under static loading

The images provided by the SEM show several areas with different features. Those areas are schematically represented on figure 4.17. The initiation of failure starts from a defect and a smooth zone is always present next to this defect. Two types of smooth zones were observed as seen on figure 4.18. The sample 1 static shows a smooth zone of type A, a long thin sharp area. The sample 2 static and sample 3 static show a smooth zone of type B, almost circular with a pac-man shape. The difference between the smooth zone of type A and B probably lies in the orientation of the zone on the fracture surface. Around the smooth zone, a mirror zone, also rather smooth, is present. This mirror zone is not exactly centered around the defect, but is bigger on the side of the smooth zone. Between the smooth zone and the mirror zone, there is a very small area with riverlines, as observed on figure 4.19. At the edge of the mirror zone, no distinct stop lines are observed, but small parabolas are gradually distinguished. The ones closer to the mirror zone face the defect, but the further away from the defect they are, the more chaotic the orientation of the parabolas becomes. The last zone is a very rough and chaotic area. All the important areas are represented on figure 4.20. In each parabola, a secondary defect of about 500 nm wide is present. A zoom of the main defect of the sample 1 is shown on figure 4.21 and a close view of the smooth area surrounding the defect of the sample 3 is shown on figure 4.22. The region far away from the initiation is shown on figure 4.23.

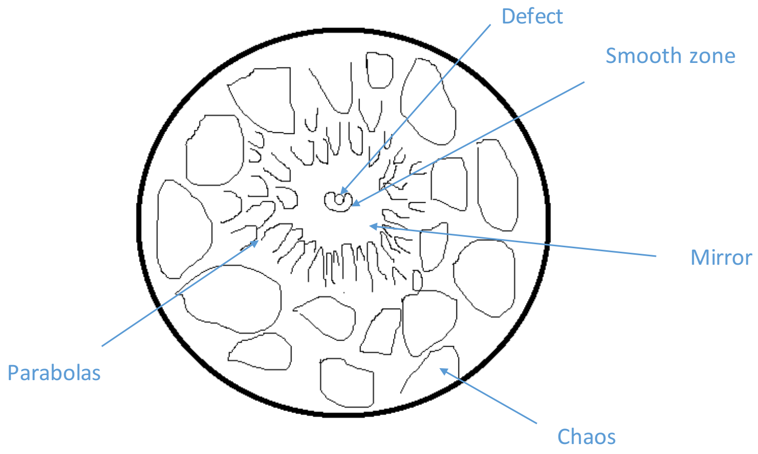

Figure 4.17: Schematic representation of the fracture surface of a dog-bone specimen, with the identification of the different areas.

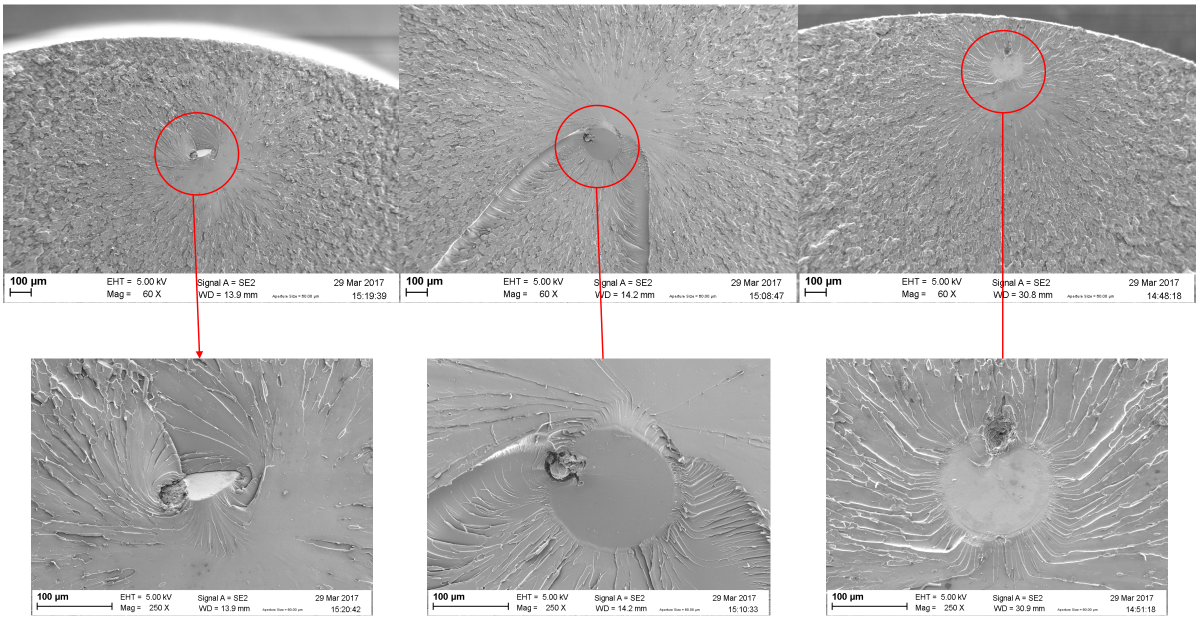

Figure 4.18: Fracture surfaces of the specimens broken under quasi static loading with a zoom on the initiation of the fracture. From left to right: sample 1 static, sample 2 static and sample 3 static.

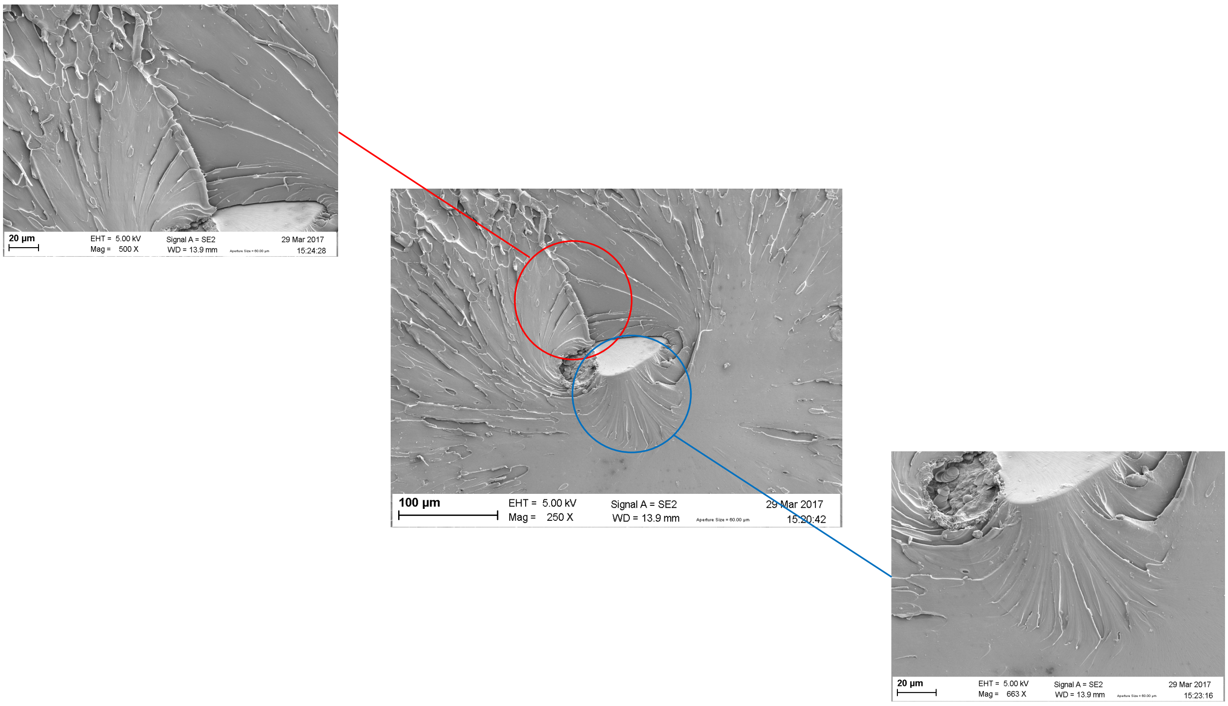

Figure 4.19: Closer view of the initiation area of the sample 1 static. On the top left corner: a scarp. On the bottom right corner: the riverlines between the smooth zone and the mirror zone.

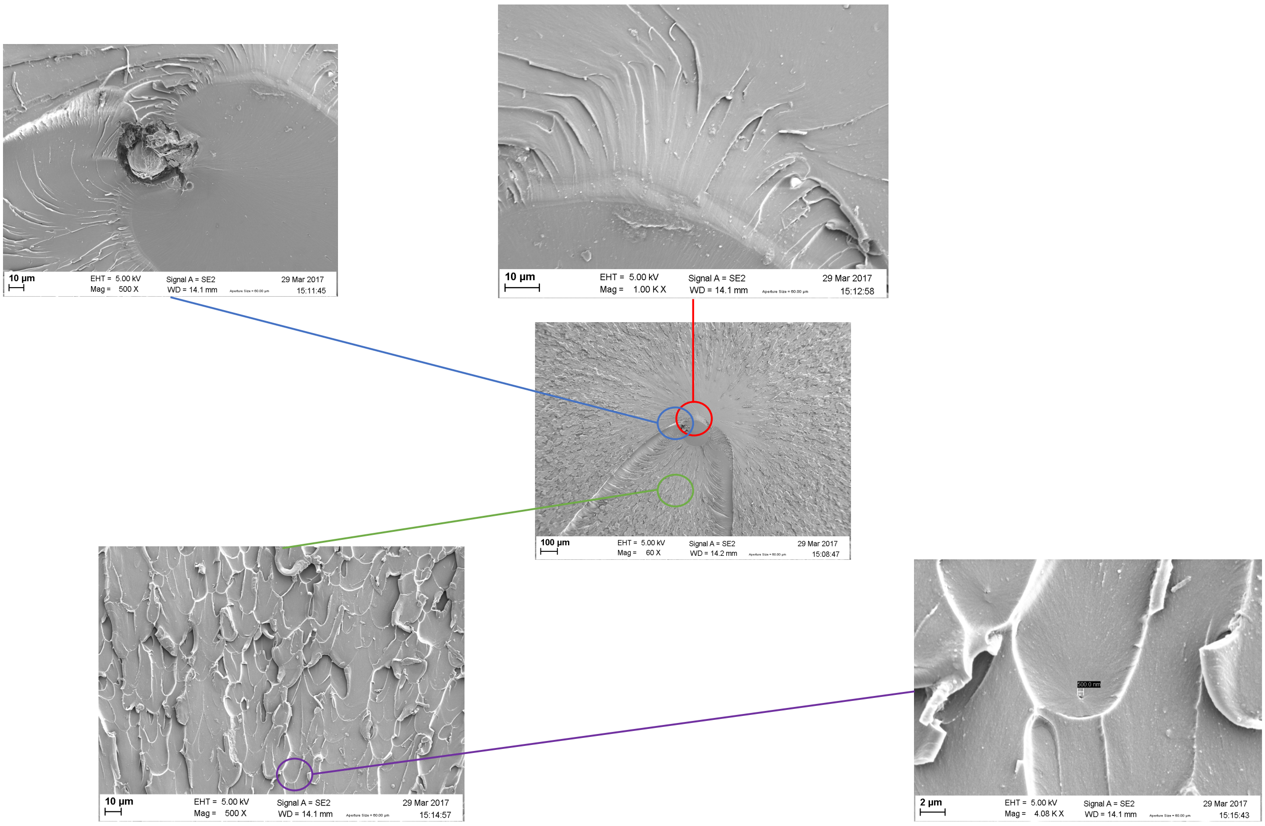

Figure 4.20: Identification of the different zones around the initiation of failure of sample 2 static. On the top left corner is a zoom of the defect. On the top a zoom of the lines between the smooth zone and the mirror zone. On the bottom left is the parabolas zone and on the bottom right corner is a zoom of a parabola.

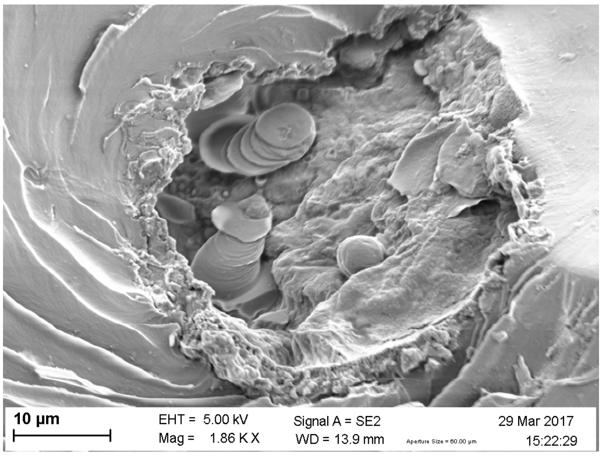

Figure 4.21: Closer view of the defect of the sample 1 static.

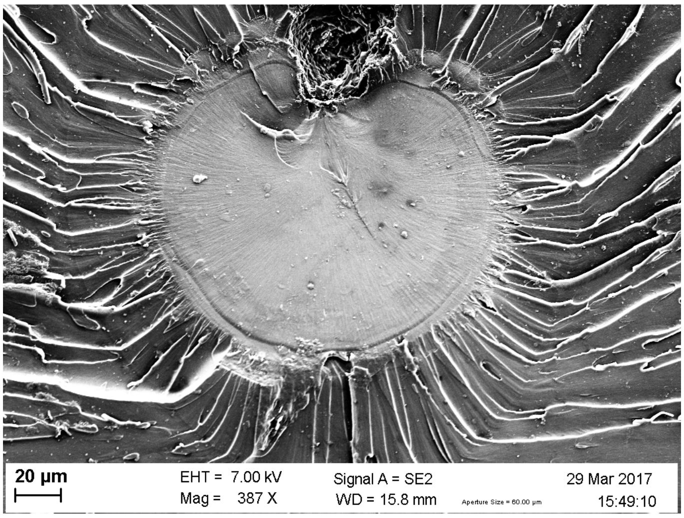

Figure 4.22: Closer view of the smooth area of the sample 3 static.

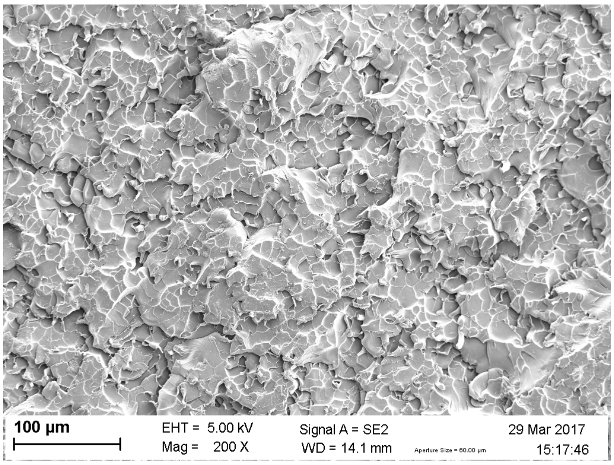

Figure 4.23: Chaos area, away from the initiation where the surface is rough.

Dog-bone specimens under cycling loading

Similar areas are observed on the fracture surfaces of the samples that failed under cycling loadings. The figures 4.24 and 4.25 respectively shows the fracture surfaces of the samples broken under cycling loading at 60% and at 50% of the stress at failure. The main difference is the size of the mirror zone, which increases a lot on the fatigue samples. A summary of the sizes of the several zones for each samples is listed on table 4.10. This table shows the equivalent radius of the almost circular defects, the width, the length and the type of the smooth zone and the mirror zone size. The measurements for the smooth zone are always taking the maximum length and maximum width of the zone, while the measurements for the mirror zone represent the distance between the edge of the defect and the furthest transition locus between the mirror zone and the first parabolas. The rough region of the fatigue specimens is very similar to the static specimens and is shown on figure 4.26. Figure 4.27 shows the different areas observed on the sample 4 fatigue. The zone 1 is the initiation area, with the defect and the smooth zone. The zone 2 shows the end of the mirror zone and the beginning of the parabolas. The zone 3 shows the starts of the chaotic area. A secondary defect, much smaller than the one responsible of the failure (with a radius around 3 μm) , is shown on figure 4.28. Again, a parabola is observed around it. The samples 7 and 8, which were broken under static loading after undergoing cycling loading at 40% of the stress at failure show a fracture surface similar to the samples broken without cycling loadings, as seen on figure 4.29.

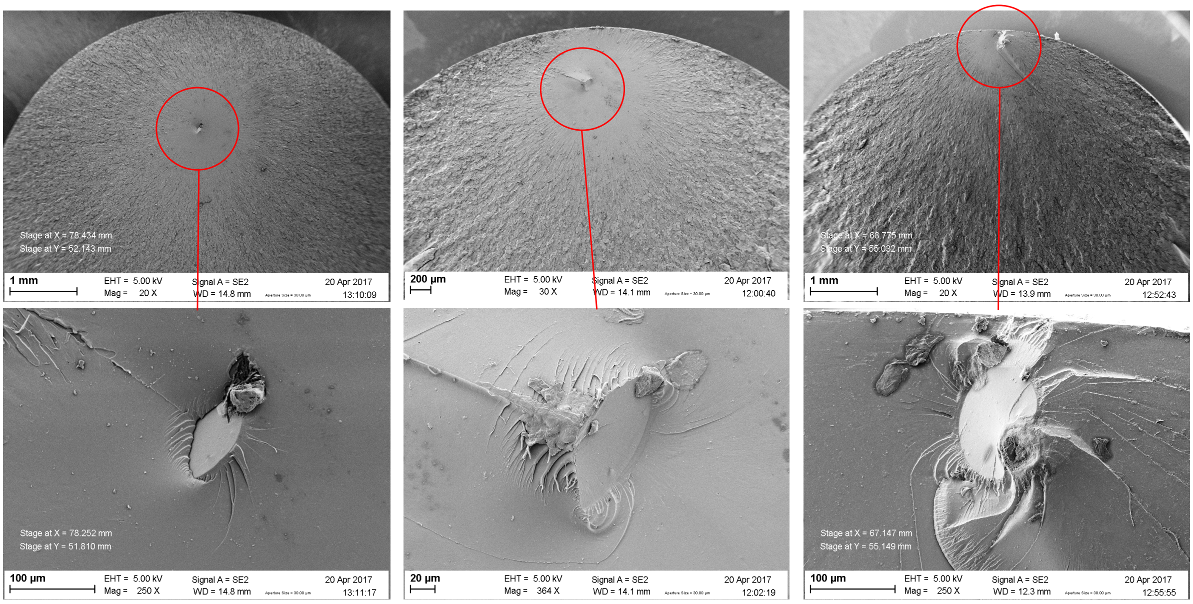

Figure 4.24: Fracture surfaces of the specimens broken under cycling loading at 60% of the stress at failure with a zoom on the initiation of the fracture. From left to right: sample 1 fatigue, sample 2 fatigue and sample 3 fatigue.

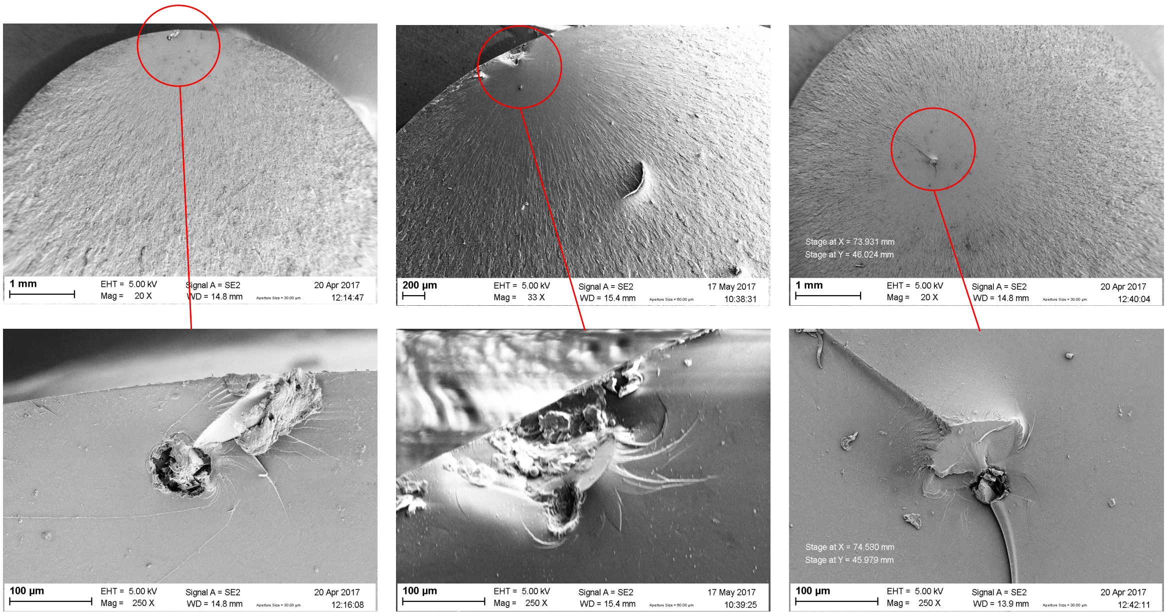

Figure 4.25: Fracture surfaces of the specimens broken under cycling loading at 50 % of the stress at failure with a zoom on the initiation of the fracture. From left to right: sample 4 fatigue, sample 5 fatigue and sample 6 fatigue.

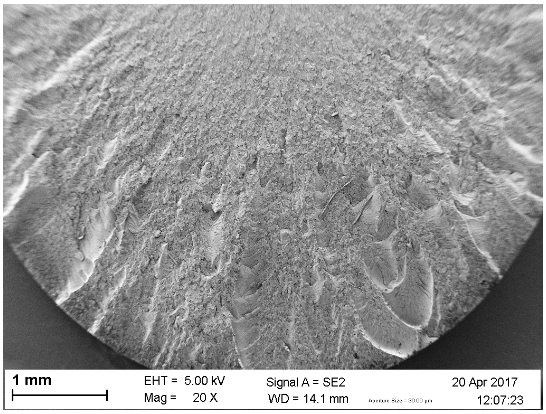

Figure 4.26: Very rough area, away from the defect, of the sample 2 fatigue.

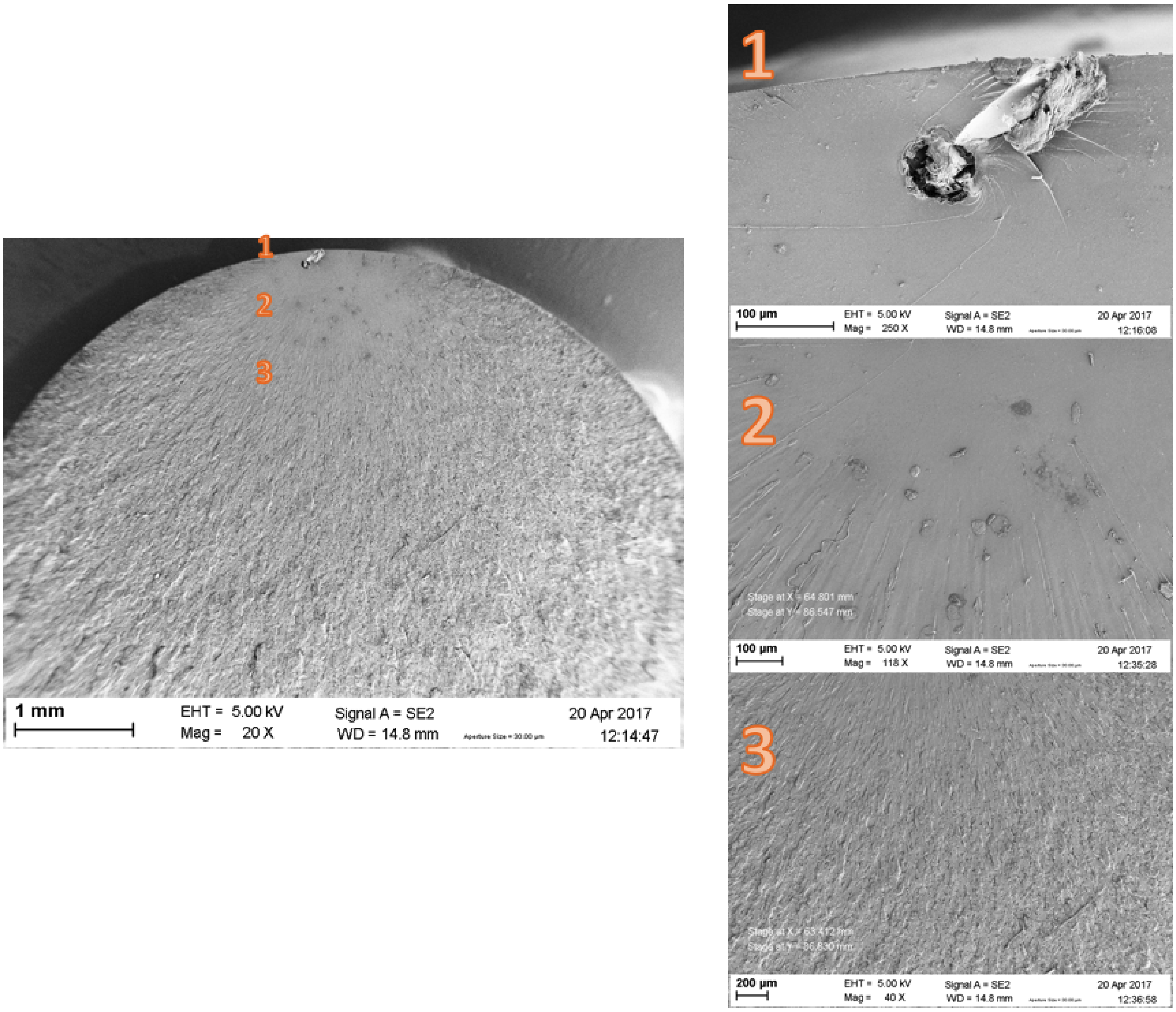

Figure 4.27: Identification of the different areas of the fracture surface of the sample 4 fatigue. 1: the initiation area with the defect and the smooth zone. 2: the mirror zone. 3: the parabolas area.

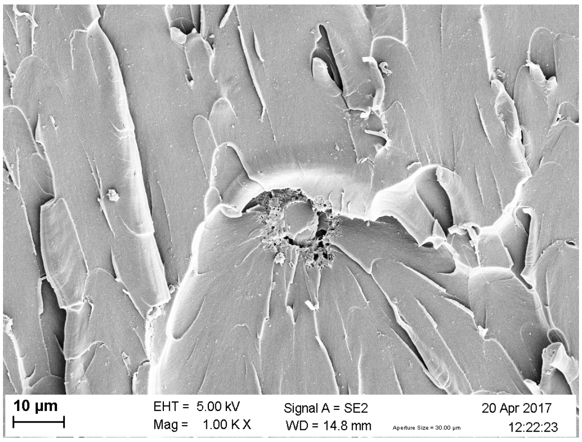

Figure 4.28: Secondary defect of the sample 4 fatigue.

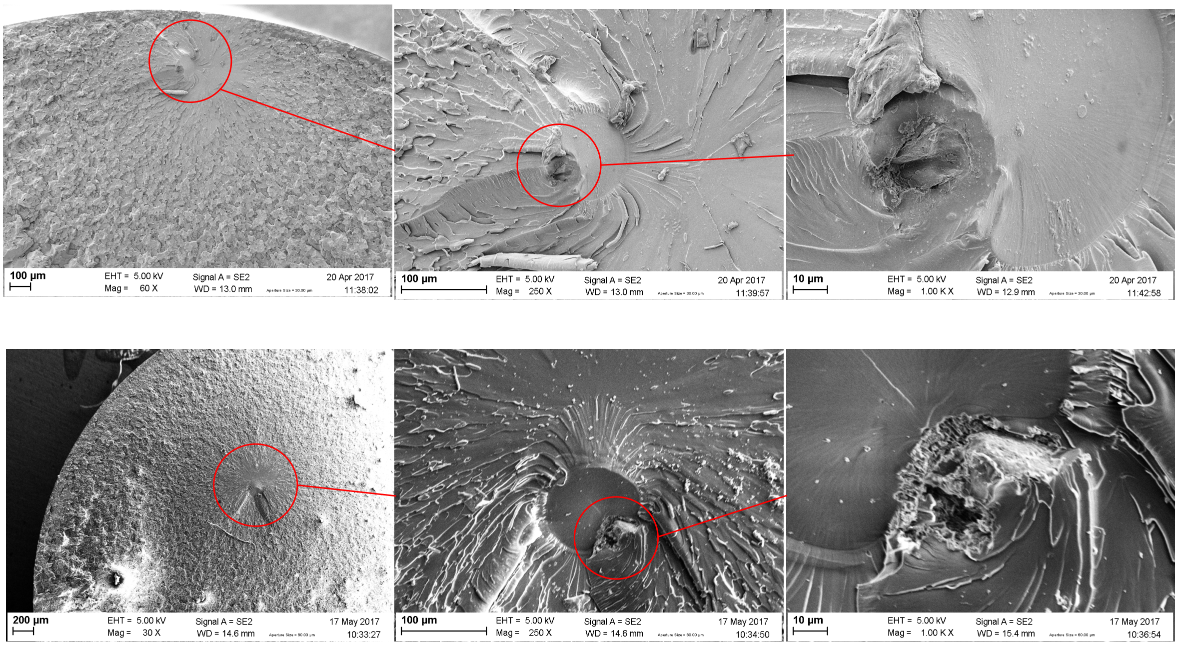

Figure 4.29: Fracture surfaces of the specimens broken under quasi static loading after cycling loading at 40 % of the stress at failure with zooms on the initiation of the fracture. On top: sample 7 fatigue. On the bottom: sample 8 fatigue.

	Defect eq. radius [μm]	Smooth zone size and type [μm]	Mirror zone size [μm]
Sample 1 static	17.6	36x73 A	90
Sample 2 static	20.69	159x170 B	209
Sample 3 static	18.8	120x142 B	218
Sample 1 fatigue	22.69	58x88 A	679
Sample 2 fatigue	25.39	49x104 A	713
Sample 3 fatigue	22.6	88x123 B	505
Sample 4 fatigue	31.59	40x123 A	832
Sample 5 fatigue	25.53	20x60 A	844
Sample 6 fatigue	20.74	60x112 A	1000
Sample 7 fatigue	17.9	76x105 B	159
Sample 8 fatigue	15.8	97x108 B	184

Table 4.10: Summary of the sizes of the different zones fore each sample: the equivalent radius of the defect, the width, length and type of the smooth zone and the mirror zone.

CT specimen under static loading

Only the thin CT specimen are presented. Figure 4.30 shows the fracture surface of the CT sample 3. It shows the initiation of the failure and the riverlines next to it. There is also a mirror zone around the area of initiation of failure.

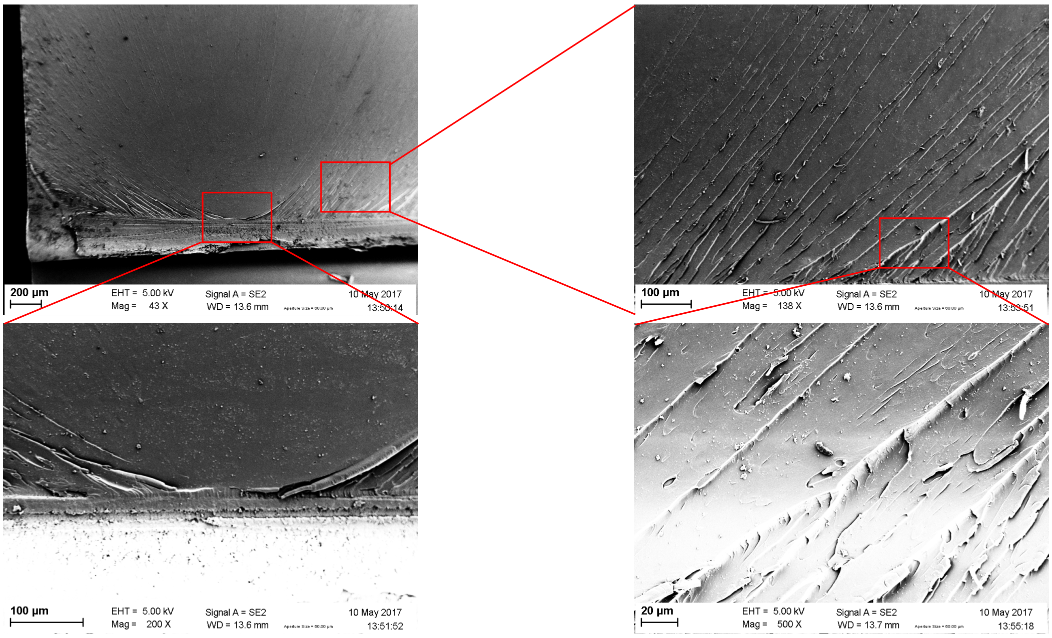

Figure 4.30: Identification of the failure initiation of the sample 3, and a closer view (on the left) of the river lines.

CT specimen under cycling loading

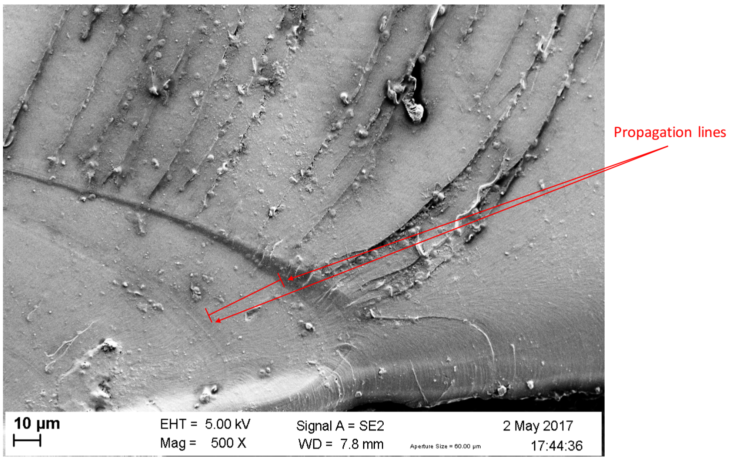

Figure 4.31: Propagation lines of the fatigue testing.

Figure 4.31 shows the propagation lines of the crack. It appears that one cycle increase the size of the crack of around 30 μm. The fracture surface of the sample 17 is presented on figure 4.32. The stop lines between the propagations of the crack are shown as well as the initiation of the failure. The fracture surface of the sample 18 is presented on figure 4.33. The initiation of failure is shown, with a stop lines between a smooth area and riverlines. On the right of the figure, a smooth area is highlighted and the presence of parabolas is again observed. The initiation of failure is more highlighted on figure 4.34. Riverlines are clearly seen, as well as some smoother areas. The transition between those regions is well represented on figure 4.35. Figure 4.36 shows a closer view of a stop between two smooth areas. It appears that on both specimens 17 and 18, there are several areas of propagation, separated with stop lines. A similar fracture surface is observed on figure 4.37 for the sample 22, which ended up broken under static loading after undergoing cycling loading. Several areas of propagation are observed and it is important to notice that the propagation didn't reach the left corner of the sample, as seen on the top left picture of figure 4.35.

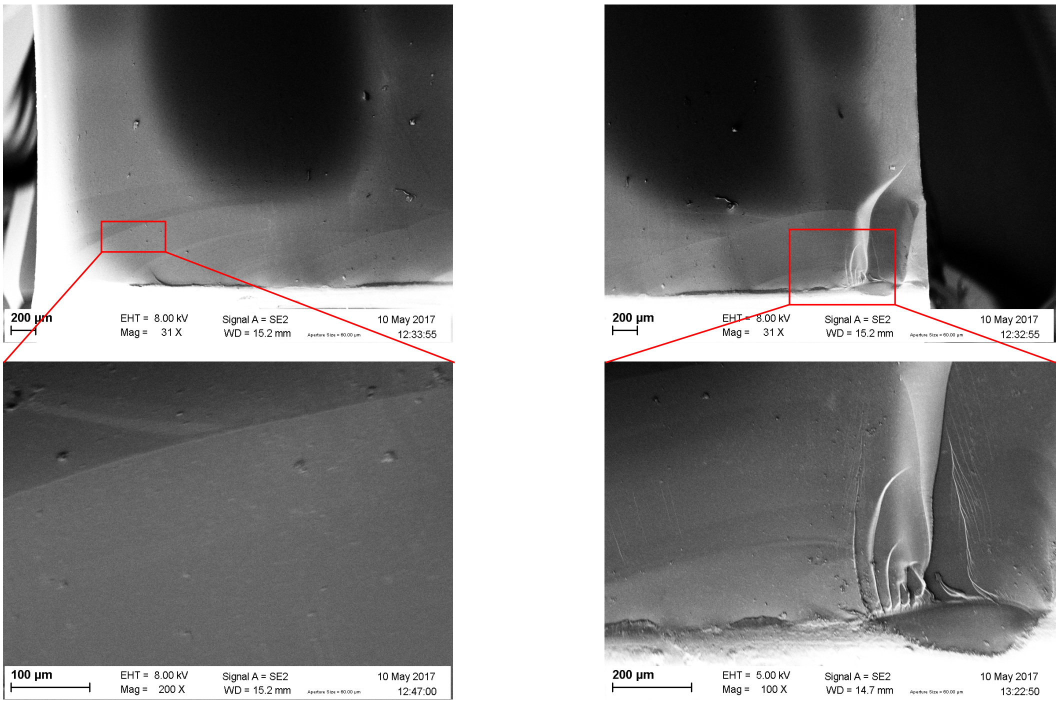

Figure 4.32: Fracture surface of the sample 17. On the left: Stop lines of the fatigue testing. On the right: Initiation area of the failure.

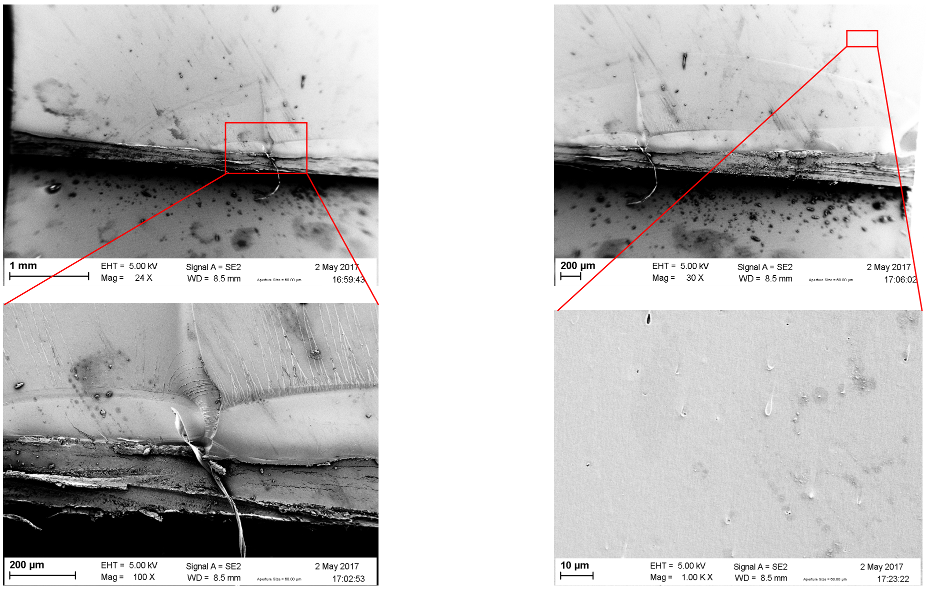

Figure 4.33: Fracture surface of sample 18. On the left: Initiation area of the failure. On the right: Smooth area with the presence of several parabolas.

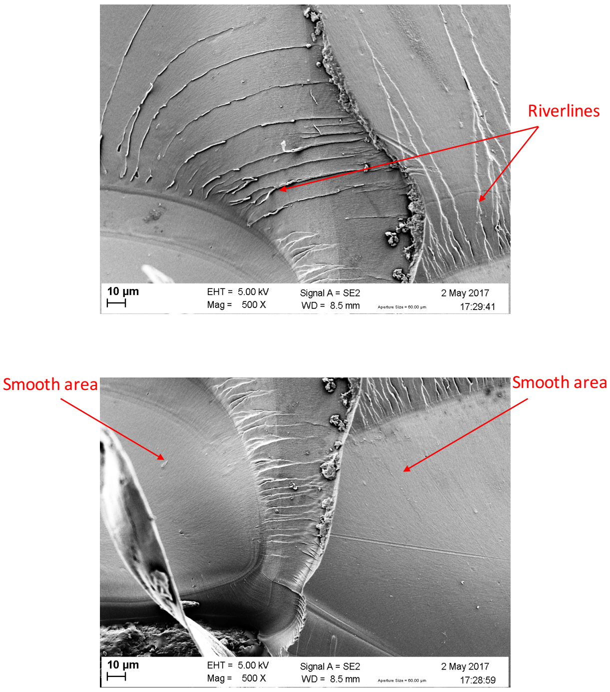

Figure 4.34: Zoom of the initiation of the fracture of sample 18. On top: riverlines. On the bottom: riverlines between 2 smooth areas.

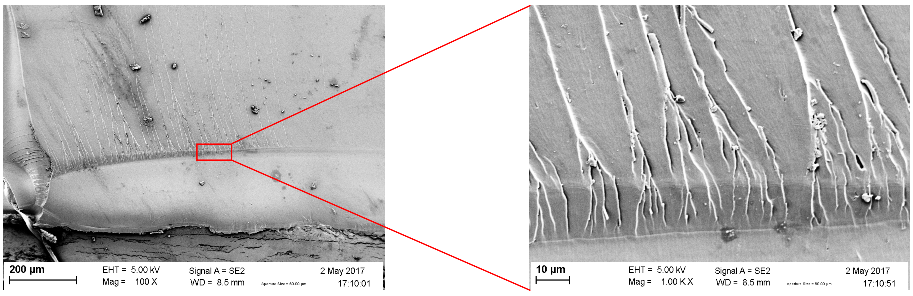

Figure 4.35: Zoom of the line between the the smooth area and the riverlines area of the sample 18.

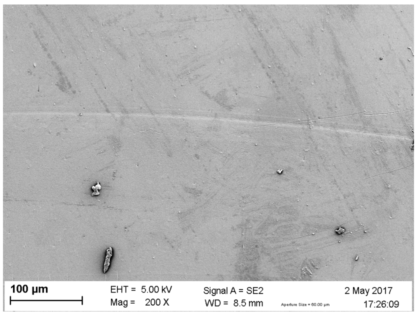

Figure 4.36: Stop line in between two smooth areas of the sample 18.

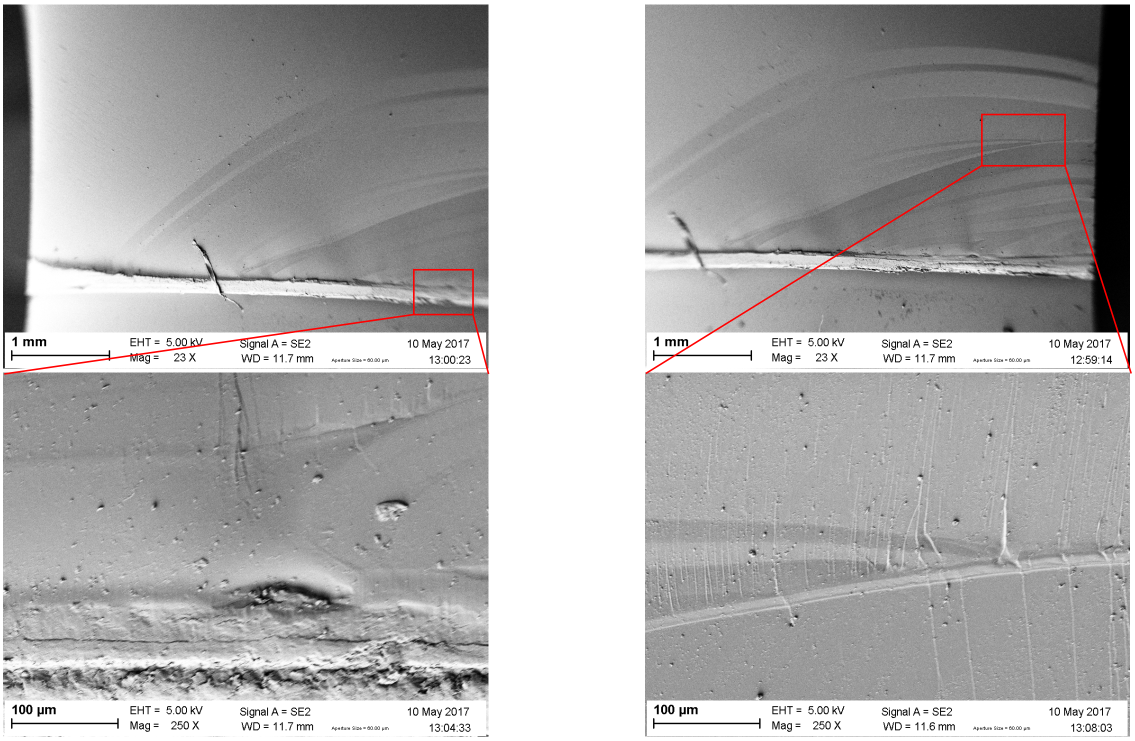

Figure 4.37: Fracture surface of the sample 22. On the left: the initiation of the crack. On the right: the stop lines of the propagation of the crack.

Chapter 5

Discussion

This chapter discusses all the results from the previous chapter and connects the results of the mechanical tests, the finite elements simulations and the fractography. It starts with the analyze of the pre-cracking method and its impact on the results. It also approximates a fracture toughness of the dog-bone samples to validate its value for the RTM6. FEA is used to validate the fracture toughness of the CT samples and to calculate the stress state at the crack tip. Then it presents the stress-life curve of the RTM6 and compares it with other stress-life curves of polymers. It also describes the crack propagation rate as a function of the amplitude of the stress intensity factor and compares this curve with the fracture surfaces of the samples. Furthermore the features observed thanks to the SEM are explained to propose a mechanism of propagation of the crack until final failure.

5.1 Pre-cracking

The pre-cracking was an important step of the experiments. The was done manually, and therefore a lot of factors could affect it. Each sample had different size and shape of pre-crack. The length, the width and the angle of sharpness (see figure 5.1) of each pre-crack was measured and table 5.1 lists all the values.

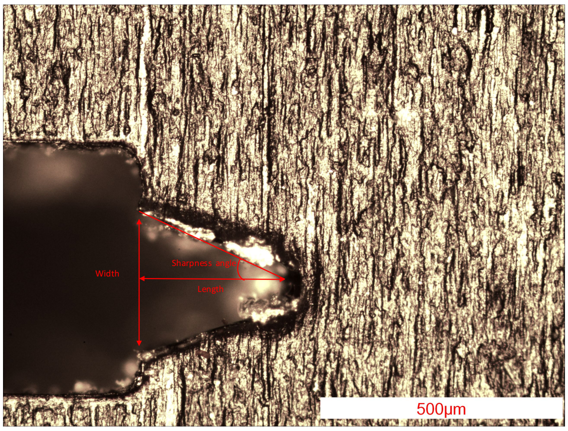

Figure 5.1: Optical microscope picture of pre-cracks.On the left, the pre-crack of the side B of the sample 3, with a zoom x20. On the right the pre-crack of the side A of the sample 5 with a zoom x10.

	Side A			Side B		
	Length [μm]	Width [μm]	Angle [°]	Length [μm]	Width [μm]	Angle [°]
Sample 1	150	100	18	100	80	21
Sample 2	300	50	4.8	220	38	4.9
Sample 3	50	20	11	28	9	9.1
Sample 4	361	200	15.5	380	170	13
Sample 5	347	240	19	324	210	18
Sample 6	412	230	15.6	230	169	14
Sample 17	347	250	19	267	180	18.6
Sample 18	307	189	17	311	203	18
Sample 22	345	163	13	251	134	15

Table 5.1: Measures if the pre-cracks length, width and angle of sharpness.

It is important to remember that sample 17 and 18 broke under cyclic loading and therefore the crack propagated, and that sample 22 was broken under static loading after undergoing cyclic loading. Therefore the shape and the length of its pre-crack changed. On this table, it is easy to see that the samples 1, 2 and 3 had pre-cracks smaller than the others. Sample 3 had particularly a small crack, as shown on figure 5.2 which explains the very high load at failure. Sample 2 has a very sharp pre-crack. This kind of pre-crack is the most similar to a fatigue pre-crack, as the sample 22 had after the testing in the fatigue machine. Both samples 2 and 22 had similar results, with a low load at failure, and then a decreasing load before final fracture. All of this analysis confirms that the pre-crack has an influence of the propagation of the crack. First a minimal crack length is necessary in order to propagate, but the shape is also important. A sharper pre-crack result in a more brittle material, therefore to have a good sample, the pre-crack should be very long and sharp.

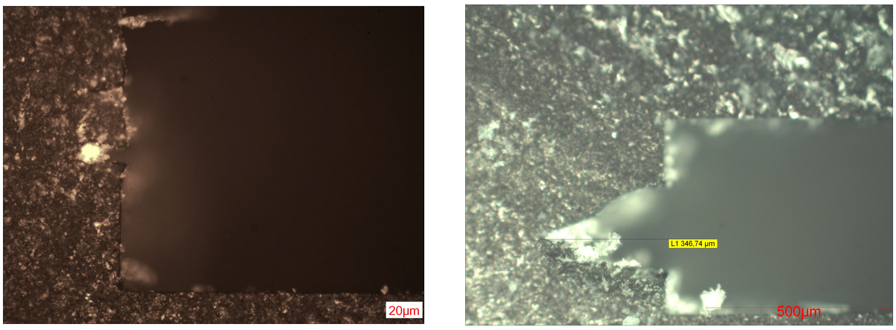

Figure 5.2: Optical microscope picture of pre-cracks.On the left, the pre-crack of the side B of the sample 3, with a zoom x20. On the right the pre-crack of the side A of the sample 5 with a zoom x10.

5.2 Static

It has been studied that the fracture of RTM6 is initiated when a critical principal stress is attained locally near characteristic internal defects of the material [15]. The defect acts as a stress concentrator leading to local tensile conditions. In the CT specimen, pre-cracks are introduced as worst defects. An approximation of the fracture toughness of the dog-bone samples was determined thanks to [39].

$$K_{Ic} = \sigma_c \sqrt{\pi a} \tag{5.1}$$

σ_c was the stress at failure and a is the equivalent radius of the defect observed with the SEM. The fracture toughness of the samples are listed on 5.2. This is an approximation, as the defects are not exactly circular, but the fracture toughness is not that far from the one obtained experimentally on the CT specimens.

	Stress at failure [MPa]	Defect radius [μm]	Fracture toughness [MPa $\sqrt{m}$]
Sample 1	99.82	17.6	0.742
Sample 2	81.88	20.69	0.661
Sample 3	94.89	18.8	0.729
Average	92.2	19.03	0.711

Table 5.2: Determination of fracture toughness from the tensile testing under quasi static loading of dog-bone samples

5.2.1 FE

The FE simulations performed gave different fracture toughness when the length of the pre-crack was too small, but for more than 200 μm, the fracture toughness was always the same regardless of the pre-crack length. This may be caused by numerical issues but it may also confirms the existence of a minimal value of the pre-crack. A pre-crack, very close to the real value, of 400 μm was used in the final simulations and the results of the simulations, fracture toughness and opening at the crack mouth, compared to the mechanical tests are listed on table 5.3. The difference in the clip-on opening of the tests and of the simulations probably lies in the fact that in the simulations they are calculated on the external node, whereas for the tests, the clip-on was inserted between the extensometer plates which have a certain height.

	Load [N]	K_{Ic} [MPa$\sqrt{m}$]	Fracture energy [$\frac{J}{m^2}$]	Clip-on [mm]
FE Thin CT	166.87	0.91	247.77	0.11
Experiment Thin CT	166.87	0.78	184	0.14
FE Thick CT	202.6	0.94	264.37	0.22
Experiment Thick CT	202.6	0.946	267.76	0.3

Table 5.3: Comparison of the FE simulations and the experiments of the CT specimens.

The simulations with plasticity showed that a maximum principal stress of 243 MPa is reached at the crack tip when failure occurs. This is lower than the 300 MPa calculated by Chevalier et al. [15] as a failure criterion. This means that even at a crack tip, the existence of a defect, for example, is needed to reach the 300 MPa required for failure to occur.

The same simulation was performed with a blunt crack, which model is shown on figure 5.3. A stress state at the crack tip of 114 MPa was calculated and shown on figure 5.4, which is even lower than the one with a triangle sharp crack.

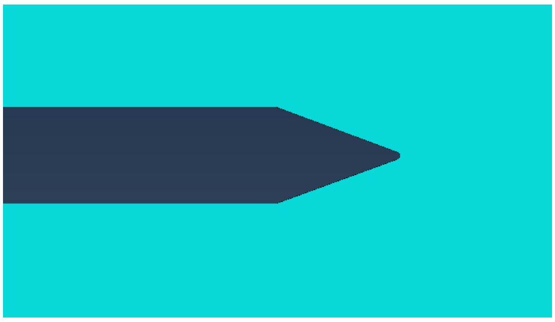

Figure 5.3: Model of a blunt crack in Abaqus.

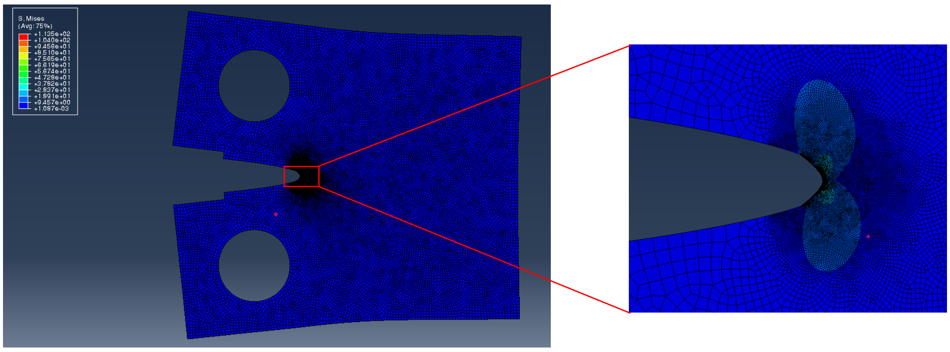

Figure 5.4: FEA of a triangle blunt crack showing the maximum principal stress at the crack tip.

5.3 Fatigue

Some components, especially aircrafts, are subjected to repeated loads, and those stresses can lead to microscopic physical damage to the materials involved. This microscopic damage can accumulate until a crack initiates and leads to the failure of the component, even at stresses well below a given material's ultimate strength. Dowling [40] defines this process of damage and failure due to cyclic loading as fatigue. This term is used because cyclic stresses gradually change the ability of the material to resist stress, but it is not readily observable. A typical cycle loading is shown on figure 5.5. On a cycle, a maximum and a minimum stress are presents. Averaging them gives the mean stress, σ_m and R is called the stress ratio and is defined as:

$$R = \frac{\sigma_{min}}{\sigma_{max}}$$

A stress ratio of 0.1 was always used in the fatigue tests to assure tensile-tensile loading.

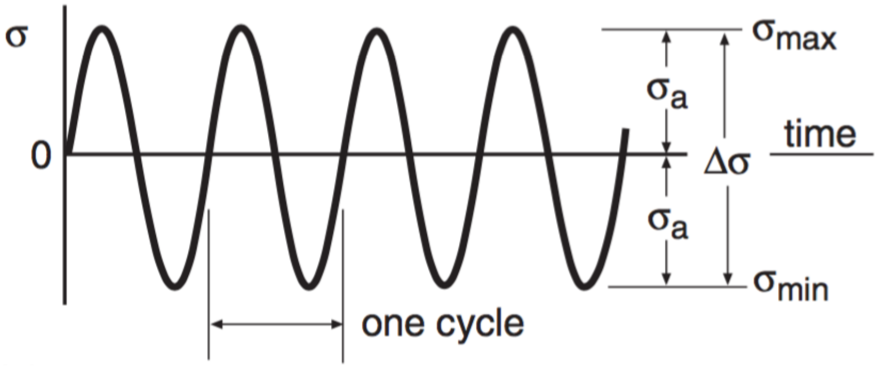

Figure 5.5: Typical drawing of a cycle loading including the associated nomenclature [40].

5.3.1 Tensile testing

Wohler curve

A fatigue crack or other damage will develop if a material is subjected to a sufficiently severe cyclic stress, leading to complete failure of the member. If the test is repeated at a higher stress level, the number of cycles to failure will be smaller [40]. The results of such tests with different stress levels may be plotted to obtain a stress–life curve (S-N curve), also called a Wohler curve. When the data approximate a straight line on a log–linear plot, the following equation is used as a mathematical representation of the curve:

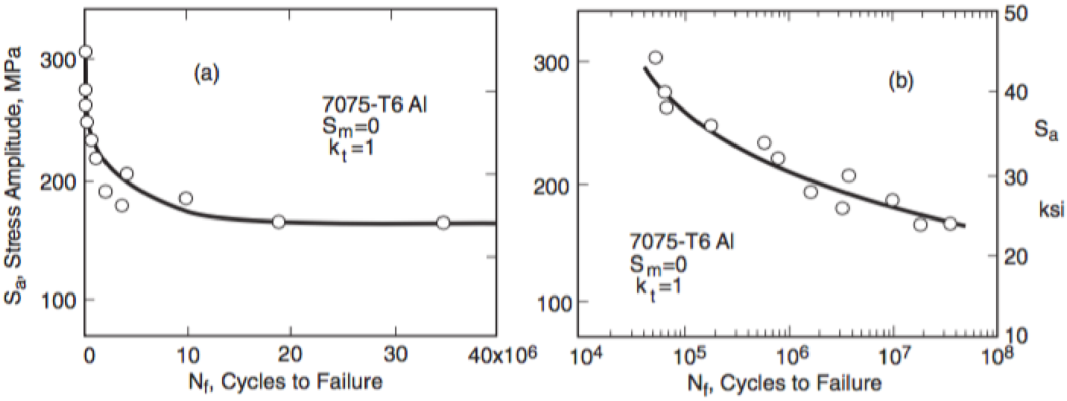

Figure 5.6: Stress versus life (S-N) curves from rotating bending tests of unnotched specimens of an aluminum alloy. Identical linear stress scales are used, but the cycle numbers are plotted on a linear scale on the left, and on a logarithmic one on the right [40]. Data from [41].

$$\sigma_a = C + DlogN_f$$

where C and D are fitting constants. When the data approximate a straight line on a log–log plot, the fitting equation is

$$\sigma_a = AN_f^B$$

where A and B are fitting constants. The figure 5.7 shows the stress-life curve of RTM6. The dashed line is a power law approximation of the data, with the equation:

$$\sigma_{max} = 81.407 N_f^{-0.064} \tag{5.2}$$

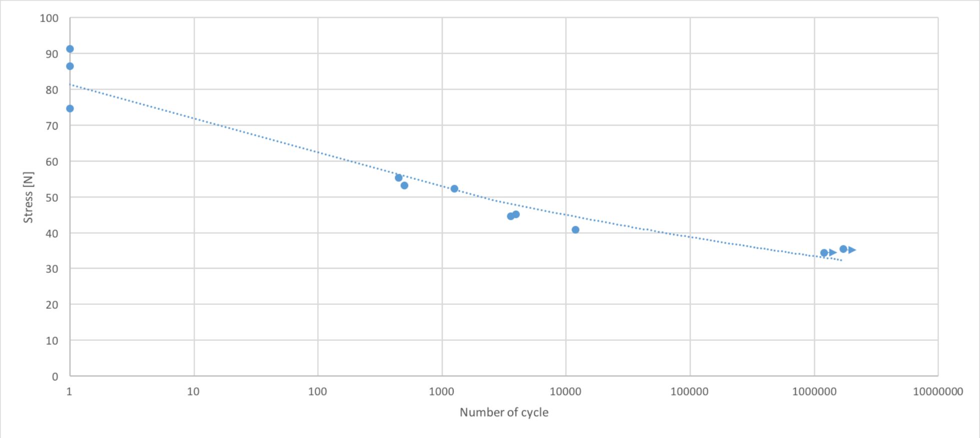

Figure 5.7: Stress at fracture - Number of cycles curve of the dog-bone samples. The dashed line is an approximated curve of the data.

The stress intensity factor of the samples 7 and 8 were calculated with equation 5.1. The values are listed on table 5.4. They are below the estimated value of ΔK_{th} of 0.28 MPa$\sqrt{m}$ obtained from the FCP testing of the CT samples, which gives a $K_{th} = 0.31$ MPa$\sqrt{m}$. It is thus understandable that under such stress the samples were not deteriorated. This is consistent with the residual strength testing which almost didn't show any deterioration of the samples.

	Stress applied [MPa]	Defect radius [μm]	Stress intensity factor [MPa $\sqrt{m}$]
Sample 7	34.3	17.9	0.257
Sample 8	35.46	15.8	0.25

Table 5.4: Determination of fracture toughness from the tensile testing under cyclic loadings of 40% of the stress at failure of dog-bone samples

Endurance limit

According to figure 5.7 and the assumption that the samples 7 and 8 were not deteriorated at all, the endurance limit σ_e should lie between 35 and 40 MPa. For a radius of defect of 21 μm and $\Delta K_{th} = 0.28$ MPa$\sqrt{m}$ equation 5.1 gives $\sigma = 38.3 MPa$. If the same mechanism of damage occurs at the crack tip of the CT samples and at the edge of the defect of the unnotched dog-bone samples, it can therefore be approximated that $\sigma_e = 38.3$.

Comparison with other epoxy resins

This curve can be compared to other S-N curves from the literature. Figure 5.8 shows on the left the S-N curve of a standard diglycidyl ether of bis-phenol A. Its σ_{uts} is 73.3 and

$E = 2.62GPa$ [42]. This epoxy has a σ_{uts} 15MPa smaller than RTM6 and its fatigue life curve is similar to the RTM6, with a downward shift of about 15 MPa. On the right the epoxy is also a diglycidyl ether of bis-phenol A. The results are similar to RTM6 until 10000 cycles, but the curve keeps decreasing until a maximum stress of 25 MPa, while the endurance limit of RTM6 seem to be around 38 MPa. Figure 5.9 shows on the left an EPIKOTETM Resin MGS RIMR 135 and EPIKURETM Curing Agent MGS RIMH 137 with a $\sigma_{uts} = 70$ MPa [44]. Once more, the curve is similar to RTM6, with a shift of about 20 MPa. On the right of the figure, an Epon 826 Resin and Epi-Cure Curing Agent 9551 fatigue curve is represented. It is very similar to RTM6. It is important to notice that it is the equivalent stress amplitude that is represented on this graph instead of the maximal stress. The equivalent stress amplitude defined by Tao et al. is $(1 + 0.76\frac{\sigma_m}{\sigma_a})\sigma_a$ ends up being very close to the maximal stress with the testing conditions of this work and therefore is suitable for a qualitative comparison.

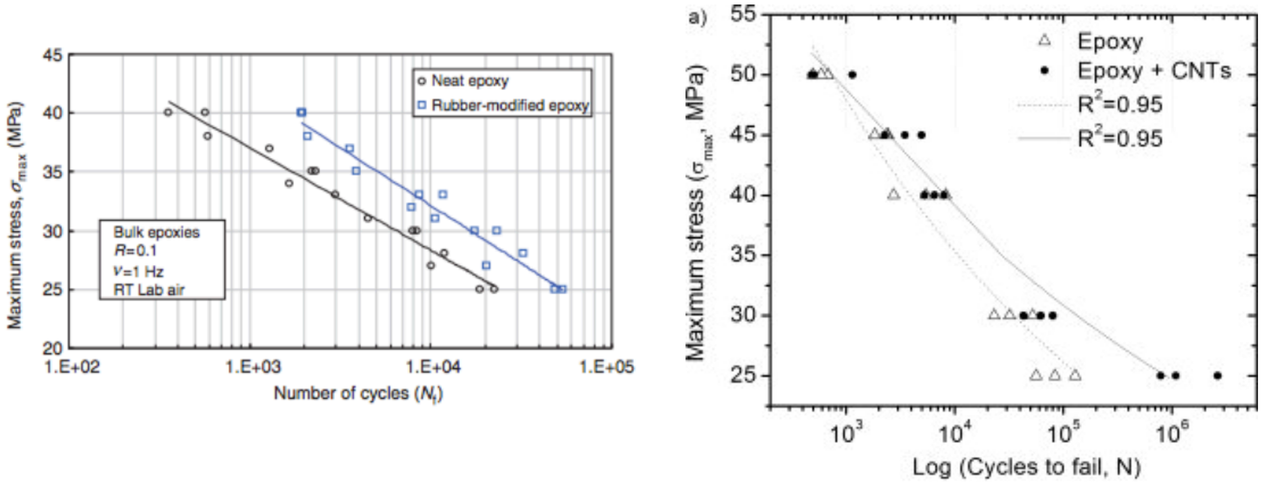

Figure 5.8: Stress versus life (S-N) curves of epoxy resins. On the left a diglycidyl ether of bis-phenol A[42]. On the right a diglycidyl ether of bis-phenol A [43].

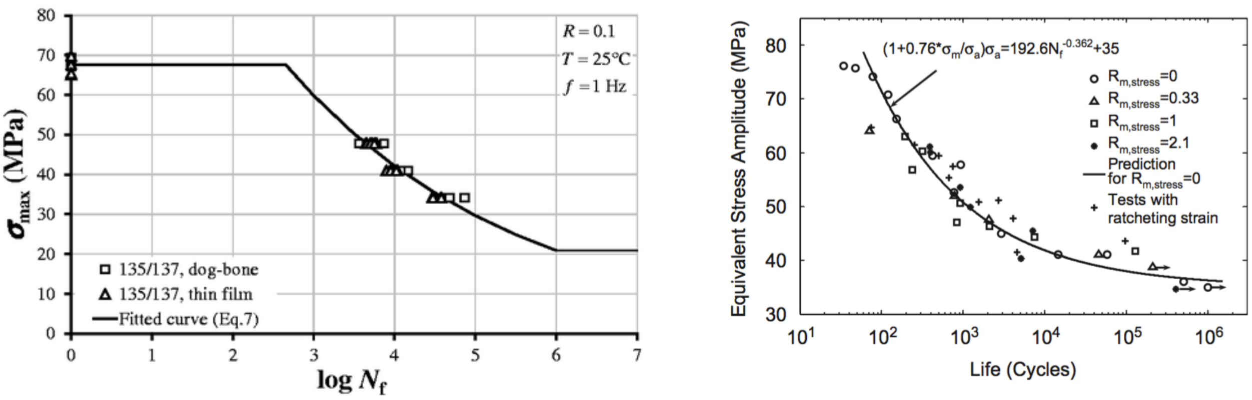

Figure 5.9: Stress versus life (S-N) curves of epoxy resins. On the left an EPIKOTETM Resin MGS RIMR 135 [44]. On the right an Epon 826 Resin [45].

Murakami's equation for ΔK_{th}

Murakami et al. [46] derived this formula for high strength steels:

$$\Delta K_{th} = 0.5 \Delta\sigma \sqrt{\pi \sqrt{area}} \tag{5.3}$$

This formula shows surprisingly accurate results on RTM6 when *area* is used as the area of the defect initiating the failure, as seen on table 5.5. As the failure of sample 5 was close to the surface, the factor 0.5 was changed to 0.65, according to Murakami et al. [46]. This approach finds a ΔK_{th} of about 0.28, which is very close to the values found with the FCP testing.

	Stress applied [MPa]	Defect area [μm^2]	ΔK_{th} [MPa $\sqrt{m}$]
Sample 1	55.26	1617.4	0.2795
Sample 2	53.19	2025	0.2846
Sample 3	52.31	1599	0.264
Sample 4	44.63	3135.7	0.27
Sample 5	40.82	2046.97	0.2847
Sample 6	45.08	1351.5	0.218

Table 5.5: Determination of the amplitude of the stress intensity factor threshold from the tensile testing under cyclic loadings of 50% and 60% of the stress at failure of dog-bone samples.

5.3.2 Short crack

The curves of figure 4.14a, 4.14b and 4.15 are very similar to figure 5.10. As explained by J. Everaerts [48] there is a possibility that cracks grow below ΔK_{th}. These short fatigue cracks are not based on the same assumptions as the long cracks and are described by EPFM rather than LEFM. They are short in a way that their size is smaller than the characteristic dimension of the micro-structure. They start growing at a high rate but do not propagate.

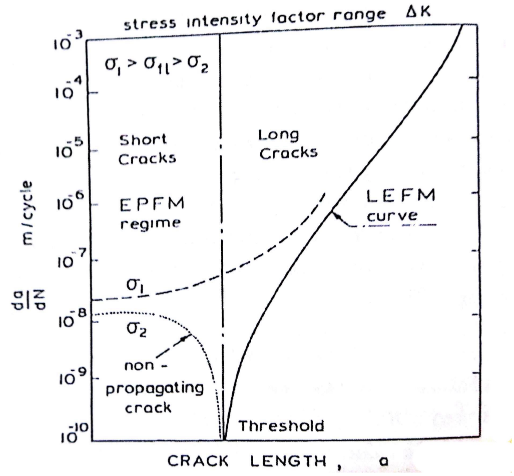

Figure 5.10: Possible crack growth rates of short cracks compared to long cracks [47].

The difference between short and long cracks is represented on figure 5.11, where there is an horizontal asymptote of value $\Delta\sigma_e$ for the short cracks whereas for long cracks ΔK_{th} is a constant. The transition between short cracks and long cracks has been identified by the El Haddad parameter [50]:

$$a_o = (\frac{\Delta K_{th}}{\Delta\sigma_e})^2 \frac{1}{\pi} \tag{5.4}$$

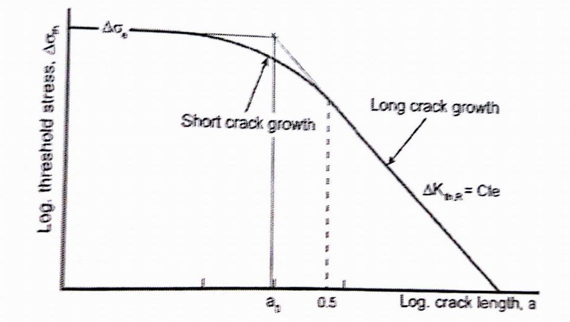

Figure 5.11: Schematic representation of the kitagawa-Takahashi diagram [49].

The work of J. Everaerts is based on metal alloys, where the short cracks stop growing when encountering a grain boundary. This is of course not the case for a thermoset polymer as the RTM6, but there is clearly an analogy of the mechanism. In the case of RTM6, non propagating short cracks grow until a plateau is reached. The material can then still undergo fatigue stress until the long cracks starts propagating faster and faster and the brittle final failure occurs. It is worth noticing that the El Haddad parameter of RTM6 is of about 19 μm, which is close to the size of the failure causing defects observed on the unnotched dog-bone specimens.

5.3.3 Fatigue crack propagation

Figures 5.12a, 5.12b and 5.12c are the curves of the "long cracks" only. They are similar to the curve on figure 5.12d obtained by Fischer et al. [51] and the important values are compared on table 5.6. The sample 22 didn't break under cycling loading and therefore the values at the end of the curve couldn't be measured. The threshold ΔK_{th} is very close to the one proposed by Fisher et al. but the Paris slopes and the critical $\Delta K_{critical}$ are a bit smaller.

	ΔK_{th} [MPa $\sqrt{m}$]	$\Delta K_{critical}$ [MPa $\sqrt{m}$]	Paris slope
Sample 18	0.32	0.4	11.43
Sample 17	0.27	0.39	13.25
Sample 22	0.34	/	/
Fischer neat RTM6 a	0.35	0.53	16.73
Fisher neat RTM6 b	0.35	0.51	17.72

Table 5.6: Comparison of the characteristic values obtained by FCP testing and the ones found in the literature.

Another epoxy resin, the Epotec YD 535 LV, was studied by [52]. They studied they effect of the stress ratio on the curve and found out that R=0.1 show significantly lower FCP rates

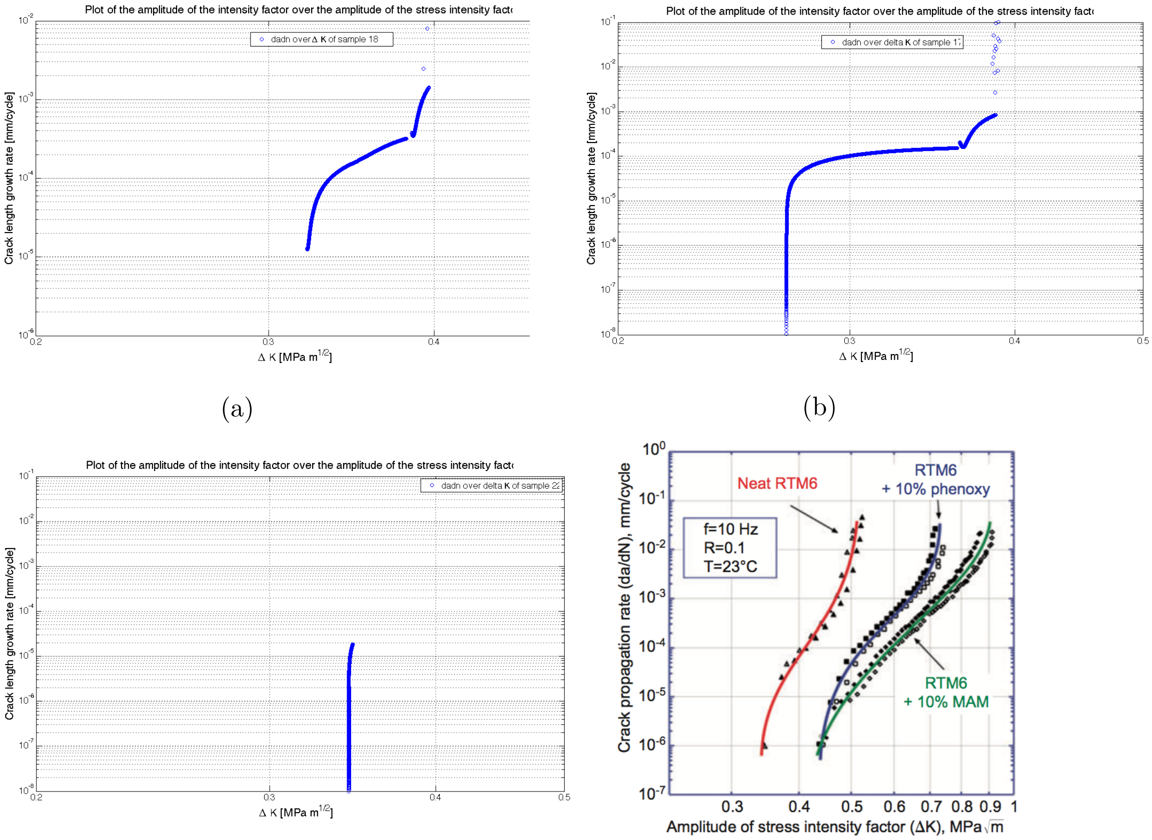

(a) (b)

(c) (d)

Figure 5.12: Plot of the crack propagation rate over the amplitude of the stress intensity factor for a) the sample 18, b) the sample 17, c) the sample 22. d) Crack propagation rate over the amplitude of stress intensity factor of neat RTM6 and toughened RTM6 [51].

R=0.4 or R=0.7 as seen on figure 5.13. They also found, for a stress ratio of 0.1 a $\Delta K_{th} = 0.3$ and a Paris slope of 10.91. Those results show that there is a close connection between the mechanisms of failure of the different resins.

Striations are visible to the naked eye on the fracture surface of the samples, as the schematic representation of figure 5.14 represents for the sample 22. The measurement of those areas are almost exactly consistent with the crack lengths obtained in section 4.3.2 as the machined notch and the pre-crack combined give $a = 4.7mm$. The first stop line at 2.5 + 4.7 = 7.2mm would represent the fatigue striations and the second at 2.7+4.7 = 7.4 mm the propagation of the crack under static loading. The third lines at 6.5 + 4.7 = 11.2 mm would represent the "unload" the decreasing part of the load - clip on curve.

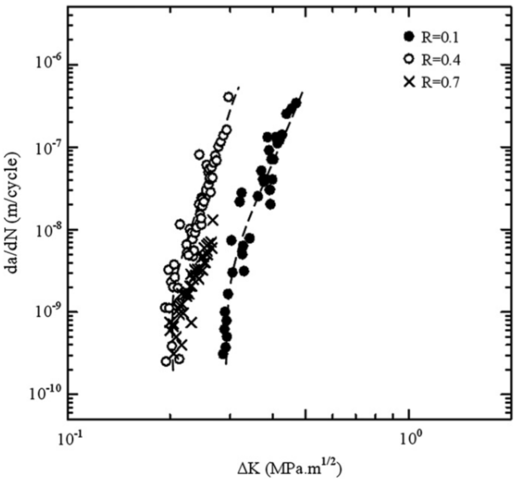

Figure 5.13: Crack propagation rate over the amplitude of the stress intensity factor for several stress ratios [52].

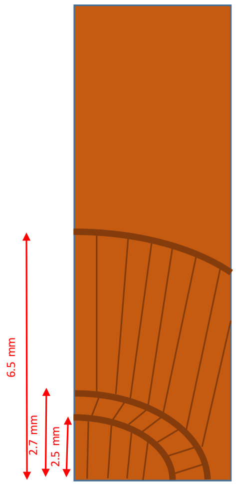

Figure 5.14: Schematic representation of the fracture surface of the thin CT specimen 22, showing the several propagations.

5.4 Comparison of fracture surface

5.4.1 Matrix cleavage

In brittle matrices, the energy of fracture is fairly low and there is relatively little deformation of the matrix during failure, this phenomenon is usually known as cleavage.

Parabolas

Parabolas are observed on figure 4.20 and similar result where studied by Greenhalgh [4], the parabolas observed in figure 5.15 appear when inhomogeneities lie ahead of, but in the same plane as, the main crack front. Secondary fracture initiate locally before the main crack reaches them, and thus the fracture direction can be locally inconsistent with the main crack growth direction. The parabola shape is explained by the propagation of the primary crack being faster than the secondary one. In the case of RTM6, the parabolas close to the main defect are facing the defect, but as the distance between the defect and the parabolas increases, the direction of the parabolas gets more and more random.

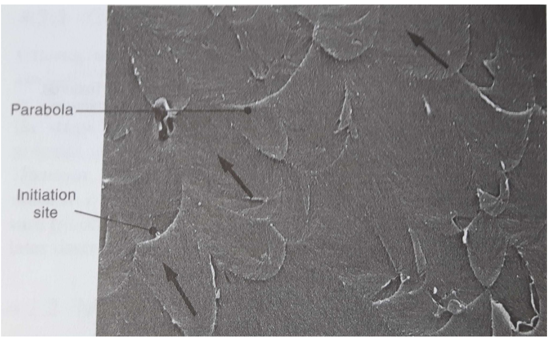

Figure 5.15: Example of parabolas in PMMA (x10k) [4].

Riverlines

Riverlines are a natural development of scarps and the convergence of crack planes. The riverlines converge into one crack and therefore the direction of crack growth is the direction in which the riverlines converge. Riverlines are therefore very useful to find crack growth direction [4].

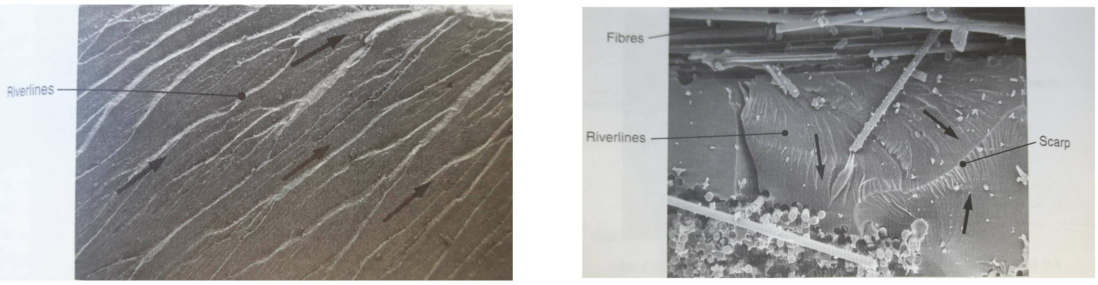

(a) (b)

Figure 5.16: Example of a) riverlines and b) riverlines and scarps [4].

Mirror, mist and hackle The mirror region is the smooth and featureless region. It is usually associated with slow propagation of the crack, and located around the origin of failure. As the fracture accelerates, a region called mist is produced, where the beginning of scarps and riverlines are observed. This region is rather smooth and matte. The crack accelerate to ultimately reach its final velocity, where the hackle fracture surface is observed.

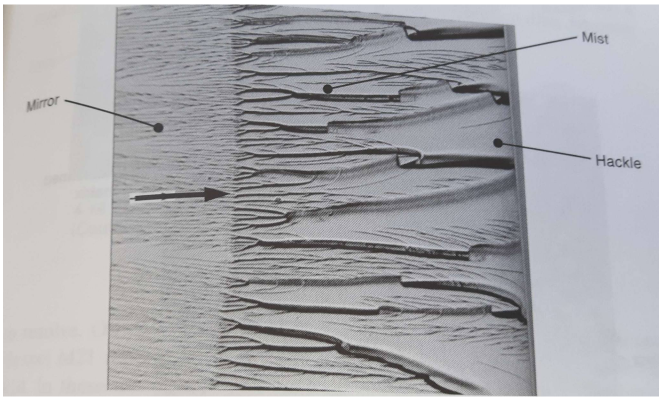

Figure 5.17: Example of mirror zone, mist and hackle [4].

5.4.2 Fatigue failure

As opposition to metals, where crack growth is associated with dislocation migration, a mechanism that can happen at low load levels [53], composites usually have amorphous polymer matrices which do not undergo this mechanism. However fatigue crack growth is still possible, especially in the presence of defects. Cyclic loading leads to changes in the material, such as stiffness drop, micro-crack or even plasticity at the crack tip (blunting). The presence of beachmarks is usually a good indication of fatigue fracture and they are associated with the period of the crack extension [53]. Striations are also a sign of fatigue failure, they are formed from molecular chains being fractured at the crack tip [54]. In polymers such as epoxies the striations spacing can be related to the stress intensity factor, raised to a power 2[55]. Regular feature are not always striations, they must not be mistaken with riverlines for example, as shown on figure 5.18. The process of mirror/mist/hackle might also be seen in fatigue failure [53] and thus boundaries between static and fatigue fracture are not always easy to distinguish. A transition is shown on figure 5.19.

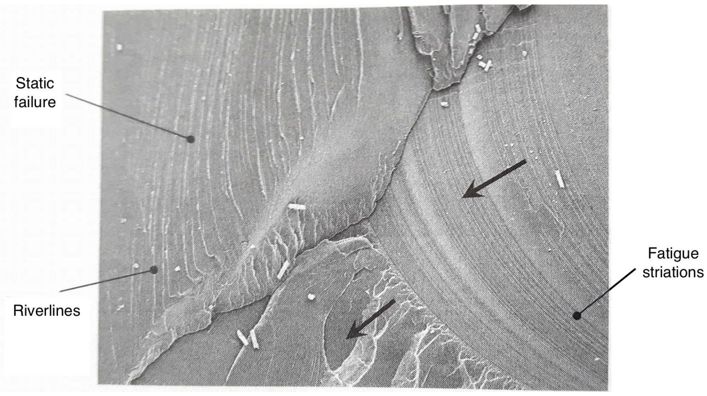

Figure 5.18: Illustration of the differences between static failure fracture surface and fatigue striations [53].

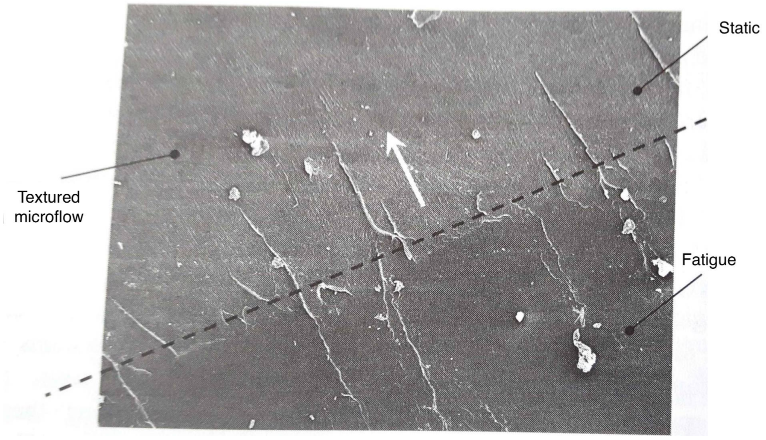

Figure 5.19: Transition between fatigue damaging and static failure[53].

5.4.3 Fracture of RTM6

The fracture of the RTM6 therefore starts from a primary defect. The crack grows and reaches other secondary defects. As the main crack is faster, parabolas are formed when the primary crack overtake the secondary ones. The main crack keeps accelerating until hackle fracture where only a rough surface is observed. When fatigue is applied to the material, the mirror area, which is the area of slow propagation, has a bigger area, as the crack took more time to accelerate.

The failure of the CT specimen also shows an area of slow crack propagation, until a sufficient stress intensity factor is reached. The same parabolas are presents, which confirms the presence of secondary defects. Again the effects of fatigue show an area of slow propagation, with fatigue striations, until the crack is long enough to overcome the stress intensity factor threshold and propagate at a high rate. The transition is very abrupt between no propagation and very fast propagation.

Chapter 6

Conclusion

The main objective of this work was the mechanical characterization of the fracture behavior of the RTM6 epoxy resins and more specifically its behavior at the crack tip. For this end, the fracture toughness was found with tests under static loading and the study of the propagation of the crack under cycling loading has been performed and a better understanding of the fracture behavior of the RTM6 was acquired. The combined results of data from mechanical tests, micrographs and numerical simulations allowed to understand the cause of failure of the material and its degradation under cycling loading. First, the Young's modulus of 3GPa and the stress strain curve were obtain thanks to standard tensile tests. CT tests also provided the fracture toughness of the material. The precracking method was found to have a big impact on the results, not only the length has to be long enough, be the shape and the sharpness of it can considerably influence the failure of the sample. A sharp pre-crack very similar to a fatigue pre-crack is therefore the most suitable to mimic real existing cracks. Thanks to fatigue tests the stress-life curve of the RTM6 was given and it's consistent with other similar epoxy resins. An endurance limit seems to be around 38 MPa. The CT samples allowed to study the propagation of the crack under cyclic loading. The crack propagation rate was plotted against the amplitude of the stress intensity factor. This curve showed two very different behaviors. The shorts cracks, that start with a high rate but are non propagating cracks, and the long cracks. The long cracks were more discussed in this work, they start propagating very slowly, at a threshold of $\mathit{\Delta} K_{th} = 0.28$ but for a short increase of stress intensity factor, the growth increases rapidly until fracture. Between those two regions, there is a brief stable growth, that had been characterized by Paris with the Paris equation. The Paris slope found for RTM6 was of about 12.3. A degradation of the stiffness was also observed after undergoing cycling loading, for both dog-bone and CT specimens. Finite elements analyses associated with the mechanical tests gave a confirmation of the fracture toughness, as well as a stress state at the crack tip of 243 MPa when failure occurs. This is lower than the 300 MPa expected and therefore the existence of an additional defect at the crack tip is very likely.

The ultimate objective of this work was to help the development of higher performance resins and composites. As a continuity of this work, the exact damage model could be implemented in abaqus to observe the crack propagation in the material. Another lead would be the inspection of the nature of the defects observed for example in the cylindrical samples. To increase the fracture toughness and the fatigue threshold a toughening with micro or nano-particles could be performed to reduce the propagation of the cracks.

Chapter 7

Annexe

7.1 Master thesis plan

Master thesis plan

Robin Dormal

April 14, 2017

Professor
Thomas Pardoen

TA
Jérémy Chevalier

1 Objectives

This thesis is focusing on the characterization and the modeling of the failure in fatigue of the RTM6 epoxy resin. This resin is a material highly used in aerospace thanks to its flexibility and its high glass transition temperature for a light weight. Experimental tests will be performed to understand how cracks initiate and propagate in the material and to quantify the material degradation through the decrease of its mechanical properties during cyclic loading (i.e. stiffness and residual strength). The main objective is to find a failure criterion for this resin in fatigue, based on the extension of an existing failure criterion developed for quasi-static loadings.

2 Experimental tests and methods

2.1 S-N curves

The curve gives the number of cycles to failure under a particular loading condition.

2.2 Mechanical properties degradation

- Stiffness drop
- Residual strength and comparison with static strength
- Link to defect's size

2.3 Fracture analysis

- Fractography and comparison with fracture surface under static loading
- Micro defect propagation into cracks.
- Void growth
- Size of critical defects
- CT fracture mechanics samples (true crack propagation)

2.4 Fracture criterion

Extension of the static criterion to fatigue, based on critical defects growth and final size.

3 Experimental test campaigns

- Tests under quasi-static loadings.
- CT Specimens

  Manufacturing of the CT specimens, testing under cycling loading and analyzing of the fracture surface with a scanning electron microscope (SEM).
- Tension-tension

  The manufacturing of the samples (cylindrical dog-bone) is important and the polishing has to be done very carefully.

  Different tests will be performed to analyze the effect of several parameters like the mean stress and the frequency and an analysis of the fracture surface with the SEM will be done.
- Shearing and compression-compression

  The main issue for those tests is the frequency. An innovative setup for the experiment is needed to be able to reach a frequency that is high enough.

4 Analysis of test results and discussion

- CT Tests

  The tests are carried out for the calculation of the fracture toughness and to analyse the crack propagation. The results will allow to draw a curve of $\frac{da}{dN}$ over ΔK, and to find the Paris law for this material. A comparison of the fracture surface in static and in fatigue will also be done.
- Tension - tension tests.

  The tests allow to draw the curve of the stress S over the number of cycles N. They also allow to analyse the effect of several parameters like the mean stress or the frequency. A comparison of the fracture surface under quasi-static loadings and under cycling loadings will be done with the fracture surface of the CT specimens. The fractographic studies will enable a quantitative analysis of the critical defects and their growth or propagation prior to final failure.
- Shearing and compression - compression tests.

  The main issues of the compression tests are the sensitivity to friction and the barreling effect.
- Fracture criterion

  A fracture criterion is to be defined based on all the results of the experiments.

5 Numerical analysis

A finite element analysis is to be performed with the software Abaqus. This analysis will model the mechanical tests that have been performed and compare them with the actual results.

6 Technical resources and contact persons

Supervisors: Jérémy Chevalier, Thomas Pardoen.
Machining: Marc Sinneave, Alban Maton.
SEM: Laurence Ryelandt.
Polishing: Jonathan Lorfèvre.
Mechanical tests: Marc Sinnaeve, Quentin Mestrez.

Static tests machine: Zwick Z250.
Cyclic tests machine: Instron 50kN.

7 Bibliography and references

- Correlation of microcrack fracture size with fatigue cycling on non-crimp fabric/RTM6 composite in the uniaxial fatigue test.

  M.Y. Shiinoa, L.M. De Camargoa, M.O.H. Cioffia, H.C.J. Voorwalda, E.C. Ortizb, M.C. Rezendec

- Fracture mechanics, third edition. T.L. Anderson.

- Fatigue crack propagation behaviour of epoxy resins modified with silica-nanoparticles.

  M.H. Kothmann, R. Zeiler, A. Rios de Anda, A. Bruckner, V. Altstadt

- Experimental determination of the micro-scale strength and stress-strain relation of an epoxy resin.

  Sanita Zike, Bent F. Sorensen, Lars P. Mikkelsen

- Numerical and experimental analysis of the compact tension test for a group of modified epoxy resins

  Martin Maier, Volker Altstidt, David Vinckier, Klaus Thoma

- Characterizing the toughness of an epoxy resin after wet aging using compact tension specimens with non-uniform moisture content

  Gustavo Quino, Jalal El Yagoubi, Gilles Lubineau

- Mechanical fatigue of epoxy resin

  M. Nagasawa, H. Kinuhata, H. Koizuka, K. Miyamoto, T. Tanaka, H. Kishimoto, T. Koike

- Micro-mechanics based pressure dependent failure model for highly cross-linked epoxy resins

  J. Chevalier, X.P. Morelle, C. Bailly, P.P. Camanho, T. Pardoen, F. Lani

- Repeatable pre-cracking preparation for fracture testing of polymeric materials

  Nithiananthan Kuppusamy, Rachel A. Tomlinson

- Mechanical characterization and physics- based modeling of highly-crosslinked epoxy resin

  X.P. Morelle

- Fractography analysis and fatigue strength of carbon fiber/RTM6 laminates

  Maria Odila Hilário Cioffi, Herman Jacobus Cornelis Voorwald, José André Marin Camargo, Mirabel Cerqueira Rezende, Edmundo C. Ortiz, Luigi Ambrosio

- Cyclic Deformation Behavior of an Epoxy Polymer.

  Xinghe Shen, Zihui Xia, and Fernand Ellyin

- Ratcheting behavior of an epoxy polymer and its effect on fatigue life.

  Gang Tao, Zihui Xia

8 Expected schedule

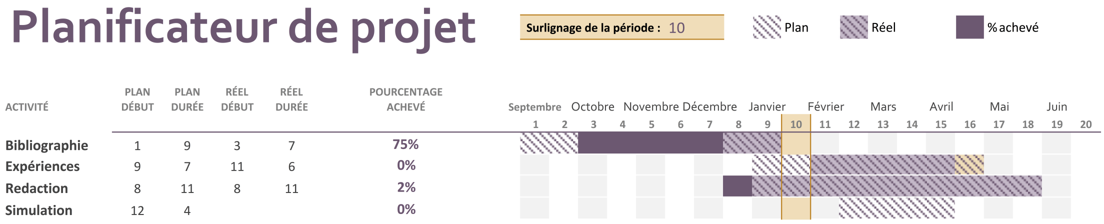

Planificateur de projet

Surlignage de la période : 10

▨ Plan ▨ Réel ■ % achevé

ACTIVITÉ	PLAN DÉBUT	PLAN DURÉE	RÉEL DÉBUT	RÉEL DURÉE	POURCENTAGE ACHEVÉ
Bibliographie	1	9	3	7	75%
Expériences	9	7	11	6	0%
Redaction	8	11	8	11	2%
Simulation	12	4			0%

Bibliography

[1] Materials of the future - part 10 : Composites in aeronautics. `http://www.pluscomposites.eu/publications`. [Online; accessed 2017-06-03].

[2] Esteban VILLALON. Recyclage des composites hautes performances impact dans le cycle de vie aéronautique. `http://asso-acit.fr/wp-content/uploads/2013/07/GROUPE_HEXCEL_ACIT_20132.pdf`, 2013. [Online; accessed 2017-06-03].

[3] T. Pardoen. Introduction to the theory of plasticity. *LMAPR 2482, EPL*, pages 31–41, 2015.

[4] Emile Greenhalgh. *Failure analysis and fractography of polymer composites*, volume 4. Elsevier, 2009.

[5] Stacking of composites laminates. `http://www.composites.ugent.be/home_made_composites`, 2017. [Online; accessed 2017-05-05].

[6] Silvestre T Pinho, Carlos G Dávila, Pedro P Camanho, Lorenzo Iannucci, and Paul Robinson. Failure models and criteria for frp under in-plane or three-dimensional stress states including shear non-linearity. 2005.

[7] A Puck and H Schürmann. Failure analysis of frp laminates by means of physically based phenomenological models. *Composites Science and Technology*, 58(7):1045–1067, 1998.

[8] Martin Knops. *Analysis of failure in fiber polymer laminates: the theory of Alfred Puck.* Springer Science & Business Media, 2008.

[9] ST Pinho, L Iannucci, and P Robinson. Physically-based failure models and criteria for laminated fibre-reinforced composites with emphasis on fibre kinking: Part i: Development. *Composites Part A: Applied Science and Manufacturing*, 37(1):63–73, 2006.

[10] G Catalanotti, PP Camanho, and AT Marques. Three-dimensional failure criteria for fiber-reinforced laminates. *Composite Structures*, 95:63–79, 2013.

[11] PP Camanho, A Arteiro, AR Melro, G Catalanotti, and M Vogler. Three-dimensional invariant-based failure criteria for fibre-reinforced composites. *International Journal of Solids and Structures*, 55:92–107, 2015.

[12] I Srivastava and N Koratkar. Fatigue and fracture toughness of epoxy nanocomposites. *JOM Journal of the Minerals, Metals and Materials Society*, 62(2):50–57, 2010.

[13] X.P. Morelle. *Mechanical characterization and physics- based modeling of highly-crosslinked epoxy resin.* PhD thesis, Université catholique de Louvain, 2015.

[14] Spandan Maiti and Philippe H Geubelle. A cohesive model for fatigue failure of polymers. *Engineering Fracture Mechanics*, 72(5):691–708, 2005.

[15] J Chevalier, XP Morelle, C Bailly, PP Camanho, T Pardoen, and F Lani. Micromechanics based pressure dependent failure model for highly cross-linked epoxy resins. *Engineering Fracture Mechanics*, 158:1–12, 2016.

[16] Kenneth L Reifsnider. *Fatigue of composite materials*, volume 4. Elsevier, 2012.

[17] GF Abdelal, A Caceres, and EJ Barbero. A micro-mechanics damage approach for fatigue of composite materials. *Composite Structures*, 56(4):413–422, 2002.

[18] Fuqiang Wu and WeiXing Yao. A fatigue damage model of composite materials. *International Journal of Fatigue*, 32(1):134–138, 2010.

[19] A Varvani-Farahani, H Haftchenari, and M Panbechi. An energy-based fatigue damage parameter for off-axis unidirectional frp composites. *Composite Structures*, 79(3):381–389, 2007.

[20] RM Guedes. Durability of polymer matrix composites: viscoelastic effect on static and fatigue loading. *Composites Science and Technology*, 67(11):2574–2583, 2007.

[21] Wim Van Paepegem, Ives De Baere, and Joris Degrieck. Modelling the nonlinear shear stress–strain response of glass fibre-reinforced composites. part i: Experimental results. *Composites science and technology*, 66(10):1455–1464, 2006.

[22] Atul Jain, Wim Van Paepegem, Ignaas Verpoest, and Stepan V Lomov. A statistical treatment of the loss of stiffness during cyclic loading for short fiber reinforced injection molded composites. *Composites Part B: Engineering*, 103:40–50, 2016.

[23] Wim Van Paepegem, Ives De Baere, Ebrahim Lamkanfi, and Joris Degrieck. Poisson's ratio as a sensitive indicator of (fatigue) damage in fibre-reinforced plastics. *Fatigue & Fracture of Engineering Materials & Structures*, 30(4):269–276, 2007.

[24] Lode Daelemans, Sam van der Heijden, Ives De Baere, Hubert Rahier, Wim Van Paepegem, and Karen De Clerck. Improved fatigue delamination behaviour of composite laminates with electrospun thermoplastic nanofibrous interleaves using the central cut-ply method. *Composites Part A: Applied Science and Manufacturing*, 2016.

[25] S Rabinowitz and P Beardmore. Cyclic deformation and fracture of polymers. *Journal of Materials Science*, 9(1):81–99, 1974.

[26] Roel PM Janssen, Dirk de Kanter, Leon E Govaert, and Han EH Meijer. Fatigue life predictions for glassy polymers: a constitutive approach. *Macromolecules*, 41(7):2520–2530, 2008.

[27] M Nagasawa, H Kinuhata, H Koizuka, K Miyamoto, T Tanaka, H Kishimoto, and T Koike. Mechanical fatigue of epoxy resin. *Journal of materials science*, 30(5):1266–1272, 1995.

[28] MM Abdel Wahab, I Hilmy, IA Ashcroft, and AD Crocombe. Evaluation of fatigue damage in adhesive bonding: part 1: bulk adhesive. *Journal of Adhesion Science and Technology*, 24(2):305–324, 2010.

[29] Tomas Walander, Alexander Eklind, Thomas Carlberger, and Ulf Stigh. Fatigue damage of adhesive layers–experiments and models. *Procedia Materials Science*, 3:829–834, 2014.

[30] ASTM Standard et al. Astm d 5045-99. standard test methods for plane-strain fracture toughness and strain energy release rate of plastic materials. *Annul Book of ASTM Standards*, 14, 1996.

[31] simulia. Fracture mechanics study of a compact tension specimen using abaqus/cae, 2007.

[32] Jérémy Chevalier, Xavier Morelle, Christian Bailly, Thomas Pardoen, and Frédéric Lani. " characterization and modeling of the strain-rate, temperature and pressure dependence of the deformatio nof a highly crosslinked aerospace grade epoxy resin.

[33] Arash Dahi Taleghani, Milad Ahmadi, JE Olson, et al. Secondary fractures and their potential impacts on hydraulic fractures efficiency. In *ISRM International Conference for Effective and Sustainable Hydraulic Fracturing*. International Society for Rock Mechanics, 2013.

[34] Leandro R Alejano and Antonio Bobet. Drucker–prager criterion. *Rock mechanics and rock engineering*, 45(6):995–999, 2012.

[35] HEXCEL Product Data. „hexflow® rtm 6, 180 c epoxy system for resin transfer moulding. *Monocomponent System*.

[36] L Castellani and M Rink. Fatigue crack growth of polymers. *European Structural Integrity Society*, 28:91–116, 2001.

[37] MH Kothmann, R Zeiler, A Rios de Anda, A Brückner, and V Altstädt. Fatigue crack propagation behaviour of epoxy resins modified with silica-nanoparticles. *Polymer*, 60:157–163, 2015.

[38] Lennart Elfgren. Fatigue capacity of concrete structures: Assessment of railway bridges, 2015.

[39] Hiroshi Tada, Paul C Paris, and George R Irwin. The stress analysis of cracks. *Handbook, Del Research Corporation*, 1973.

[40] Norman E. Dowling. *Mechanical Behavior of Materials*. Pearson, 2012.

[41] C. W. Macgregor and N. Grossman. *Effects of Cyclic Loading on Mechanical Behavior of 24S-T4 and 75S-T6 Aluminum Alloys and SAE 4130 Steel*. 1952.

[42] CM Manjunatha, AC Taylor, AJ Kinloch, and S Sprenger. The tensile fatigue behavior of a gfrp composite with rubber particle modified epoxy matrix. *Journal of Reinforced Plastics and Composites*, 29(14):2170–2183, 2010.

[43] MR Loos, J Yang, DL Feke, and I Manas-Zloczower. Enhanced fatigue life of carbon nanotube-reinforced epoxy composites. *Polymer Engineering & Science*, 52(9):1882–1887, 2012.

[44] Yuanchen Huang, Yunpeng Zhu, Carlos Alberto Cimini Jr, and Sung Kyu Ha. Characterization of moisture effect on static and fatigue performance of epoxy resin using thin-film specimen on dynamic mechanical analyzer. *Journal of Composite Materials*, page 0021998316644851, 2017.

[45] Gang Tao and Zihui Xia. Ratcheting behavior of an epoxy polymer and its effect on fatigue life. *Polymer testing*, 26(4):451–460, 2007.

[46] Y Murakam, T Nomoto, and T Ueda. Factors influencing the mechanism of superlong fatigue failure in steels. *Fatigue & fracture of engineering materials & structures*, 22(7):581–590, 1999.

[47] KJ Miller. The short crack problem. *Fatigue & Fracture of Engineering Materials & Structures*, 5(3):223–232, 1982.

[48] Joris Everaerts. Fatigue crack initiation and facet formation in ti-6al-4v wires. 2017.

[49] Kasper Lambrighs. Fatigue properties of heavily drawn steel wires. *PhD study, Katholieke Universiteit Leuven*, 2010.

[50] MH El Haddad, TH Topper, and KN Smith. Prediction of non propagating cracks. *Engineering Fracture Mechanics*, 11(3):573–584, 1979.

[51] Frank Fischer, Uwe Beier, Felipe Wolff-Fabris, and Volker Altstädt. Toughened high performance epoxy resin system for aerospace applications. *Science and Engineering of Composite Materials*, 18(4):209–215, 2011.

[52] Chaosuan Kanchanomai and A Thammaruechuc. Effects of stress ratio on fatigue crack growth of thermoset epoxy resin. *Polymer Degradation and Stability*, 94(10):1772–1778, 2009.

[53] Emile Greenhalgh. *Failure analysis and fractography of polymer composites*, volume 5. Elsevier, 2009.

[54] CSH Bawn. Encyclopedia of polymer science and engineering: Ji kroschwitz, hf mark, n. bikales, cg overberger and g. menges (eds.) john wiley and sons, new york, 1985, 906 pages, us 240,£ 170, isbn 0-471-89540-7, 1987.

[55] RW Hertzberg, MD Skibo, and JA Manson. Fatigue fracture micromechanisms in engineering plastics. In *Fatigue Mechanisms*. ASTM International, 1979.

Rue Archimède, 1 bte L6.11.01, 1348 Louvain-la-Neuve **www.uclouvain.be/epl**